FEDERAL UNIVERSITY OF PARAÍBA
CENTER OF TECHNOLOGY
GRADUATE PROGRAM IN MECHANICAL ENGINEERING

JOSÉ WILKER DE LIMA SILVA

GENERALIZED FUNCTIONALS FOR QUALIFICATION OF GEOLOGICAL CARBON STORAGE INJECTION SITES

JOÃO PESSOA
2024

José Wilker de Lima Silva

Generalized functionals for qualification of geological carbon storage injection sites

Thesis submitted to the Graduate Program in Mechanical Engineering of Federal University of Paraíba as part of the requirements for obtaining the degree of Doctor in Mechanical Engineering. Concentration Area: Thermal Science and Fluids.

Advisor: Prof. Dr. Gustavo Charles Peixoto de Oliveira

Co-advisor: Prof. Dr. Igor Fernandes Gomes

João Pessoa - PB
July 2024

José Wilker de Lima Silva

Funcionais generalizados para qualificação de locais de injeção para armazenamento geológico de carbono

Tese apresentada ao Programa de Pós-Graduação em Engenharia Mecânica da Universidade Federal da Paraíba como parte dos requisitos para obtenção do título de Doutor(a) em Engenharia Mecânica. Área de Concentração: Termofluidos.

Orientador(a): Prof. Dr. Gustavo Charles Peixoto de Oliveira
Co-orientador(a): Prof. Dr. Igor Fernandes Gomes

João Pessoa - PB
Julho de 2024

GENERALIZED FUNCTIONALS FOR QUALIFICATION OF GEOLOGICAL CARBON STORAGE INJECTION SITES

por

JOSÉ WILKER LIMA DA SILVA
Tese aprovada em 10 de julho de 2024

Prof. Dr. Gustavo Charles Peixoto de Oliveira
Orientador – UFPB

Prof. Dr. Igor Fernandes Gomes
Coorientador – UFPE

Prof. Dr. Moises Dantas dos Santos
Examinador Interno – UFPB

Prof. Dr. João Alves de Lima
Examinador Interno – UFPB

Prof. Dr. Paulo Couto
Examinador Externo – UFRJ

Prof. Dr. Abouzar Mirzaei-Paiaman
Examinador Externo – University of Texas at Austin

João Pessoa – PB
2024

To my wife and constant companion, Dayana, who has always supported me. Also to my sons, Pedro and George, who had to endure my absence many times until this thesis could be concluded.

ACKNOWLEDGEMENTS

"Now faith is the substance of things hoped for,
the evidence of things not seen."
(Hebrews 11:1, King James Bible)

"For verily I say unto you,
That whosoever shall say unto this mountain,
Be thou removed, and be thou cast into the sea;
and shall not doubt in his heart,
but shall believe that those things which he saith shall come to pass;
he shall have whatsoever he saith."
(Mark 11:23, King James Bible)

RESUMO

SILVA, J. W. L. **Funcionais generalizados para qualificação de locais de injeção para armazenamento geológico de carbono**. 2024. 117pp. Tese (Doutorado em Engenharia Mecânica) – Programa de Pós-Graduação em Engenharia Mecânica, Universidade Federal da Paraíba, João Pessoa, 2024.

Muitas nações comprometeram-se a alcançar a neutralidade de carbono até 2050 através da implementação do armazenamento geológico de carbono (GCS) como uma tecnologia fundamental no quadro da captura, utilização e armazenamento de carbono (CCUS), liderando assim a iniciativa *Net Zero*. O objetivo do CCUS é capturar as emissões de dióxido de carbono (CO_2), reciclando-as ou transportando-as através de dutos até formações geológicas subterrâneas para armazenamento permanente. Apesar do sucesso global nos projetos de GCS, impulsionados pelo setor de petróleo e gás, as iniciativas de GCS em grande escala ainda estão em seus estágios iniciais no Brasil. Estão em desenvolvimento bases de dados para potenciais locais de armazenamento, incluindo aquíferos salinos e reservatórios esgotados, tal como acontece com a estrutura regulamentar. Esta tese apresenta modelos matemáticos para a seleção sistemática e classificação de locais subterrâneos de armazenamento de CO_2. A pesquisa explora uma família de funcionais matemáticos, cada um com funções de ponderação distintas, atingindo dois objetivos principais. Em primeiro lugar, esclarece as interações não lineares entre as propriedades das rochas e dos fluidos utilizando indicadores de qualidade. Em segundo lugar, avalia regiões geográficas, considerando armadilhas estruturais em rochas capeadoras. Esta metodologia é um recurso valioso para identificar locais adequados de injeção e armazenamento. Os modelos foram implementados utilizando o *Matlab Reservoir Simulation Toolbox* (MRST), e estudos de casos utilizando o modelo UNISIM-I-D para o Campo de Namorado na Bacia de Campos, Brasil, mostraram a influência da permeabilidade e porosidade assim como de curvas sigmóides, exponenciais ou híbridas nas diferentes interpretações de locais ideais de armazenamento, com excedentes que variam até 66% no melhor dos casos. Foram utilizados o modelo de equilíbrio vertical para diminuição do custo computacional e análise de sensibilidade Sobol para estudar a influência individual de cada parâmetro. Resultados das simulações corroboram com as análises teóricas. O objetivo final do estudo é estabelecer uma base de conhecimento fundamental para futuros projetos de GCS no Brasil, aproveitando infraestruturas de poços herdados.

Palavras-chave: descarbonização, armazenamento geológico de carbono, métodos computacionais, seleção de locais geológicos.

ABSTRACT

SILVA, J. W. L. **Generalized functionals for qualification of geological carbon storage injection sites**. 2024. 117pp. Thesis (Doctoral Degree in Mechanical Engineering) – Graduate Program in Mechanical Engineering, Federal University of Paraíba, João Pessoa, 2024.

Many nations have pledged to achieve carbon neutrality by 2050 through the implementation of geological carbon storage (GCS) as a pivotal technology within the carbon capture, utilization, and storage (CCUS) framework, thus spearheading the Net Zero initiative. The CCUS goal is to capture carbon dioxide (CO_2) emissions, recycling them or transporting them through pipelines to underground geological formations for permanent storage. Despite global success in GCS projects, driven by the oil and gas sector, large-scale GCS initiatives are still in their early stages in Brazil. Databases for potential storage sites, including saline aquifers and depleted reservoirs, are in development, as with the regulatory structure. This thesis introduces mathematical models for the systematic selection and ranking of underground CO_2 storage sites. The research explores a family of mathematical functionals, each with distinct weighting functions, achieving two main objectives. Firstly, it clarifies non-linear interactions between rock and fluid properties using quality indicators. Secondly, it evaluates geographical regions, considering structural traps in caprocks. This methodology is a valuable resource for identifying suitable injection and storage locations. The models were implemented using the Matlab Reservoir Simulation Toolbox (MRST), and a case study using the UNISIM-I-D model for the Namorado Field in the Campos Basin, Brazil, indicates the influence of permeability and porosity as well as sigmoid, exponential or hybrid curves on different interpretations of ideal storage locations, with surpluses that range up to 66% in the best case. The vertical equilibrium model was used to reduce computational cost and Sobol sensitivity analysis to study the individual influence of each parameter. Simulation results corroborate the theoretical analyses. The ultimate objective of the study is to establish a fundamental knowledge base for future GCS projects in Brazil, leveraging legacy well infrastructures.

Keywords: decarbonization, geological carbon storage, computational methods, geological site selection.

LIST OF FIGURES

LIST OF TABLES

LIST OF ABBREVIATIONS, ACRONYMS AND SYMBOLS

Abbreviations and Acronyms

CCS	Carbon capture and storage
CCUS	Carbon Capture, Utilization and Storage
DDU	Discrete dynamic unit
DECC	Department of Energy & Climate Change of the United Kingdom
FU	Flow unit
GCS	Geological carbon storage
GHG	Greenhouse gas
IPCC	Intergovernmental Panel on Climate Change
IUC	Injectivity unit class
MCC	Maximum closeness centrality
ML	Machine learning
MRST	Matlab Reservoir Software Toolbox
O&G	Oil and Gas
QM	Quality map
RPS	Reservoir process speed
SSA	Sobol sensitivity analysis
UNISIM-I-D	Universal Simulator for I-dimensional reservoirs
VE	Vertical equilibrium
VQM	Volumetric quality map

Arabic symbols

$^{\circ}C$	degree Celsius
n_p	Number of active cells
p	Pressure
p_{crit}	Critical pressure
s_w	Water saturation
$u_{()}$	Continuous real-valued function
$\mathbf{x}, \mathbf{y}$	Position vector
b	Boundary
B	Statistical binning method
cP	CentiPoise
C	Cluster

d	Distance
Gt	Gigaton
G	Graph
I,J,K	three-dimensional logical coordinates
J*	3rd quartile of the distribution of all Jaccard numbers
J	Jaccard index
km	Kilometer
Mt	Megaton
M	Mega
m	Meter
Pa	Pascal
s	Second
vol	Volume
v	Node
W	Well

Greek symbols

β	Distance-to-trap function
γ	Closeness centrality
∞	Infinity
κ	Permeability field
$\mathcal{F}$	Functional
$\mathcal{V}_{\otimes,k}$	k-ary Cartesian product
$\mathfrak{J}$	functional
ϕ	Porosity field
σ	Standard deviation
Σ	Summation
τ	Trap index
υ	Trap volume ratio
$\mathbf{K}$	Permeability tensor

Others symbols

$(\ )^c$	Complementary set
$(\ )^\perp$	Normal projection
$\lceil\ \rceil$	Ceiling function
$\{S_{()}\}$	Collection of storage sites
$c_{(\ )}$	Cell

e_j	Percentage of intersecting sites
$S_{()}$	Single storage site
#()	Cardinality

CONTENTS

1   INTRODUCTION

The escalating global energy demand has compelled governments, private entities, and the international community to commit to reducing greenhouse gas emissions into the atmosphere. Given that CO_2 is a primary driver of anthropogenic climate change, the development of effective abatement mechanisms is imperative in our pursuit of achieving carbon neutrality by 2050, commonly referred to as "Net Zero" (BOUCKAERT *et al.*, 2021; IEA, 2023).

In anticipation of this sustainable future, geological carbon storage (GCS) has emerged as a vital technology for mitigating CO_2 emissions. Since the 1990s, the industrial implementation of underground CO_2 injection for permanent storage has been underway (FURRE *et al.*, 2017). Typical storage sites for CO_2 are assignable to depleted oil and gas reservoirs. These sites possess adequate storage capacity, benefit from previous understanding of geological and hydrodynamic features, and are less susceptible to injection-induced seismic events compared to saline aquifers (ZOBACK; SMIT, 2023).

Brazil as a global frontline country in storage potential[1] embraces CCS initiatives nationwide since the disclosure of its National Climate Change Plan (FEDERAL, 2008). Pioneer surveys concerning CCS and the theoretical CO_2 storage capacity of Brazilian hydrocarbon fields, aquifers, and coalbeds underscored that its sedimentary basins could potentially accommodate more than 2035 Gt of CO_2 (IGLESIAS *et al.*, 2015). Newer assessments point out that the country is ready to leverage prolific GCS ventures (CIOTTA *et al.*, 2021). At present, offshore basins and depleted reserves, especially those covering the Pre-salt region, are the most promising sites (DREXLER *et al.*, 2020; RODRIGUES *et al.*, 2022).

Beyond the precise mapping of GCS opportunities, the definitive approval of a regulatory framework and investments in lower-cost technologies are open issues. Advancements toward GCS regulation in the country came primarily from the Bill of Law 1425/2022, coined the "CCS Bill of Law", which will rule GCS activities and reuse along the national territory, both in economic zones and in the continental shelf under homeland jurisdiction[2]. The areas of interest for GCS extend from North to South, both onshore and offshore, but their individual storage capacity varies dramatically.

As a backbone for the GCS challenges, reservoir simulation plays a relevant role for action in emerging carbon markets. Therein, site selection, site characterization, and injection well placement are key factors to add efficiency, safety, and predictability in field projects (JUN *et al.*, 2019; LUBOŃ, 2021). Although injection well placement methods for GCS have much in common with the knowledge base inherited from the petroleum industry, they need adap-

---

[1]   The Global Status of CCS 2018.
[2]   Incentive to decarbonize the economy is approved by the Brazilian environmental commission.

tions for different scenarios and goals, such as caprock identification, detailed modeling of supercritical gas dynamics, and general site selection frameworks. All of these features are of fundamental interest for exploration and development planning.

With that growing interest in GCS, traditional well placement techniques formerly used for production purposes are being transformed and readjusted for injection purposes. A few examples of the literature include simulation-based optimization for reduction of leakage risk in storage operations tested in brine-saturated reservoirs (STOPA *et al.*, 2016), mixed integer programming for injection schedule (MIYAGI *et al.*, 2018), multiphase simulations for analysis of gas flow in fractured media (case from Yangtze Basin, China) (HU *et al.*, 2021), and coupled geomechanics / neural networks simulations for injection efficiency in faulted sands (case from Gulf of Mexico) (ESPINOZA *et al.*, 2022).

While GCS well placement strategies focused on the internal features of the formations have been developed worldwide, so far, there are limited application of frameworks for storage in Brazilian basins and especially of mathematical models for GCS selection, characterization, and simulation under the perspective of quality maps and dynamic petrophysical units — subjects detailed in the next section. To fill in these gaps, this thesis presents a family of functionals intended to qualifying GCS sites and ultimately indicating high-performance injection sites. Each functional provides a distinguished interpretation of appropriate storage locations and incorporate several static and dynamic variables. Through numerical simulations, we examined the CO_2 plume path and its storage inventory over a well-known model for a reservoir located at the Campos Basin, in Brazil southeastern region. Simulations of new-frontier infrastructure reveal that the storage surplus reached at the locations suggested by the functionals may be better up to 66% in contrast to the legacy well infrastructure at the best case.

1.1 Thesis objectives and findings

The specific objectives of this thesis are:

- To propose detailed multi-parametric mathematical models that help to select and prioritize carbon dioxide (CO_2) storage sites within underground formations;

- To simulate numerically the CO_2 plume dynamics through the porous media for different scenarios and assess the trapping mechanisms inventory, especially the stratigraphical and structural ones;

- To suggest well placement strategies and techniques and potential locations for efficient injection by using the underlying concepts of *flow units*, *injectivity*, and *volumetric quality map*;

- To apply computational engineering techniques for discretizing, clustering, and ranking CO_2 storage sites.

  As a consequence, one ultimately expects it will share insights for:

- Establishing a physically consistent and explainable theoretical framework that supports realistic GCS field projects;

- Providing a numerical perspective for the wide-scope issue of greenhouse gas (GHG) mitigation with special attention to CO_2 disposal;

- Leveraging the scientific and technological development of GCS in Brazil.

This study presented a set of injectivity functionals that can be used to qualify CO_2 storage sites. These functionals are promising in supporting geological carbon storage ventures, as they can improve injection performance for wells located in strategic positions. Since there are many physical properties affecting gas dynamics in deep storage, this study handled them statically. For the Brazilian context, this research is useful in developing a comprehensive understanding of CO_2 injection processes. Comparisons showed a storage surplus increase of up to 66%.

1.2 Thesis outline

Beyond this introduction chapter and the conclusion, this thesis has the following core chapters and matters:

- Chapter 2: a literature review on relevant works on CO_2 storage is presented;

- Chapter 3: the methods that were applied to obtain the results are presented, through geological, mathematical and computational frameworks;

- Chapter 4, the results obtained are presented, adding discussion, comparison and justification.

2 LITERATURE REVIEW

CO_2 storage in underground geological formations has a plentiful history. This chapter introduces the state-of-art devoted to this technology from a review of the scientific progress of its implementation worldwide.

First of all, we provide some contextual information to base specific discussions.

2.1 Energy transition challenges

The growth in demand for energy worldwide has been pushing society and public agents to seek mechanisms that reduce the emission of carbon dioxide into the atmosphere, since it is the main triggering component of anthropogenic climate change. The scale of the problem is evident given the growing population base with increasing demands for more energy-intensive lifestyles (MACDOWELL *et al.*, 2010; STOCKER, 2014; VERHEGGEN *et al.*, 2014; COOK *et al.*, 2016; ROSE *et al.*, 2017). Despite the urgent transition toward renewables, the dominance of fossil fuels persists due to their energy density, well-established resource base, and extensive infrastructure for extraction and distribution. This perpetuates their integral role in power generation, heating, and heavy industrial manufacturing operations. Acknowledging this reality, it is clear that fossil fuels will remain a crucial component to meet energy demands for the foreseeable future. Balancing the imperative for sustainable practices with the current energy infrastructure represents a complex challenge as the world grapples with the need to address climate change while ensuring continued access to reliable and abundant energy sources. The increase of atmospheric concentration of CO_2 is responsible for raising the average earth temperature and the ocean's level (RISE, 2004; SOLOMON, 2009; NASA, 2015)

Power plants and energy-intensive industries are the major CO_2 emitters, and now they are compelled to drastically reduce their CO_2 emission. The high carbon intensity of the power sector (42%) is due to the large share of coal-fired plants in the global electricity supply. Hence, decarbonization of power and industrial sectors is essential to achieve emission reduction targets. By 2050, the global energy demand should to double. At the same time, it is expected that the production of energy from fossil sources will gradually decline until a carbon neutral scenario is reached: the so-called *Net Zero* (BOUCKAERT *et al.*, 2021).

The annual increase in CO_2 emissions is an alarming phenomenon, driven by voracious energy consumption in the industrial sector in China and the United States. Both economic powers have increased their demand for energy sources, many of which still depend intensively on fossil fuels. Furthermore, the rising economic dynamism in India, Indonesia, Saudi Arabia and Mexico also contributes to this worrying scenario. Rapid growth in these nations drives

industrial production and energy consumption, often from non-renewable sources. The need for infrastructure and increased industrial production in these emerging countries are intrinsically linked to an increase in CO_2 emissions. Given this panorama, it is crucial to implement effective strategies to contain emissions, such as the transition to renewable energy sources and the adoption of cleaner technologies (Figure 1).
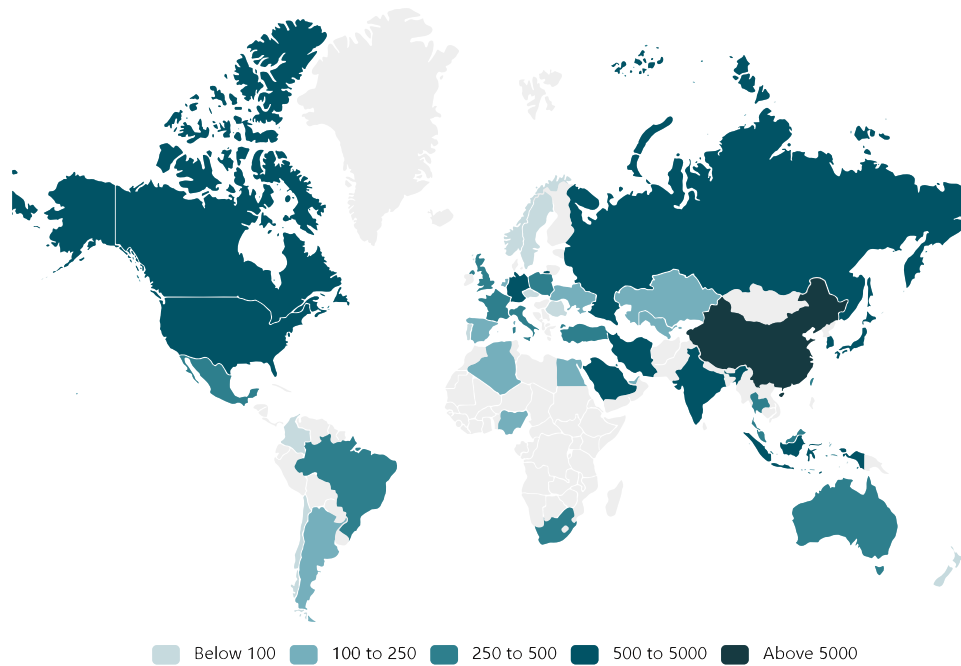
Figure 1 – Global CO_2 emission (MtCO_2) in 2022. Source: (ENERDATA, 2023).

2.2 Carbon Capture and Storage (CCS)

As the global community transitions towards a more sustainable energy chain, the focus on *carbon capture and storage* (CCS) intensifies as one of the most promising technologies to mitigate CO_2 emissions and, consequently, greenhouse gases. The inception of this technique dates back to the 1970s, as documented in the literature (Table 1), gaining substantial attractiveness roughly two decades later. At its core, CCS involves capturing the CO_2 emanating from industrial processes that involve the combustion of fuels. The captured CO_2 is then transported to a suitable location, where it is injected into deep geological formations, ensuring permanent storage and preventing gas leakages into the atmosphere. This method is characterized by its substantial storage capacity, offering long-term isolation of CO_2 for at least several hundred years. Additionally, CCS demonstrates a reasonable cost-effectiveness and minimizes environmental impact (YAMASAKI, 2003). As industrial activities continue to play a pivotal role in global economies, the imperative to adopt technologies like CCS becomes increasingly evident. The collaborative pursuit of such innovative solutions holds the key to achieving sustainable and environmentally responsible practices on a global scale.

Table 1 – CCS Milestones.

Year	Resume
1972	First injection of CO_2 at an oil field in Texas, USA. The CO_2 was used to enhance oil recovery (EOR).
1986	The concept of CO_2 capture and storage (CCS) was for the first time presented by Norwegian researchers.
1996	The Sleipner project in the North Sea opens as the world's first large scale commercial CO_2 storage project, storing one Mton-CO_2 annually. CO_2 is separated from natural gas produced from the Sleipner field and injected into the Utsira formation, an aquifer 800 m below the bottom of the sea.
1997	Working with the Kyoto Protocol, world leaders acknowledged CCS as a potential mitigation mechanism, but no incentives were included in the final agreement.
2004	Second commercial large scale project in operation: The In Salah project in Algeria
2005	Australia is the first country to establish a regulatory framework for CCS.
2007	EU heads of state and governments commit to building 10-12 demonstration projects for CCS by 2015. The G8 leaders recognize the critical role of CCS in tackling climate change, and recommend to build 20 CCS demonstration plants worldwide by 2010.
2008	The EU Climate package: An EU wide demonstration programme for CCS is established, and income from the European Trading Scheme (ETS) will be used to finance the demonstration programme. CO_2 Storage Directive and financial mechanisms for CCS demonstration projects also part of the agreement.
2010	Introduction of European Commission's NER300 – world's largest funding programme for CCS demonstration projects and innovative renewable energy technologies.
2012	Official opening of Technology Centre Mongstad (TCM) in Norway – world's largest facility for testing and improving CO_2 capture. Canada sets CO_2 Emission Performance Standard (EPS) for both new coal-fired power plants and existing plants that have reached the end of their useful lives, which effectively calls for CCS, at 420 tonnes of CO_2 per GWh.
2013	EU releases CCS Communication which acknowledges role of CCS in tackling emissions from industry. Bio-CCS facility Decatur in Illinois, USA, stores world's first 500,000 carbon negative tonnes of CO_2.
2014	World's first full-scale commerical CCS project opens at coal power plant Boundary Dam in Canada's Saskatchewan province. The EU sets climate targets in the 2030 Framework for Climate and Energy Policy and begins work on the Energy Union Strategy.
2015	Adoption of the Paris Agreement at COP21, which emphasizes the role of CCS in achieving climate goals. SaskPower's Boundary Dam CCS project in Canada becomes fully operational, demonstrating large-scale CCS for coal-fired power plants.
2016	Start of operation of the Petra Nova CCS project in Texas, USA, capturing CO_2 from a coal-fired power plant.
2017	Continued cost reductions in CCS technologies and processes, making them more economically viable. Advancements in solvent-based capture technologies and monitoring methods.
2018	Start of operations of the world's first commercial-scale natural gas power plant with CCS, the Net Power plant in Texas and increase in operational CCS storage projects globally, demonstrating storage viability.
2019	Growing policy support for CCS with increased funding and incentives in several countries and expansion of CCS projects in Europe, North America, and Asia-Pacific regions.
2020	Accelerated focus on CCS as a key technology for achieving net-zero emissions targets by mid-century and investment: Increased private and public sector investments in CCS projects and research.
2021	CCS prominently featured at COP26 with renewed commitments and initiatives.
2022	Advances in direct air capture (DAC) and carbon utilization technologies and expansion of CCS infrastructure and pipelines to support multiple projects.
2023	Launch of large-scale CCS projects in emerging markets and continued deployment in established markets and increased international cooperation on CCS research, development, and deployment.

CCS emerges as a pivotal strategy in the comprehensive decarbonization of both the power and industrial sectors (BRINCKERHOFF *et al.*, 2011). Recognized by the Intergovern-

mental Panel on Climate Change (IPCC) as an indispensable resource, CCS plays a crucial role in the pursuit of international environmental objectives. The IPCC identifies it as a linchpin for achieving goals such as constraining future global warming within the 2°C threshold, thereby mitigating the onset of severe climate change events (IPCC, 2005; AGENCY, 2016; BRUHN *et al.*, 2016).

Projections suggest that the widespread implementation of CCS has the potential to reduce CO_2 emissions by approximately 20% come 2050, as outlined in the roadmap presented by the Department of Energy & Climate Change of the United Kingdom (DECC, 2012). This estimate underscores the transformative impact that CCS can wield on mitigating climate change by curbing carbon emissions.

In the overarching context of the global climate crisis, the endorsement and active integration of CCS into sustainability agendas represent a critical step toward realizing a low-carbon future. The collaborative efforts to propel CCS technologies forward are fundamental to achieving a substantial reduction in greenhouse gas emissions and fostering a resilient and sustainable global environment.

2.3 Brazilian context

Brazil is renowned for its low carbon intensity energy matrix, primarily driven by hydroelectric power generation. The country's greenhouse gas (GHGs) are predominantly attributed to deforestation and land use changes. In spite of this, Brazil has shown a strong commitment to advancing research on geological carbon storage (GCS) as a crucial approach to mitigating GHGs. This commitment has been particularly underscored by the commencement of production from pre-salt reservoirs, which contain significant amounts of CO_2 in the extracted fluids[3].

In a study by Iglesias *et al.* (2015), efforts by various sectors in Brazil, including government, academia, and industry, were briefly described in their pursuit of CCS development and promotion. Among the key initiatives driving CCS advancement in Brazil, the establishment of a dedicated research center for CO_2 capture technologies and the investigation of potential long-term storage reservoirs within the country were highlighted. Additionally, pilot-scale installations for field testing and validation of CCS technologies have been initiated. The support and involvement of Brazil's largest oil company, PETROBRAS, have played a key role in the initial phases of CCS development, with the impetus being the substantial pre-salt oil reserves and a commitment to minimizing emissions from these reserves. The establishment and growth of Center of Excellence in Carbon Storage Research (CEPAC), a research center focused on addressing geological storage challenges and knowledge gaps, have also significantly contributed to CCS development in the country.

---

[3]   1st Annual CCS: Report in Brazil 2022/2023.

In line with international trends, Brazil presented your first CCS Atlas (KETZER *et al.*, 2015), illustrating the potential for establishing CCS projects within its borders. This potential is particularly noteworthy, given the prospect of CCS projects in the bioenergy sector, taking into account the considerable number of existing biofuel production facilities in the country. Amidst global challenges facing CCS deployment in recent years, Brazil has emerged as a nation actively engaged in advancing this key technological solution for emissions reduction and climate change mitigation.

Brazil as a global frontline country in storage potential (INSTITUTE, 2018) embraces CCS initiatives nationwide since the disclosure of its National Climate Change Plan (FEDERAL, 2008). According to Iglesias *et al.* (2015), pioneer surveys concerning CCS and the theoretical CO_2 storage capacity of Brazilian hydrocarbon fields, aquifers, and coalbeds underscored that its sedimentary basins could potentially accommodate more than 2035 Gt of CO_2 (Figure 2a). Newer assessments point out that the country is ready to leverage prolific GCS ventures (CIOTTA *et al.*, 2021). At present, offshore basins and depleted reserves, especially those covering the Pre-salt region, are the most promising sites (DREXLER *et al.*, 2020; RODRIGUES *et al.*, 2022).

(a)   (b)
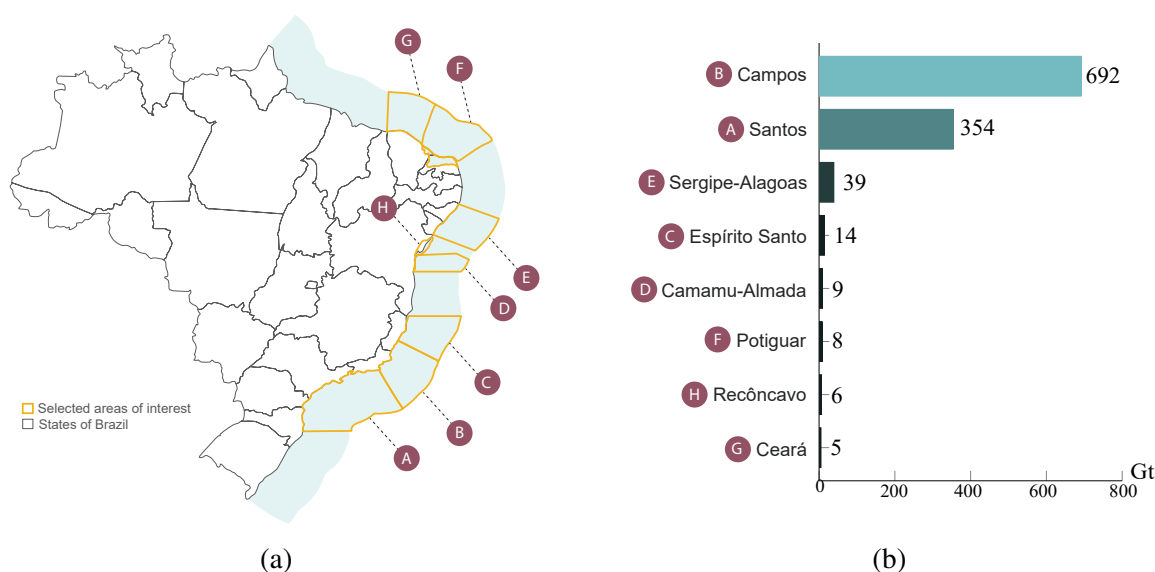
Figure 2 – (a) Selected areas of interest for CO_2 storage in Brazil; (b) Brazilian basins with the largest theoretical storage capacities of supercritical CO_2 in Gigatons (adapted from (CIOTTA *et al.*, 2021)).

Beyond the precise mapping of GCS opportunities, the definitive approval of a regulatory framework and investments in lower-cost technologies are open issues. Advancements toward GCS regulation in the country came primarily from the Bill of Law 1425/2022, coined the "CCS Bill of Law", which will rule GCS activities and reuse along the national territory, both in economic zones and in the continental shelf under homeland jurisdiction[4]. The areas of

---

[4] Incentive to decarbonize the economy is approved by the Brazilian environmental commission.

interest for GCS extend from North to South, both onshore and offshore, but their individual storage capacity varies dramatically.

Câmara *et al.* (2016) presented the need to structure a regulatory framework for the use of CCS technologies to create an environment of trust for civil society and the private sector and presented legal and infra-legal normative documents (laws, decrees, regulations, among others) existing in force in Brazil to identify gaps and regulatory weaknesses for the implementation of CCS projects in Brazil, since CCS technologies are recent and current laws and regulations do not provide for the use of such technologies. The expected Brazilian economic and industrial growth suggests that, in the coming years, CO_2 emissions in the country will increase. The activities of the oil industry, especially activities related to exploration in the pre-salt zone, and the growing demand for energy, will be the major concerns involving CO_2 emissions in Brazil, since it has a great potential for geological storage of CO_2 based on the existence of mature oil basins or those in declining production, such as the Recôncavo Basin, which are favorable to the large-scale use of CCS technology.

In the current environmental context, the significance of technological advancements is evident, along with the incentives for adopting CCS technology, not only in Brazil but also globally. Whether through public financing or emissions fees, exploratory studies indicate the potential for CO_2 mitigation. Specifically, in Brazil's petroleum-rich Pre-salt and Recôncavo Basin regions, an estimated annual emissions capacity suggests the mitigation potential of 26.4 million tonnes of CO2e. Research further reveals that Brazil's geological reservoirs have the capacity to store approximately 2,000 billion tonnes (2,000 Gt) of CO2e (CÂMARA; AN-DRADE; ROCHA, 2011). The implementation of CCS activities, both in Brazil and worldwide, and the concurrent development of associated technologies are essential for reducing a substantial amount of carbon dioxide in the atmosphere over the coming decades. However, given the multitude of factors to consider, both technically and operationally, CCS should be treated as a coordinated international endeavor. This entails formulating clear and achievable proposals and goals for implementation in line with the Paris Agreement, which includes setting specific targets for carbon dioxide capture and storage, methods for stimulating public and private investments, and the establishment of formal agreements ratified by the legislative and executive branches of participating countries. Effective collaboration between governmental bodies, private enterprises, and international organizations is paramount to create a secure legal framework for CCS activities in Brazil (NUNES; COSTA, 2019).

Luo *et al.* (2023) recently presented an in-depth examination of the mechanisms underlying carbon dioxide storage and utilization at the ocean floor. Their analysis encompassed critical technical and economic considerations and synthesized existing research on safety risks, investment monitoring and control technologies, as well as operational costs, with a focus on identifying remaining gaps in knowledge. The unique characteristics of the deep-sea environment, characterized by high pressure and low temperatures, enable the generation of liquid

CO_2 and CO_2 hydrate with larger density and gravitational stability compared to seawater. This makes deep-sea storage an effective and reliable option for carbon dioxide sequestration. The cost associated with offshore carbon dioxide storage is closely intertwined with several factors, including the type of storage reservoir (e.g., saline formations or depleted fields), geological conditions (e.g., porosity, permeability, and depth), and the chosen storage methods (liquid or mineral carbonation). Notably, the study found that many coastal countries prefer offshore locations for their carbon storage sites due to these factors. Furthermore, the research highlighted that offshore carbon capture, utilization, and storage (CCUS) is still in its nascent stages in Brazil, and public awareness and perception of this concept are evolving.

Based on research conducted by Ciotta *et al.* (2021), Brazil's substantial size and significant global economic involvement warrant international attention when it comes to efforts aimed at mitigating its carbon emissions. Utilizing depleted oil and gas fields offers a multitude of benefits, including access to technical data, economic viability, pre-existing infrastructure, and reduced environmental impacts. The authors provide an estimation of the storage capacity within 85 offshore oil and gas fields in Brazil, connecting this capacity with the existing infrastructure and emissions-related criteria. This combination of storage capacity analysis, emissions information, and infrastructure availability serves as crucial criteria for pinpointing the most suitable areas for carbon dioxide (CO_2) storage in the Brazilian offshore region. One key takeaway from this study is that many of Brazil's major cities are situated along the coast and are significant sources of CO_2 emissions. Consequently, designating offshore fields for CO_2 storage proves pertinent as it minimizes the distance for transportation. Furthermore, employing depleted oil and gas fields for CCS also offers the possibility of substituting straightforward decommissioning processes. By capitalizing on existing infrastructure and technical expertise, Brazilian offshore fields enhance the feasibility of successful carbon storage projects. The regions of utmost interest, possessing the most favorable criteria for implementing a CO_2 storage initiative, are the Santos and Campos basins (Figure 2b). The Brazilian Northeast region also holds potential for carbon storage, albeit to a relatively lesser extent compared to the Recôncavo and Southeast regions. This underscores the feasibility of utilizing pilot projects to store coastal emissions.

Within the Brazilian context, a study by Oliveira *et al.* (2021) and Cañas (2022) conducted an assessment of the CO_2 storage potential within the Irati Formation, situated in the Paraná Basin—a region hosting a majority of the nation's stationary carbon emission sources. Among the deep geological formations considered for CO_2 storage, shale layers have emerged as a promising field due to their high efficiency, abundance, and significant organic matter content, which enhances CO_2 retention. However, one of the key challenges in identifying suitable reservoir locations lies in the need for accurate geological characterization and storage volume estimation. To address this, three-dimensional (3D) implicit modeling techniques were employed, not only for volume calculations but also for site selection. These techniques generated thematic 3D models that indicated critical attributes such as thickness, depth, geological

structures, and proximity to aquifer systems. The initial findings are promising, as the estimated storage capacity surpasses the total locally produced CO_2, signifying the potential to support the development of new CCS projects in this region.

2.4 Geological carbon storage challenges

In CCS technology, one of the best options for CO_2 sequestration is underground geological storage (IPCC, 2005), which comprises saline aquifers, depleted oil and gas reservoirs and coal seams (Figure 3) (BACHU, 2000; YANG *et al.*, 2008; MICHAEL *et al.*, 2010; NA *et al.*, 2015). Initial work such as Holloway and Savage (1993) showed the need and possibility of disposing of CO_2 underground in offshore oil and gas fields with great advantages in relation to the cost of exploration and storage, with the need to search for ideal locations with large blockages in reservoir rocks.
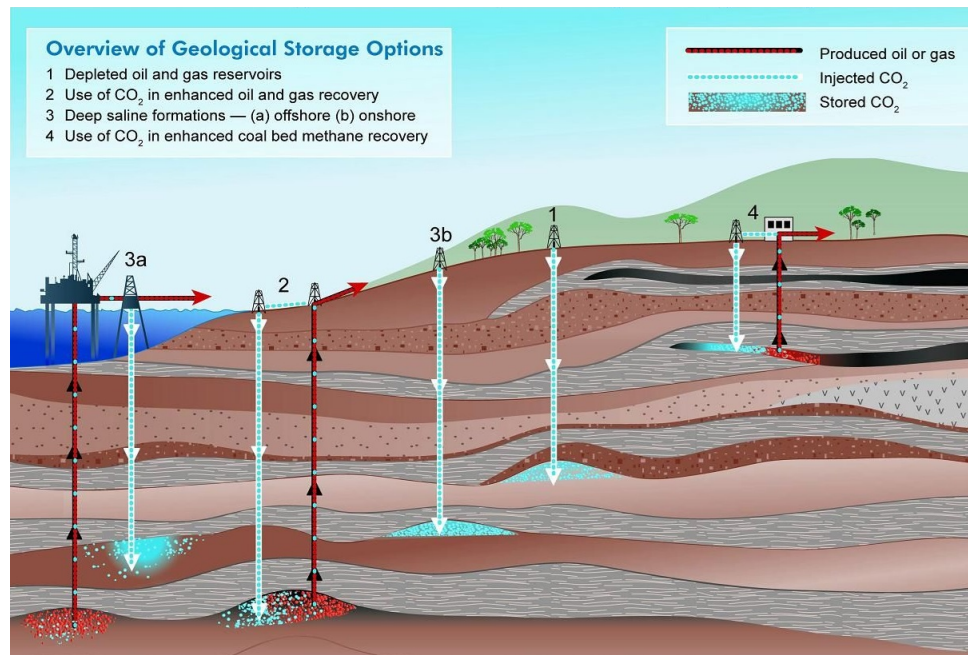
Figure 3 – Methods for storing CO_2 in deep underground geological formations. Source: (IPCC, 2005).

According to Bachu (2000), geological CO_2 sinks do not require major technological development as they use technologies applied by industry for the exploration and production of hydrocarbons. However, the biggest challenge is identifying the best methods and locations for adequate long-term CO_2 storage. Some ways of storing CO_2 take into account elimination in oil and gas reservoirs and injection into deep saline aquifers. Some criteria are considered to evaluate the potential of a sedimentary basin for CO_2 storage, such as geological configuration, economic aspects and socio-political conditions. The most suitable sedimentary basins for CO_2 sequestration are basins in a mature stage of exploration and development located on stable continental shelves or along divergent tectonic plates and with favorable geology and hydrodynamic regime of formation waters, conducive to hydrodynamic and mineral entrapment

in geological time scale. The identification of zones of high permeability and porosity will help locate the best locations for CO_2 injection and sequestration.

Still by Bachu (2002), the potential for CO_2 escape and migration is a decisive factor in screening unsafe sites and site capacity must be determined based on in situ conditions and the properties and behavior of CO_2. It was suggested that the geological space of each basin be transformed into CO_2 space. The CO_2 space can then be mapped and used to identify locations with significant storage capacity and locations that are unsafe due to CO_2 phase instability or potential migration and escape.

Studies carried out by Nordbotten, Celia and Bachu (2005) suggest an analytical solution that provides a tool to estimate practical quantities associated with CO_2 injection, describing the spatio-temporal evolution of the plume. Kumar *et al.* (2005) presented reservoir simulation studies of a CO_2 sequestration project in a deep saline aquifer with the feasibility of permanent storage such that large volumes of CO_2 do not escape from the aquifer. The authors concluded that the movement of gas leaves a residual gas saturation and dissolves in the native brine, reducing the amount of mobile gas, thus preventing CO_2 from reaching the top of the aquifer.

Meyer *et al.* (2008) reported the regional screening, selection and geological characterization of a potential onshore CO_2 storage site (saline aquifer) in northeastern Germany to identify and investigate a candidate CO_2 storage site from a lignite-fired power plant. Even with the results achieved by the study, the authors suggest more data and research (modeling) to prove the structural integrity of the storage site and ensure long-term safety, as some issues regarding the integrity of the cover rock or the quality of the reservoir could not be addressed. According to Stangeland (2007), the European Union could feasibly capture and store 25 billion tonnes of CO_2 by 2050.

Grataloup *et al.* (2009) applied a methodology for selecting geological CO_2 storage sites taking into account criteria whose combinations allowed potential sites, considering storage optimization in terms of capacity and injectivity, risk minimization, regulation, environmental restrictions, in addition economic considerations and social aspects. The amalgamation of essential selection criteria enables the demarcation of potential CO_2 storage zones, whereas the synthesis of criteria for site qualification offers a means to evaluate potential locations and subsequently pinpoint the most suitable ones within a specific context. The choice of criteria for this site selection process may vary based on local conditions, objectives, and data accessibility. Qualitative or quantitative attributes can be determined through data aggregation, reprocessing, analysis, or fresh data acquisition, depending on the specific requirements.

Schnaar and Digiulio (2009) presented a summary of computational modeling studies developed to predict the fate and transport of CO_2 based on scientific understanding of these underground processes through sensitivity analyzes and descriptions of the use of site characterization data in model development. However, the study did not characterize the injection site

for best efficiency.

Research carried out by Shukla *et al.* (2010) identified important research gaps and the need for further studies on the integrity of caprock. A comprehensive study was presented on the various techniques and mechanisms involved in mitigating carbon dioxide during and after its sequestration in geological formations, with special emphasis on its safe storage in sedimentary basins. Storage periods typically last a long period of time and therefore the importance of the integrity of the caprock seal for the required duration is critical for successful CO_2 sequestration projects. Pioneering geological CO_2 storage projects, as cited by Jenkins *et al.* (2012), have shown satisfactory results in relation to safety and the possibility of significant amounts of storage, also taking into account the social aspects relating to the challenges inherent to CCS projects.

Zhao *et al.* (2014) introduced an approach for assessing CO_2 storage that takes into account factors such as CO_2 displacement efficiency, CO_2 sweep efficiency, CO_2 dissolution in oil and gas, and CO_2 displacement mechanisms. These critical factors in the evaluation method are determined through the integration of reservoir simulation techniques, thermodynamic principles, and statistical analysis methods. As a result, they established a comprehensive system for evaluating CO_2 storage capacity.

In recent work, open source computational tools have been used to model large-scale, long-term CO_2 migration. An example of this is MRST - Matlab Reservoir Software Toolbox, through your module MRST-co2lab, which takes into account the ideas of basin modeling, computational geometry, hydrology and reservoir simulation. Furthermore, vertical equilibrium methods for efficient simulation of structural, residual and solubility traps were used, such as Nilsen *et al.* (2015a), and addressing the need for future work to identify good injection sites and optimize injection strategies.

Considering the importance of ensuring the safety of CCS projects over thousands of years, it is important to study the structural traps and spill paths beneath a seal rock. Subsurface knowledge can be captured quantitatively using computational methods, for example, developed in oil production. In this regard, Nilsen *et al.* (2015b) presented a set of tools provided by the separate module in the open source Matlab Reservoir Simulation Toolbox (MRST), consisting of geometric and percolation-type methods for calculating structural traps and spill paths below of a sealing rock. Using water management concepts, these tools have been applied to large-scale aquifer models to quickly estimate structural entrapment potential, determine spill paths from potential injection points, suggest optimal injection locations, etc.

Lie *et al.* (2016) presents a simulation workflow for large-scale CO_2 storage in the Norwegian North Sea. It addresses the need for robust computational tools to model and predict CO_2 injection and migration in geological formations. The authors develop and validate a workflow that integrates various simulation components, including geological modeling, flow simulation, and uncertainty quantification. They apply this workflow to a case study in the

North Sea, demonstrating its capability to handle complex subsurface scenarios and providing insights into the feasibility and safety of CO_2 storage. The study underscores the importance of advanced simulations for effective CO_2 sequestration strategies.

Allen *et al.* (2017) explored the potential storage capacities within different geological formations through the optimization of well placement, injection rates, and the utilization of production wells for pressure management as needed. They devised optimal strategies based on various simple yet realistic objectives and constraints, including penalties for CO_2 leakage, cost minimization of well operations, and restrictions on pressure build-up. The optimization techniques employed accounted for the long-term impact of CO_2 leakage, circumventing the need to make assumptions about the geological timescale over which the aquifer's properties would remain constant. The duration that CO_2 must be retained within a rock formation to qualify as permanent storage is a subject of political and regulatory debate. Nonetheless, irrespective of whether this timeframe is defined as centuries, millennia, or millions of years, the algorithms developed in this study can be used to maximize storage capacity under the assumption of a stable geological model.

Ahmadinia and Shariatipour (2018) analyzed the importance of the structural geometry of the top seal on CO_2 plume migration and long-term retention behavior. The results indicate the feasibility of vertical equilibrium models for simulating CO_2 migration and the approach can be used to develop other simulators. The authors suggested to use VE and composition models in ECLIPSE (PETTERSEN, 2006) to carry out a comprehensive study on the feasibility of the VE module in MRST to simulate the CO_2 storage process in saline aquifers.

Ringrose (2018) studied CO_2 plume monitoring on the Sleipner offshore gas platform (Norway). The results indicated a storage efficiency of 5% of the pore volume after 14 years of injection, with approximately 10% of this volume dissolved into the brine phase. These estimates are consistent with the fluid dynamics of CO_2 injection, in which gravity-dominated processes are expected to provide efficiencies in the range of 1-6%. The author concluded that there are ways to increase storage efficiency beyond 6%, whether using smart well placements to explore geology or modifying the injection flow. In the same year, Abbaszadeh and Shariatipour (2018) examined CO_2 injection in a model and performed sensitivity analyzes for some fluid, rock and injection parameters. The results showed that pressure and the CO_2 plume influence storage efficiency and safety.

Ajayi, Gomes and Bera (2019) presented an extensive perusal on CO_2 storage technologies. This comprehensive review encompassed the historical evolution of fundamental storage concepts, the intricate physical processes at play, the modeling techniques and simulators employed, capacity estimation methods, measurement monitoring and verification strategies, as well as the associated risks and challenges. It turns out that the key components of a successful carbon dioxide storage project involve precise site selection, rigorous characterization (including storage capacity estimation and plume modeling), and diligent monitoring to mitigate the

risks of potential leaks through seals.

In the quest for sedimentary basins suitable for CCS projects, an investigation by Abuov, Seisenbayev and Lee (2020) identified optimal basins in Kazakhstan (Central Asian country), considering factors such as containment, capacity, and feasibility. The study had estimated that the nation possesses a total effective CO_2 storage capacity of around 583 Gt. The findings indicated that four sedimentary basins have the potential to make a substantial impact on reducing greenhouse gas emissions in Kazakhstan, thereby facilitating the country's transition toward achieving the objectives outlined in the Paris Agreement.

An examination of the impact of injection well placement on CO_2 storage efficiency was conducted by Luboń (2021) in the context of three well-known geological formations (traps) located in the deep aquifers of the Early Jurassic Polish Lowlands. To simulate CO_2 injection, geological models of these structures were employed across fifty distinct well locations. Computer simulations revealed that the dynamic CO_2 storage capacity varies based on the chosen injection well location. The findings indicated that for structures with favorable reservoir properties, the CO_2 storage efficiency increases as the distance from the injection well to the top of the structure and the depth differential to the top of the structure expand. Conversely, for structures with less favorable reservoir properties, the opposite trend is observed. Furthermore, as the quality of petrophysical reservoir parameters improves, such as porosity and permeability, the significance of injection well placement in assessing CO_2 storage efficiency becomes more pronounced.

Akai *et al.* (2021) introduced a numerical modeling investigation concerning the CO_2 storage capacity within depleted gas reservoirs. Initially, this study relied on a basic volumetric equation to estimate the CO_2 storage capacity in such reservoirs. Subsequently, a numerical reservoir simulation was conducted, accounting for various reservoir characteristics, including reservoir heterogeneity, aquifer water intrusion, rock compaction, and their potential reversibility. The simulation outcomes consistently indicated a substantial quantity of CO_2 trapped in the form of a dissolved component into water.

The utilization of deep saline aquifers for CO_2 storage represents a clear avenue for large-scale CO_2 mitigation. The initial and vital step in deploying large-scale CCUS projects is to determine the storage capacity. However, the assessment of CO_2 capacity in aquifer formations through existing methods is subject to uncertainties arising from the selection of storage mechanisms, data quality, evaluation algorithms, and exogenous factors. Wei *et al.* (2022) conducted a comprehensive review of these methods. They introduced a hierarchical framework for capacity evaluation, categorizing capacity types and providing insights into the assessment processes and the uncertainties associated with capacity estimation.

Romeo *et al.* (2022) introduced the assessment method employed by the US Department of Energy for evaluating storage capacity in non-petroleum saline reservoirs, with a specific focus on offshore environments. Offshore carbon storage offers several potential advantages, in-

cluding increased distance from densely populated areas and reduced likelihood of interactions with groundwater. The study also delved into considerations related to potential storage distributions, sensitivity analyses, and the integration of spatial data and tools aimed at facilitating the secure selection of suitable storage sites.

Callas *et al.* (2022) details a comprehensive workflow and criteria for selecting depleted hydrocarbon reservoirs for carbon storage, addressing the growing need for effective CO_2 sequestration solutions. The authors highlight the advantages of using depleted reservoirs, such as their established capacity, existing infrastructure, and available geological data, which make them promising candidates for carbon storage. The proposed selection workflow is a multi-criteria decision-making process that integrates technical, economic, and environmental considerations. Key technical criteria include reservoir capacity, integrity, and injectivity, ensuring the site can safely and effectively store CO_2. Economic factors encompass the costs associated with transportation, injection, and monitoring of CO_2, as well as potential financial incentives or regulatory frameworks supporting carbon storage projects. Environmental criteria focus on minimizing ecological impacts and ensuring long-term containment of CO_2 to prevent leakage. The authors demonstrate the application of this workflow through detailed case studies, showcasing its practical utility in real-world scenarios. The case studies illustrate the evaluation process, from initial screening of potential sites to detailed assessments of their suitability for carbon storage. This systematic approach ensures that selected reservoirs meet stringent safety and efficiency standards, contributing to the development of viable carbon storage strategies.

Yang *et al.* (2023) presents a method for evaluating the CO_2 storage potential of saline aquifers in a petroliferous basin, addressing the critical need for effective carbon sequestration strategies. The authors develop a comprehensive evaluation method that integrates geological, hydrodynamic, and economical factors to assess the suitability of saline aquifers for CO_2 storage. The proposed method involves a detailed analysis of the geological characteristics of the aquifer, including its porosity, permeability, and thickness, which determine the storage capacity and injectivity of CO_2. Hydrodynamic assessments are conducted to understand fluid flow and pressure changes within the aquifer, ensuring that CO_2 can be effectively injected and contained over long periods. Additionally, economic evaluations consider the costs associated with CO_2 capture, transportation, injection, and monitoring, as well as potential financial incentives and regulatory requirements. The authors validate their method through a case study in a petroliferous basin, demonstrating its practical application and effectiveness. The case study involves detailed geological and hydrodynamic modeling, as well as cost-benefit analyses, to identify the most suitable sites for CO_2 storage within the basin. Overall, the study provides a robust framework for assessing the CO_2 storage potential of saline aquifers, contributing to the development of viable carbon sequestration solutions. This method can be applied to other basins, aiding in the global effort to mitigate climate change by securely storing CO_2 emissions.

In their study, Rasool *et al.* (2023) conducted a comprehensive comparative analysis

of CO_2 storage across various geological formations, including deep saline aquifers, depleted reservoirs, coal seams, basalt formations, and clastic formations. This analysis was based on seven key factors sourced from the literature: safety, storage capacity, injection rates, efficiency, residual entrapment, containment and integrity, and potential for improvement. These factors were individually assessed and ranked on a scale from low to high. Subsequently, a classification system was developed to categorize geological formations for CO_2 storage. The results revealed that deep saline aquifers and basalt formations emerged as the most promising options for effective CO_2 storage.

Callas *et al.* (2023) introduced a regional exploration method designed to identify and prioritize numerous potential sites for large-scale CCS projects, ultimately pinpointing the most suitable location or locations for sequestering a substantial volume of CO_2. This method employs a phased, criteria-based approach that comprehensively screens a wide range of depleted hydrocarbon reservoirs, taking into account technical, regulatory, political, socioeconomical, and environmental factors. It is worth noting that many studies offering best practices or general approaches for site selection in carbon storage lack a focus on the quality of the data used for assessments. Specifically, there is a lack of specific metrics that elucidate how to quantitatively evaluate various properties. The workflow outlined in that study is structured into multiple steps, spanning from the initial screening of potential sites to the site-specific characterization phase. However, it acknowledges that, during the site characterization phase, additional information, simulations, and data collection may be necessary. The criteria used in this methodology are categorized to address key aspects related to CO_2 injection and geological storage, encompassing: injection capacity and optimization; retention and mitigation of geomechanical risks; location and economic constraints. This structured approach ensures a comprehensive evaluation of candidate sites and promotes a more informed and systematic decision-making process in CCS project planning.

In a recent study by Yang *et al.* (2023), a comprehensive assessment was conducted to examine the progress achieved in carbon dioxide (CO_2) storage projects worldwide, with a focus on analyzing the key companies and businesses engaged in CCS initiatives. The research highlighted the critical importance of a well-thought-out CO_2 injection strategy, as deficiencies in this aspect can lead to well integrity issues, hydrate formation, and challenges in maintaining proper pressure control. Moreover, it emphasized the need for further research, particularly in the realm of geological assessments before injection and storage. Several salient points emerged from the analysis: While CO_2 injection can be applied to a variety of geological formations, depleted oil and gas reservoirs stand out as the most promising candidates for carbon storage. This preference arises from the fact that these reservoirs have undergone thorough exploration and development phases, providing valuable information on key factors such as reservoir capacity, permeability, porosity, and the quality of the covering rock and sealing mechanisms—essential prerequisites for effective carbon storage; additionally, the existing critical infrastructure originally utilized for oil exploration and production, including pipelines, injection wells, and pro-

duction wells, can be repurposed for CCS with only minor modifications, thus streamlining the implementation of carbon storage projects; advances in monitoring techniques during the CO_2 injection and storage processes, whether in deep or shallow geological formations, have significantly reduced environmental and resource-related risks. This progress enhances confidence in the successful execution of CCS initiatives, as it helps ensure the protection of the environment and natural resources.

Examining the fate of CO_2 dynamics and storage on a large scale necessitates the incorporation of uncertainty and sensitivity analysis. In their recent work, Alqahtani *et al.* (2023) introduced a robust workflow that leverages machine learning (ML) to facilitate both uncertainty and global sensitivity analysis in the prediction of CO_2 storage within deep saline aquifers. Advanced sampling techniques were used, enabling high-resolution simulations (MRST-`co2lab`) that capture the intricate details of the system. Moreover, acknowledging the non-linear relationships between input parameters and the corresponding output variables, the workflow employs ML to manage these complex associations effectively. To expedite the hyperparameter tuning process, Bayesian optimization was utilized, enhancing the efficiency of the analysis. The workflow employs Monte Carlo simulations to explore the propagation of uncertainty, providing valuable insights into how uncertainties affect the system. This approach holds great potential for application in field-scale CO_2 sequestration projects within deep saline aquifers, contributing to a more informed understanding of the dynamics and storage of CO_2 on a large scale. Recently, Fotias, Ismail and Gaganis (2024) advocated for the efficacy of Bayesian Optimization in the context of optimizing well placement for CCS operations, emphasizing its potential as a preferred methodology for enhancing sustainability in the energy sector.

Izadpanahi *et al.* (2024) highlights the advantages of nano-injection, particularly in larger pores, which increases capillary entry pressure and interfacial tension, thereby enhancing long-term capillary trapping. Foam-assisted gas injection, especially in multi-cycle applications, is shown to improve sweep efficiency and residual trapping. The stimulation of microbial activity is crucial for converting dissolved CO_2 into mineral-secured CO_2, facilitating its sequestration through mineralization. For narrow, low-permeability saline aquifers, hydraulic fracturing is recommended to enhance injectivity and storage capacity, while rock heterogeneity can further improve storage efficiency. The study emphasizes the importance of maintaining water-wet conditions for optimal storage and containment security. Additionally, it suggests co-injecting pollutants like SO2 and CH4 with CO_2 to increase safety and cost-effectiveness in CCS systems. Overall, the study underscores the need for a holistic approach that integrates these methods to maximize the efficiency and safety of CO_2 storage in saline formations.

2.5 Thermodynamics considerations to GCS

Supercritical CO_2 is recognized as one of the most effective industrial solvents. Due to its planar molecular configuration, CO_2 can escape from tight geological formations that have historically trapped methane more easily, a molecule with a three-dimensional structure. Monitoring at a CO_2 injection facility in Frio, Texas, has shown that injecting CO_2 into saline aquifers results in decreased brine pH and the dissolution of carbonates and iron oxyhydroxides. This dissolution process compromises the structural integrity of surrounding rocks, potentially creating fractures and pathways for CO_2 and brine leakage. Furthermore, it can mobilize toxic trace metals and organic compounds, leading to significant environmental risks if these substances migrate into potable groundwater (KHARAKA *et al.*, 2006). Additionally, a monitoring study conducted in Cranfield, Mississippi, revealed that current models and computational tools are inadequate for accurately predicting reservoir responses. This highlights the challenges faced in forecasting the long-term fate and transport of CO_2 in geological reservoirs (HOVORKA; MECKEL; TREVINO, 2013).

An interesting aspect of offshore CO_2 storage is related to the molecular structure of CO_2, which is planar and angular. When CO_2 dissolves in fresh and saline water, it increases the density of the aqueous solution [43]. This denser CO_2-saline solution tends to sink in the ocean, preventing the gas from rising to the surface and escaping into the atmosphere. This characteristic renders deep ocean sequestration of CO_2 significantly less risky compared to storage in geological formations and suggests that it may be the preferable long-term storage option for CO_2 (MCBRIDE-WRIGHT; MAITLAND; TRUSLER, 2015).

Aminu *et al.* (2017) provided an overview of advancements in carbon dioxide storage, addressing both resolved critical issues and highlighting challenges that demand increased focus in the realms of CO_2 sequestration, criteria for assessing storage sites, CO_2 behavior within reservoirs, and methodologies for estimating CO_2 storage capacity. In reference to the critical CO_2 point (7.38 MPa and 31.1°C, equivalent to a hydrostatic head of 738 m), even a minor variation in geothermal gradient with depth can lead to CO_2 reaching supercritical conditions (Figure 4a).

Assuming that the pressure distribution within a sedimentary basin follows hydrostatic principles, the minimum required depth for injecting CO_2 in its supercritical state, under a geothermal gradient of 25°C/km and a surface temperature of 15°C, is approximately 800 m (Figure 4b). Moreover, Siqueira, Iglesias and Ketzer (2017) revised experimental and numerical models utilized in the examination of CO_2-water-rock interactions and their practicality in assessing how carbon dioxide injection affects the quality and integrity of carbonate reservoirs.
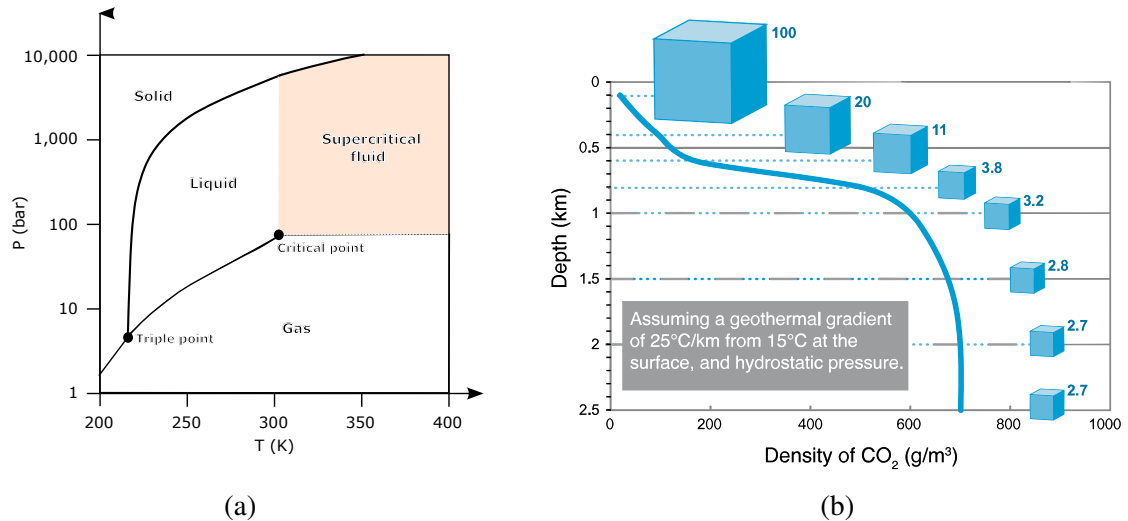
Figure 4 – (a) CO_2 pressure-temperature phase diagram; (b) The density of CO_2 varies with depth, assuming hydrostatic pressure and a geothermal gradient of 25°C per kilometer from 15°C at the surface. Beyond 800 meters depth, there is a rapid increase in carbon dioxide density, leading to the attainment of a supercritical state. The cubes in the representation signify the relative volume occupied by CO_2, showing a significant decrease in volume down to 800 m. Beyond this depth, specifically below 1.5 km, both density and specific volume stabilize, exhibiting near-constant values. Source: (IPCC, 2005).

2.6 Particular challenges of GCS numerical modeling

Kumar *et al.* (2005) identify several numerical challenges associated with the simulation of CO_2 storage in deep saline aquifers. These challenges include:

- Nonlinearities in multiphase flow equations: the simulation of CO_2 injection involves solving highly nonlinear multiphase flow equations. These nonlinearities arise from phase behavior, relative permeability, and capillary pressure effects, which complicate the numerical solution and require robust iterative solvers;

- Large-scale computational models: modeling CO_2 storage accurately requires detailed geological models with fine spatial discretization to capture heterogeneities in the reservoir. This leads to large-scale computational models with millions of grid cells, demanding substantial computational resources and efficient numerical algorithms;

- Phase behavior of CO_2: CO_2 exhibits complex phase behavior under reservoir conditions, including supercritical states, which must be accurately represented in the simulation. The equations of state (EOS) used to describe CO_2 properties add to the complexity of the numerical model;

- Coupling of mass and energy transport: the injection of CO_2 into saline aquifers involves coupled mass and energy transport processes, including heat transfer and dissolution of

CO_2 into the brine. Accurately simulating these coupled processes poses significant numerical challenges;

- Stability and convergence: ensuring numerical stability and convergence of the solution is challenging, especially when dealing with sharp fronts and discontinuities in the concentration of CO_2 and pressure fields. Advanced stabilization techniques and adaptive time-stepping methods are often required;

- Heterogeneity of the reservoir: geological formations are inherently heterogeneous, and accurately capturing this heterogeneity is crucial for realistic simulations. Representing fine-scale heterogeneities in large-scale models without excessive computational cost remains a challenge;

- Capillary trapping and hysteresis: capillary trapping mechanisms and hysteresis effects in relative permeability and capillary pressure relationships must be included in the models to accurately predict CO_2 plume behavior and long-term storage security;

- Numerical diffusion: numerical diffusion can artificially smear sharp fronts and interfaces, leading to inaccurate predictions of CO_2 migration and trapping. Mitigating these numerical artifacts requires high-resolution schemes and careful grid design.

The authors address these challenges by implementing advanced numerical techniques, such as adaptive gridding, efficient solvers, and improved physical models, to enhance the accuracy and efficiency of CO_2 storage simulations.

Benson and Cole (2008) highlight the numerical and geological challenges associated with simulating CO_2 storage in deep sedimentary formations, including interactions between gas and brine, are diverse and complex. In relation to geological heterogeneity, the variability in the properties of sedimentary formations, such as permeability and porosity, makes it difficult to accurately model the behavior of CO_2 after injection. The simulation must capture interactions between CO_2, brine and rock phases, including dissolution processes, mineral precipitation and capillary displacement. As the behavior of CO_2 is influenced by the pressure and temperature conditions of the reservoir, models must integrate mass and heat transfer accurately. According to the authors, numerical techniques need to predict and validate the migration of CO_2 and its retention over time to guarantee the safety and effectiveness of storage. Regarding temporal and spatial scale, simulations must cover long periods (hundreds to thousands of years) and large areas, which requires significant computational resources and advanced modeling techniques to maintain accuracy and efficiency. These challenges highlight the need for continued advances in modeling techniques and the importance of a detailed understanding of the processes involved in CO_2 storage in deep sedimentary formations.

Hesse, Orr *et al.* (2008) investigates the behavior of CO_2 gravity currents in deep saline aquifers, with a specific focus on residual trapping. The research addresses how CO_2 behaves

after injection, moving like a gravitational current due to the difference in density between CO_2 and saline water. The formation of a CO_2 plume is analyzed, considering the influence of residual entrapment, where part of the CO_2 is retained in the rock matrix, reducing its mobility and escape potential. The study develops mathematical models and analytical solutions to describe the temporal and spatial evolution of these gravitational currents. A crucial aspect of the model is the consideration of vertical balance, which simplifies the analysis by assuming that vertical pressure variations are negligible compared to horizontal variations. This allows the application of more simplified and analytical solutions to predict the behavior of CO_2. The results show that residual trapping plays a significant role in the long-term security of geological CO_2 storage, helping to limit plume extent and promoting the retention of injected CO_2.

Kopp, Class and Helmig (2009) present several numerical and geological challenges associated with simulating CO_2 storage in deep sedimentary formations, especially considering the interactions between gas and brine. Some of the main challenges include the estimation of storage capacity coefficients as the accurate determination of storage capacity coefficients is complicated due to the heterogeneity of saline aquifers and variations in pressure and temperature conditions. Furthermore, sedimentary formations present great variability in permeability and porosity properties, which influences the distribution and migration of injected CO_2. Regarding multiphase interactions, accurate simulation must consider the complex interactions between CO_2, brine and rock phases, including capillary effects, CO_2 solubility in brine and the formation of residual phases. Regarding the modeling of transport processes, capturing the dynamics of CO_2 transport in porous media, including advection, dispersion and diffusion, is fundamental and requires advanced numerical techniques. Due to the complexity and scale of the simulations, significant computational resources are required to solve the 3D multiphase flow equations. Regarding monitoring and verification, predicting CO_2 migration and validating numerical models require robust monitoring and verification techniques to ensure that CO_2 remains confined in the reservoir.

Studies carried out by Eigestad *et al.* (2009) described a dataset for the Johansen geological model (southwest of Norway) for estimating the CO_2 sequestration capacity and the processes that could cause gas leakage into the above formations through numerical simulation. Results show that the choice of lateral boundary conditions can significantly alter simulation results and that a computational improvement is necessary to adequately resolve the CO_2 plume.

From Juanes, MacMinn *et al.* (2010) studies pointed out that CO_2 moves radially away from the injection well and up the formation due to buoyancy forces when injected into deep saline aquifers. Because of the large horizontal dimensions of the plume, three-dimensional simulations of CO_2 plume migration over long periods of time are computationally expensive. Therefore, to obtain results within a reasonable period of time it is necessary to use coarse meshes that result in inaccurate results due to numerical errors. More accurate models based on vertical equilibrium (LAKE, 1989) were used in studies by Nilsen *et al.* (2011) and Nilsen,

Lie and Andersen (2016), ensuring an increase in performance compared to standard three-dimensional models, providing reliable estimates of long-term CO_2 migration, incorporating geometry and aquifer heterogeneity, considering the effects of hydrodynamic and residual trapping, which can be used to provide reliable estimates of long-term CO_2 migration.

Some early studies on geological leak risk assessment from underground storage using a depleted oil field or deep saline aquifers, such as Zucatelli *et al.* (2013), used numerical modeling as a tool to evaluate and predict the fate of CO_2 injected from the storage behavior, what will be the fate of the CO_2 after its injection and what will be the geological risk of leakage.

Bandilla *et al.* (2014) used mathematical modeling as a tool to predict the migration of CO_2 to ensure safe and permanent storage through a series of models with different levels of complexity, such as a numerical model of vertical equilibrium with a clear interface, a numerical model of vertical balance with capillary transition zone and vertically integrated model with dynamic vertical pressure. The results showed that vertical balance models are sufficient for modeling.

When the IPCC Special Report on CCS was released in 2005, the notion of CO_2 storage efficiency had not yet been introduced, and as a result, no numerical values had been included in the scientific literature. CO_2 storage efficiency is defined as the ratio of the volume of CO_2 injected into a geological formation's pore space to the total rock volume. This concept was first introduced in 2007 in regional-scale assessments of storage capacity in the United States and Europe. Since then, numerous research papers, as discussed in this article, have addressed the topic of CO_2 storage efficiency and its associated values. The calculated values for storage efficiency, as reported in the literature, exhibit a considerable range, spanning from less than 1% to over 10%. Efficiency is highly variable and depends on the specific characteristics of each reservoir and the implementation of appropriate monitoring and management techniques (BACHU, 2015).

Sáinz *et al.* (2015) presented initial studies on the efficiency and safety of CO_2 storage and showed that the results depend on dominant capture mechanisms in each specific reservoir. The authors presented four trapping mechanisms that contribute to retention: structural, capillary, solubility and mineral entrapment. The objective of this study was to evaluate the influence of the location of the injection point on the evolution of the trapping mechanisms, quantifying the CO_2 trapped in the free phase, by capillarity and dissolved. Numerical simulations showed that even small changes in injection well location can lead to different distributions between trapping mechanisms. By injecting CO_2 away from the top of the storage formation, supercritical plume migration becomes greater and "fast" capillary trapping is improved increasing storage security.

One of the primary aims of employing numerical simulations in the context of oil reservoirs and saline aquifers is to predict their behavior over their operational lifespan. An integral petrophysical characteristic used for the characterization of these porous environments is per-

meability. Permeability signifies the medium's capacity to convey fluids, and, in the context at hand, it pertains to the potential for the saline aquifer to impede the passage of gas during the injection process. In their research, Zucatelli (2016) undertook a study involving simulations of CO_2 injection and geological storage within a saline aquifer, with the objective of scrutinizing how the reservoir's performance is impacted by variations in permeability. The physical model under examination took the form of a hypothetical rectangular parallelepiped reservoir, housing an injection well at its center. The findings were assessed and elucidated, focusing on changes in pressure and gas saturation within the saline aquifer. This article concludes that both of the parameters analyzed exhibit heightened sensitivity in response to reduced permeability.

Raza *et al.* (2018) aimed to emphasize the significance of residual gas in determining the capacity, injectivity, pressurization of reservoirs, and trapping mechanisms at storage sites by employing numerical simulations. The findings revealed a direct correlation between storage performance and the quantity of residual gas present in the medium, highlighting that reservoirs with lower residual fluids are preferable for storage purposes.

To explore the impact of injection rate and timing on reservoir dynamics and storage performance, Li *et al.* (2019) designed continuous and intermittent injection scenarios with the goal of storing 1 million tons of CO_2 annually over a 30-year period. These scenarios were assessed through numerical simulations conducted in saline aquifers utilizing real field data. The findings were generally promising for most intermittent injection strategies, albeit necessitating higher injection pressures compared to continuous injection for achieving the same CO_2 storage targets. However, over the long-term, differences in capture efficiencies between intermittent and continuous injections typically fell within the 1% to 3% range.

In a recent study by Yue *et al.* (2022), it was recommended that the CO_2 injection rate in CCS projects should be meticulously assessed, taking into account the outcomes of reservoir models. Analytical analysis was proposed as a valuable approach for validating migration distances derived from numerical simulations. The presence of reservoir heterogeneity was found to augment lateral displacement while concurrently impeding vertical plume migration throughout the injection period. In the same year, Urych *et al.* (2022) introduced dynamic simulation models for CO_2 injection into saline aquifers within the Choszczno-Suliszewo structure located in northwestern Poland. Two distinct injection scenarios, each featuring different injection rates of 1 Mt CO_2/year and 2 Mt CO_2/year, were meticulously examined. This comprehensive analysis focused on assessing pressure changes and the evolving characteristics of the sequestration process. Additionally, the spatial distribution of free CO_2 saturation within the structure and dissolved carbon dioxide within the brine was visually represented. The observation period for tracking transformations within the rock mass extended up to 1,000 years after the completion of injection. The modeling of CO_2 sequestration in Early Jurassic aquifers within the Suliszewo structure successfully achieved the predetermined CO_2 injection rates for both scenarios. The sequestration process demonstrated remarkable effectiveness, primarily driven

by the phenomenon of CO_2 dissolution in the brine, resulting in the convection movement of CO_2-enriched brine. This process not only led to an expansion of CO_2 storage capacity but also resulted in the permanent, long-term retention of the injected carbon dioxide. Furthermore, the study observed the displacement of injected CO_2 from the collection layers to the layers forming the reservoir seal.

3 METHODS

In this chapter, the methodological body is presented as a six-part division, consisting of quality maps, petrophysical units, GCS classification systems as well as geologic, mathematical and computational frameworks. These frameworks respectively cover the geologic context of this study, the concepts and functions that support the qualifying process with a consistent mathematical and physical basis, and the numerical procedures needed for modeling and simulating storage sites.

Furthermore, each of these methodological parts is essential for the comprehensive understanding and accurate execution of the study. Geological structures provide the solid basis for contextual analysis, allowing a detailed assessment of the specific geological aspects that influence storage. Without this understanding of the geological context, the effectiveness of the qualification process could be compromised, resulting in inaccurate and potentially inefficient assessments.

On the other hand, the incorporation of robust mathematical and physical concepts provides a solid structure for the formulation and analysis of the models involved. This mathematical basis not only validates the methods used, but also guarantees the accuracy and reliability of the results obtained during qualification. Additionally, detailed numerical procedures provide the tools necessary to transform geological data and mathematical concepts into practical, meaningful simulations that can effectively guide storage decisions.

3.1 Quality maps: revamping an old strategy

More than two decades ago, the concept of "quality map" (QM) emerged in O&G industry to find productive areas by means of a two-dimensional representation of the reservoir responses and uncertainties. The core idea of this reduced-order approach aimed to aggregate the depth-wise dynamics of a surveyed region onto a 2D map through two main steps: i) multiple runs of flow simulations for a single well in different areal locations and ii) filling of uncovered sites by interpolation over non-simulated cells (CRUZ *et al.*, 2004).

Pioneer investigations associated QMs with concepts broadly used today, such as productivity potential (BABU; ODEH, 1989; NAKAJIMA; SCHIOZER, 2003) and quality index (MARTINI *et al.*, 2005). Although QMs could have a time-dependent representation changeable as a function of the dynamic properties captured by recurrent simulations over long time steps, this procedure reached the computational cost. Then, heuristic methods proposed another qualification perspective through proxy functions.

Proxy functions combined attributes of grid cells (petrophysical, dynamic, and geometrical) and assumed parametric forms abstracted from Darcy's law under considerations on relative productivity, oil-bearing capacity, and fluid mobility (KHARGHORIA *et al.*, 2003). Necessary adjustments to improve the correlation with flow simulation results appeared later supported by zone ranking (DAVIES *et al.*, 2006), geostatistics (GUERRA; NARAYANASAMY, 2006), artificial intelligence (MIN *et al.*, 2011), and optimization. In this last case, QMs related to productivity proxies as screening methods. One argued that proxy functions should be a compound of both time-invariant reservoir properties, such as permeability and time-varying properties, such as pressure and saturation (LIU; JALALI, 2006). Following this tenet, several dynamic measures to identify "sweet spots" appeared in the literature embedding time-of-flight, net-to-gross (TAWARE *et al.*, 2012; RAVALEC, 2012), water coning, gas cap, gas channelling, distances between the grid cells and gas-oil contact, among other parameters (DING *et al.*, 2014; DING *et al.*, 2019; POULADI *et al.*, 2020).

QMs and productivity potential intermingled over the years to produce high-fidelity models focused on well placement whose main difference were variables that composed the proxy functions. All things considered, our first assumption for this thesis is: *proxy functions formerly used to identify production sites can be revamped and adapted to create 3D (volumetric) QMs useful for qualification of CO_2 storage sites.*

3.2 Petrophysical units: static vs. dynamic

The *flow unit* (FU) concept has been a base model for delineating productive volumes in reservoirs for many years due to its ability to incorporate sorts of petrophysical and geological properties (SLATT *et al.*, 1990). Having reached an apogee because its distinguishing aspects of lateral and vertical continuity (HEARN *et al.*, 1984), internal consistency (JR, 1987; JR *et al.*, 1992), and statistical explanation (ABBASZADEH *et al.*, 1996), a FU is, in the jargon of reservoir modelers, a "volume endowed with good fluid flow properties" (CANNON, 2015).

Recently, there has been a better understanding of FUs, particularly in carbonate rocks, thanks to new concepts about the different nature of petrophysical static units and petrophysical dynamic units. A static rock type is now defined quantitatively as a group of rocks with the same primary drainage capillary pressure curves or unique water saturation for a given distance above the free water level. On the other hand, a dynamic rock type is a classification of rocks with similar fluid flow behavior. FUs are since then identified as dynamic rock types mainly because of the superior experimental performance grounded on the flow deliverability potential (MIRZAEI-PAIAMAN *et al.*, 2018; MIRZAEI-PAIAMAN *et al.*, 2019).

Analyzing the dynamics of CO_2 flow through a potential geological site is a complex challenge due to the multiple variables and processes involved. Dynamic units are a practical approach to this analysis for several reasons:

- *Multi-scale modeling*: Dynamic units allow modeling processes at different temporal and spatial scales, which is essential for understanding CO_2 migration in geological reservoirs. This includes everything from the microscopic scale (porous interactions within rocks) to the macroscopic scale (movement of CO_2 in large volumes of rocks or along fault lines).

- *Integration of geophysical and geological properties*. The dynamics of CO_2 flow is influenced by several rock properties, such as porosity, permeability, and mineral structure. Dynamic units allow you to integrate these physical and chemical properties into a cohesive model, enabling a more detailed understanding of how CO_2 behaves in a geological location.

- *Simulation of physico-chemical processes*. The flow of CO_2 in geological environments involves a series of physical and chemical processes, such as dissolution in groundwater, chemical reactions with minerals, and diffusion through pores. Dynamic units are capable of simulating these complex processes and their interactions, providing an accurate representation of the dynamics of CO_2 flow.

- *Capturing non-linearities and heterogeneities*. The geological environment is intrinsically heterogeneous and the processes that govern the flow of CO_2 are often non-linear. Dynamic units can capture these heterogeneities and non-linearities, allowing for more realistic and accurate modeling of CO_2 fluxes.

- *Response to environmental and operational changes*. During the injection of CO_2 into a geological reservoir, several changes can occur, such as variations in pressure, temperature, and chemical reactions. Dynamic units allow you to simulate these changes and predict how the CO_2 flow will respond to different operational and environmental conditions, helping to identify risks and optimize management strategies.

- *Feedbacks and feedback processes*. Interactions between CO_2, rocks and fluids in the reservoir can generate feedbacks that affect flow dynamics. For example, dissolving CO_2 in water can change the chemistry of the water and influence the reactivity of minerals. Dynamic units allow you to model these complex feedbacks, providing a comprehensive view of how processes interact over time.

- *Risk and safety assessment*. The injection of CO_2 into geological reservoirs must consider potential risks, such as the possibility of leaks or fracturing. Dynamic units allow you to simulate risk scenarios and assess the security of geological storage, helping to develop mitigation and response strategies.

In this thesis, we assume that using dynamic units as models to characterize rock volumes that have internal consistency in terms of rock-fluid interaction is a practical approach to

analyze CO_2 flow dynamics through a potential site. Our second assumption is that *the dynamic unit model is suitable for characterizing storage sites because its internal constituents describe underground volumes as disjoint compartments*.

3.3 GCS classification systems

A Geologic Carbon Storage Classification System (GCSCS) establishes protocols that shape well-segmented workflows for selecting appropriate sites and making decisions about CO_2 storage. There are different opinions on how to organize such systems, but generally, a successful subsurface container requires two main elements: i) a set of desirable geological characteristics and ii) a series of successive stages that culminate at a potential site.

When referring to a subsurface region, the former group of parameters includes three aspects: capacity, which refers to the volume of pore space available for CO_2 storage; injectivity, which measures a formation's ability to conduct fluid flow and provide quick access to the pore space; and containment, which pertains to a formation's ability to securely trap and retain the injected CO_2 for an extended period of time (COOPER *et al.*, 2009). The latter group of parameters, on the other hand, includes various terminologies presented alternatively in the literature (CARPENTER *et al.*, 2011; BACHU, 2010; GOODMAN *et al.*, 2011; CALLAS *et al.*, 2022).
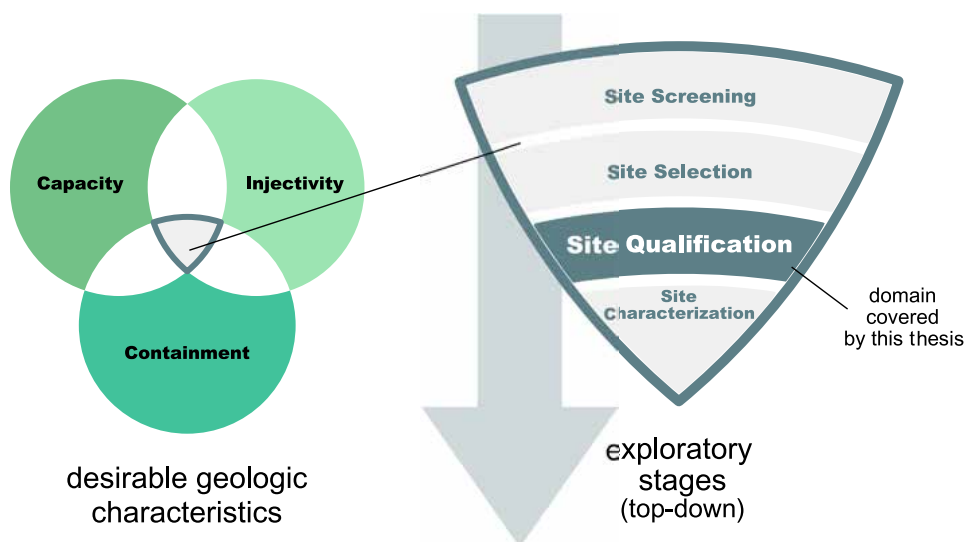
Figure 5 – Association between desirable geologic characteristics and exploratory stages of the GCS classification system adopted in this thesis.

Here, the focus falls on three main stages of GCS:

1. *Site screening*. In this stage, potential areas of interest for GCS are identified, despite the presence of uncertainty and limited data.

2. *Site selection*. In this stage, technical scores and rankings are used, usually based on additional geological information. Potential areas approved in the previous stage gain an increased level of confidence.

3. *Site characterization*. In this stage, the best-ranked sites found in the previous stage undergo detailed analyses and individual studies.

Our proposal intersperses the second and third stages through a sub-stage defined here as *site qualification* (Figure 5).

Under this viewpoint, we can define site qualification as the process dedicated to constructing measurable criteria (e.g. scores and indices) both mathematically and geologically consistent applicable to site characterization. This definition lays down the third assumption of this thesis: *mathematical functionals are appropriate to create multi-feature qualifying indices useful to support GCS modeling*.

3.4 Geologic framework

3.4.1 Reservoir model

The UNISIM-I-D model developed by CEPETRO (Center for Petroleum Studies, Unicamp, Brazil) is a crucial tool in the simulation and analysis of oil and gas reservoirs. This model, an abbreviation for "UNIversal SIMulator for I-Dimensional reservoirs", is designed to provide an accurate and efficient representation of reservoir characteristics, enabling a comprehensive assessment of different scenarios and production strategies.
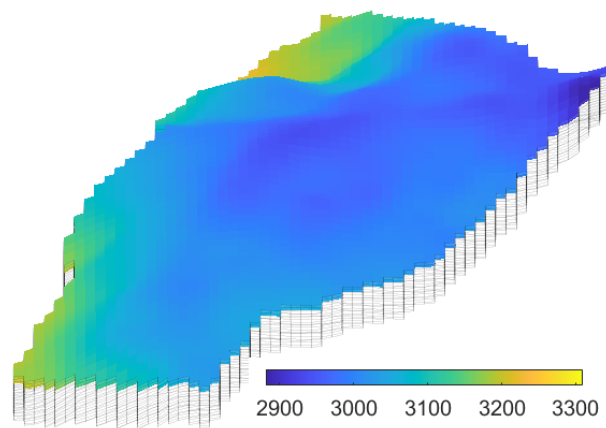
Figure 6 – 3D view of depth variation (m) of the UNISIM-I-D model. Unfilled cells represent the cropped part of the original model.

One of the distinguishing features of UNISIM-I-D is its ability to simplify the complexity of three-dimensional reservoirs into a one-dimensional representation. This is achieved by dividing the reservoir into vertical cells, allowing detailed modeling of reservoir properties, such

Table 2 – General properties of the reduced model.

Property	Value
Depth range	2900 - 3300 m
Average pore pressure	30 MPa
Maximum porosity	0.3
Water saturation	100%
Global average permeability (cf. Eq. (3.3))	2.58 mD

as permeability, porosity and fluid saturation, across depth. This simplified approach not only reduces the computational burden required for simulations, but also makes the results easier to interpret, making UNISIM-I-D a valuable tool for engineers and researchers. Furthermore, UNISIM-I-D offers a wide range of options for data entry, allowing the integration of geological and petrophysical information in a flexible and personalized way.

The model used for the current experiments is a cropped version of the UNISIM-I-D model, whose cutoff layer was placed just above the outset of the discontinuity locus existing in the original model (Figure 6). This version let us to bypass numerical limitations concerning the CO_2 flow simulation model. Its geologic characteristics are representative of the superior strata of the Namorado sandstone, a mature field located offshore in the Campos Basin, southwestern region of Brazil, predominantly formed by turbiditic deposits (AVANSI; SCHIOZER, 2015; GONZALEZ *et al.*, 2019), having reasonable properties for CGS simulations (Table 2) and has the largest theoretical storage capacity of supercritical CO_2 among Brazilian sedimentary basins (Figure 2b).

3.4.2 Trap analysis

By applying the trap analysis resource available in `MRST-co2lab` module, it is possible to visualize how spill paths, spill points, catchment regions, and traps are all hierarchically interconnected. These terms are specific to the software but useful to represent geologic entities relevant to appraisal and modeling of GCS projects (NILSEN *et al.*, 2015b; LIE, 2019).

Nilsen *et al.* (2015b) clarifies the fundamental concepts and basic algorithm for the corner-based method, which views the top surface grid as a network composed of nodes and edges, where flow occurs between nodes along the edges (Figure 7).

- The neighborhood of an internal node is defined as the node itself, along with all nodes immediately connected to it.

- The shallowest node within a neighborhood is called the local maximum.

- The relationship between a node and each of its surrounding neighbors defines a vector, with a node's upward neighbor being the one with the steepest upward slope (if any).
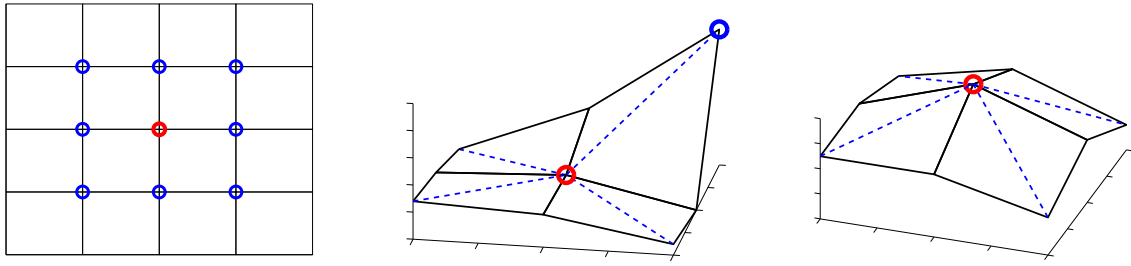
Figure 7 – *Left:* The neighborhood of an internal node consists of the node itself and its surrounding nodes. *Middle:* A node and its upslope neighbor marked blue. *Right:* a local maximum does not have any upslope node. Source: (NILSEN *et al.*, 2015b).

The link between the nodes and their neighbors on the upper slope establishes a directed tree, in which the infinitesimal flow, driven by buoyancy, travels along paths known as *spill paths*. These paths connect each node to its upslope neighbor. Each spill path culminates in a local maximum or boundary node. The spillover area of an internal local maximum is defined as all nodes on the paths leading to that maximum (Figure 8). All nodes on paths that terminate at a boundary node are assigned to the region's spillover area.
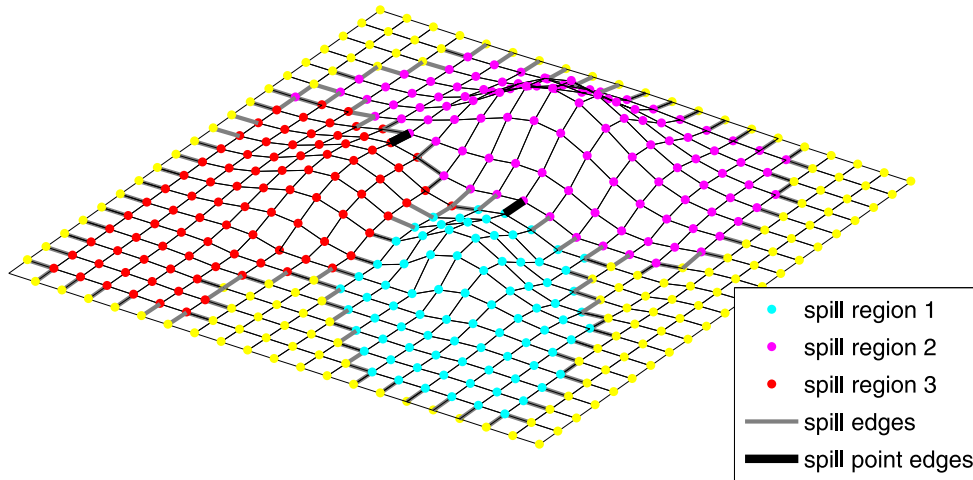
Figure 8 – Three interior and one exterior spill region with associated spill edges. The spill-point edge is the shallowest spill edge connected to a spill region. Source: (NILSEN *et al.*, 2015b).

A *spill edge* refers to an edge in the mesh that connects nodes belonging to two distinct spill regions. When CO_2 moves upward along a spill path, it may leave the domain or accumulate near a local maximum, waiting until the surface of the accumulated CO_2 reaches the shallowest spill edge of the associated spill region. This shallower edge is called the *spill point edge*, with the *spill point* being the deeper node between the two, and the corresponding depth is known as the *spill depth*. In degenerate cases, the spill point may not be unique. The area under the surface where CO_2 accumulates before reaching the spill point is identified as the *trap* associated with the local maximum. The mesh nodes contained in this trap are called *trap nodes*, thus defining the *trap region* associated with this local maximum. The remaining portion of the spill region is called the *catchment region*.

When the accumulated CO_2 reaches the spill point, it will begin to leak in a different region, following the path found upwards. If this path leads to a new local maximum, the trap from which the CO_2 leaked is said to be *upslope connected* to the trap associated with the new local maximum, with the leak path being called a *connection* or *river*. The set of traps and rivers forms a directed graph. Traps associated with different local maxima can connect to each other, resulting in cycles in this graph. This occurs when local traps constitute subpockets within a larger global capture structure (Figure 9).
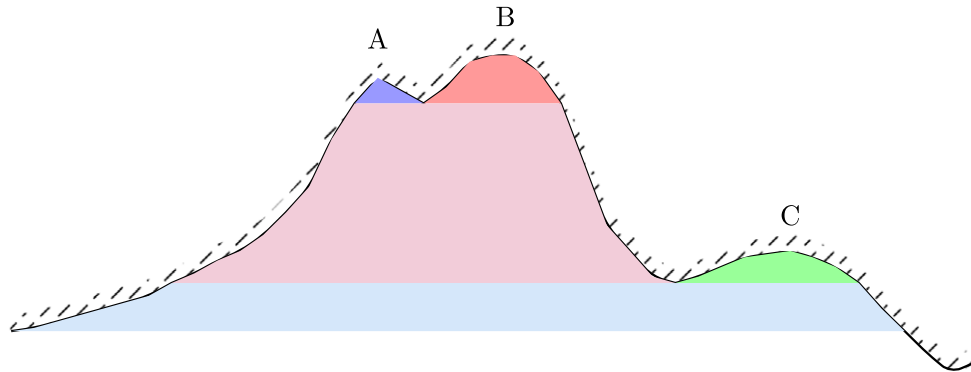
Figure 9 – Illustration of a trap hierarchy. A, B and C are local maxima with associated traps colored in blue, red and green. Trap C is upslope - connected to B, whereas A and B are upslope - connected to each other and are therefore subtraps of a larger trap AB shown in purple. Now, AB and C form local pockets of yet a larger trap structure ABC (cyan), whose spill point is at the far left of the domain. Source: (NILSEN *et al.*, 2015b).

If two or more local traps combine in this way to form a more comprehensive trap, we call them *lower-level traps*, or *subtraps*, of a *higher-level trap*. The volume of the upper level trap may be significantly greater than the combined volume of the lower level traps. The process of identifying cycles and merging traps is repeated iteratively until the graph composed of traps and rivers becomes acyclic. A trap that can no longer be merged is called a *global trap* and is either upwardly connected to another global trap or extends outside the domain. Algorithm 1 explains the step-by-step process for calculating the total volume within each trap by building a graph of nodes and their connections.

In summary, spill paths explain possible paths followed by the CO_2 buoyancy-driven flow under a sealing caprock towards its top portion and describes the path taken by CO_2 below the cover rock during its floating migration, considering an infinitesimal flow. When a trap is completely saturated with CO_2, any additional amount entering the trap will result in an equivalent amount escaping. For infinitesimal quantities, the flow will follow a spill path out of the trap, culminating in another trap or exiting the domain. In this way, it is possible to view individual traps as connected by spill paths, similar to the interconnection of lakes via rivers.

All these elementary entities form a large network of channels, "rivers", subtraps, and higher-level traps that allow us to detect migration paths, injection sites, and probable leakage points. The trap analysis over the reduced model portraits a "spider"-like network of 11 traps with variable capacity (Figure 10) and total capacity of around $1.6 \times 10^7 \, \text{m}^3$. A large top-level

(a)

(b)

(c)
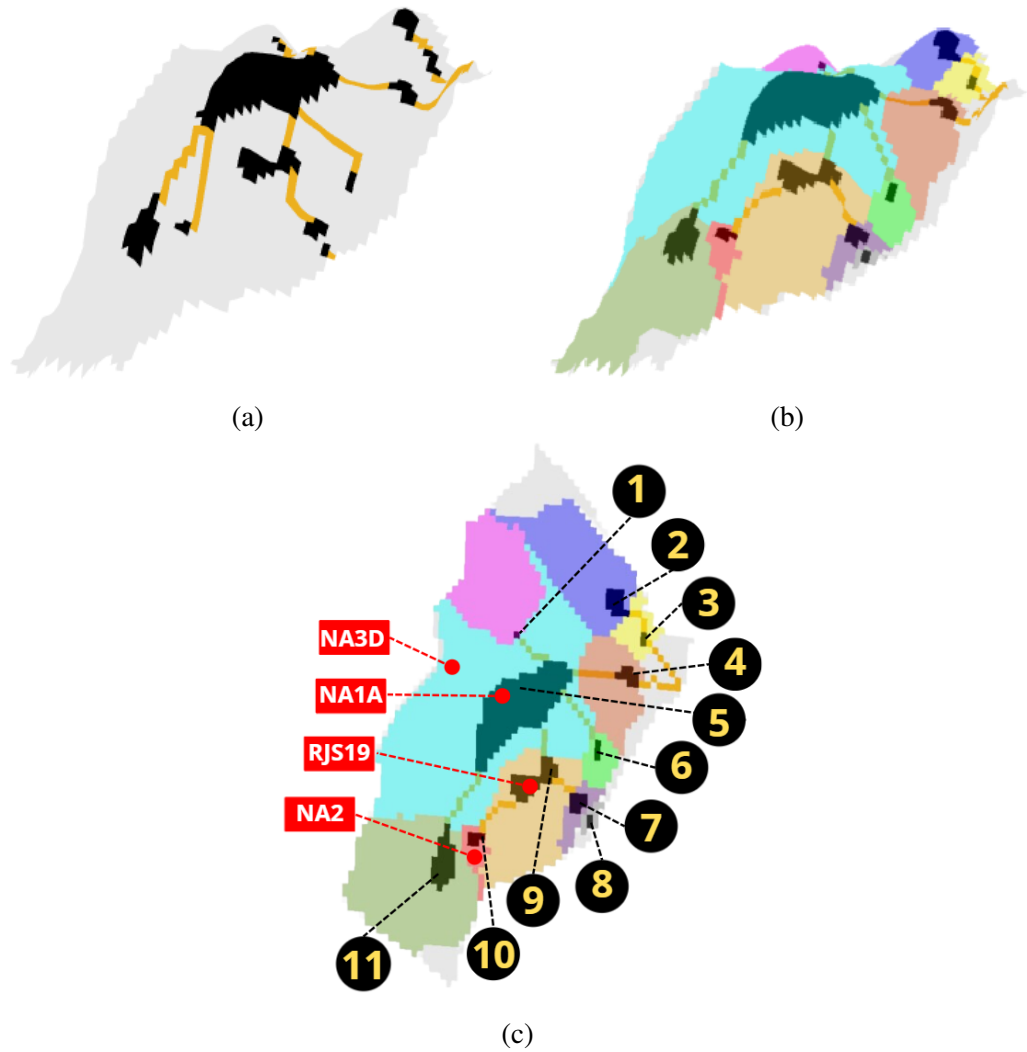
Figure 10 – Trap analysis of the reduced UNISIM-I-D model: (a) 3D view of the network of traps and rivers plotted over the top layer of the corner-point grid; (b) 3D view of the traps, rivers, and catchment regions associated to the traps; (c) top view version of (b) with numbered traps and identification of the legacy wells (in red).

trap locates at the central region of the field. Smaller satellite subtraps from second to fourth levels – in terms of a hierarchical tree – form around connecting rivers that flow into the larger trap.

3.5 Mathematical framework

Firstly, the mathematical framework provides a short theoretical background on functionals and how they apply to this thesis. Secondly, it establishes the underlying functions and parameters necessary to express the functionals. Lastly, it defines the family of qualifying functionals.

Algorithm 1 – Compute the bulk volume inside each trap (adapted by (NILSEN *et al.*, 2015b)).
Require: Construct the graph *G* of individual nodes and their connections with upslope neighbors.
Ensure: The bulk volume geometrically inside each trap.

1: Create graph *G* by depicting individual nodes and their connections to upslope neighbors. This should be done for each interior node that is not a local maximum. Eliminate connections to downslope neighbors.
2: Allocate each node to a distinct spill region.
3: Detect spill edges.
4: Allocate a spill-point edge to each spill region by selecting the highest among the spill edges that intersect the region's boundary.
5: Establish connections between local maxima by following the rivers originating from the spill-point edge(s) of each region along the spill paths defined by *G*. This process results in a new graph *H* composed of interconnected local maxima/traps.
6: Identify global traps by systematically eliminating cycles in *H* through iterations and merging the traps implicated in the process.
7: Compute the bulk volume geometrically inside each trap.

3.5.1 Theoretical synopsis on functionals

Functionals are popular in applications involving calculus of variations. Loosely speaking, a functional can be defined as a real-valued "function of functions". This means it is an mathematical entity that depends on functions as its variables, which, in turn, may depend on other variables (GELFAND; FOMIN, 1963). Functionals are often defined by integral expressions that require certain properties such as bounded variation, compactness, and continuity, but can be constructed for non-integral models under less rigid assumptions. In fact, when working with porous materials, the mathematical constraints imposed by functional theory are relaxed to some extent. This is because quantities such as porosity are defined only in the sense of a Representative Elementary Volume (BEAR, 1972). Therefore, the qualifying functionals introduced in this thesis are based on the premises of the continuum hypothesis and the nonlinear nature of the medium's properties.

As the position vector $\mathbf{x}$ on the 3D Euclidean space determines the main free variable of our applications, a functional $\mathcal{F}$ is generically expressed by the form

$$\mathcal{F}(u_1(\mathbf{x}), u_2(\mathbf{x}), \ldots, u_k(\mathbf{x})), \tag{3.1}$$

where each u_j, $j = 1, 2, \ldots, k$, is a real-valued function assumed continuous pointwise. Here, the functionals will take the similar form of a *parametric group*, built as a product of dimensional quantities. Therefore, one has that the formal definition of a qualifying functional for storage site is:

$$\mathcal{F}\colon \mathcal{V}_{\otimes,k}(\mathbb{R}^3) \to [0, +\infty)$$
$$\Pi_{j=1}^k u_j \mapsto \mathcal{F}(\Pi_{j=1}^k u_j),$$

where $\mathcal{V}_{\otimes,k}$ represents a Cartesian product of k functional spaces – where the k underlying functions lie in – and Π is the product operator. At this point, we should underline that the deep examination of the properties of these individual spaces is out of scope, as with the inspection of their operations on the ground of the mathematical analysis.

This way, a qualifying functional is an *indicator* whose input is a product of underlying functions, and the output is a single real value. However, due to the variety of physical interpretations that such indicator may have from the combination of several dimensions of its underlying functions, it is practical and suitable to construct a dimensionless normalized version for $\mathcal{F}$. A straightforward way to do that is by using the min-max rule, from which we get to

$$\mathfrak{J}(\mathbf{x}) = \frac{\mathcal{F}(\mathbf{x}) - \min(\mathcal{F}(\mathbf{x}))}{\max(\mathcal{F}(\mathbf{x})) - \min(\mathcal{F}(\mathbf{x}))}. \tag{3.2}$$

Subsection 3.5.4 expounds the practical implementation of the abstraction discussed so far in simpler notations. For the rest of the thesis, $\mathfrak{J}$ is the meaningful quantity for CO_2 storage site qualification.

3.5.2 Flow deliverability function

The *flow deliverability function* measures the quality of a formation taking into account the so-called *reservoir process speed*, *RPS*, interpreted as a factor that controls the speed of a fluid moving through a reservoir layer (OLIVEIRA *et al.*, 2022). By defining $RPS = \dfrac{\kappa}{\phi}$, where ϕ is the effective porosity, and

$$\kappa(\mathbf{x}) = \left\{ \sum_{i=1}^{3} \mathbf{K}(\mathbf{x})_{ii}^2 \right\}^{1/2}, \tag{3.3}$$

is a local average absolute permeability computed from the principal components of the permeability tensor $\mathbf{K}$, the flow deliverability function assumes the form

$$\lambda(\mathbf{x}) = 0.0314 \, [RPS(\mathbf{x})]^{1/2}, \tag{3.4}$$

where 0.0314 is a unit conversion factor from millidarcies.

Experimental results showed that λ performs better for different rock formations, in contrast with a series of other theoretical flow indicators (MIRZAEI-PAIAMAN *et al.*, 2018; MIRZAEI-PAIAMAN *et al.*, 2019; FARAMARZI-PALANGAR; MIRZAEI-PAIAMAN, 2021; MIRZAEI-PAIAMAN; GHANBARIAN, 2022). Roughly speaking, λ is a "flow potential" metric for the storage site. It is worthwhile mentioning that λ depends exclusively on space since ϕ and κ change only locally and are maintained fixed over time. That is why λ is treated here as a function instead of an index.

3.5.3 Distance-to-trap function

To locally weigh the quality of a storage site, distances are an effective way for assigning degrees of relevance to locations in the surroundings of a trap. In order to have things clearer, we defined a few entities that establish metric relations.

Let $\mathbf{x}$ be a spatial position; $d(\mathbf{x}, \mathbf{y})$ the Euclidean distance between $\mathbf{x}$ and another position $\mathbf{y}$; $\mathbf{x}_\tau$ the τ-th trap top point; $\mathbf{x}_{b;\tau}$ a position at the τ-th trap boundary; $\mathbf{x}_b$ a position at the field boundary; and $\mathbf{x}_\tau^\perp$ the normal projection of $\mathbf{x}_\tau$ on the horizontal plane tangent to the τ-th spill point.

Besides, let us consider that a catchment region embraces both the effective trap region, denoted by $\mathcal{T}$, and the complementary trap region below the spill point of the respective trap, denoted by $\mathcal{T}^c$. The effective trap region is the pocket where CO_2 will get withheld, whereas the complementary trap region is a transitional flow region. Since the injectable gaseous mass is limited by the effective trap capacity, it is appropriate to define the *trap volume ratio* as

$$\upsilon = \begin{cases} \dfrac{\text{vol}(\mathcal{T})}{\text{vol}(\mathcal{T}^c)}, & \text{if } \mathcal{T}^c \neq \emptyset \\ \dfrac{\text{vol}(\mathcal{T})}{\sum_{\tau=1}^{n_\tau} \text{vol}(\mathcal{T}_\tau)}, & \text{otherwise,} \end{cases} \tag{3.5}$$

where vol stands for "volume". One expects that $\upsilon < 1$ because the effective trap volume usually is higher than the transitional region volume. Once established, these quantities allow us to define a *distance-to-trap function* by a generic form given by

$$\beta(\mathbf{x}; p_1, p_2, \ldots, p_m), \tag{3.6}$$

which depends on space and a finite number of m parameters. Below are defined the three β-functions proposed (Figure 11):

$$\beta_1(\mathbf{x}; d_1) \quad := \quad \underset{1 \leq \tau \leq n_\tau}{\text{mean}} \{\beta_{1,\tau}(\mathbf{x}; d_1)\} \tag{3.7}$$

$$\beta_2(\mathbf{x}; \upsilon, d_1, d_2, n_\tau) \quad := \quad \underset{1 \leq \tau \leq n_\tau}{\text{mean}} \{\beta_{2,\tau}(\mathbf{x}; \upsilon, d_1, d_2, n_\tau)\} \tag{3.8}$$

$$\beta_3(\mathbf{x}; d_1, d_3) \quad := \quad \underset{1 \leq \tau \leq n_\tau}{\text{mean}} \{\beta_{3,\tau}(\mathbf{x}; d_1, d_3)\} \tag{3.9}$$

where

$$\beta_{1,\tau}(\mathbf{x}; d_1) \quad := \quad \begin{cases} 1 & , \text{ if } 0 < d_1 \leq 1, \\ \dfrac{1}{\log(d_1)} & , \text{ otherwise,} \end{cases} \tag{3.10a}$$

$$\beta_{2,\tau}(\mathbf{x}; \upsilon, d_1, d_2, n_\tau) \quad := \quad -\dfrac{1}{1 + \dfrac{1}{\upsilon} \exp\left[-\left(\dfrac{d_1 - d_2}{n_\mathcal{T}}\right)\right]}, \text{ and} \tag{3.10b}$$

$$\beta_{3,\tau}(\mathbf{x}; d_1, d_3) \quad := \quad \exp\left(-\dfrac{d_1}{d_3}\right). \tag{3.10c}$$

(a)

(b)
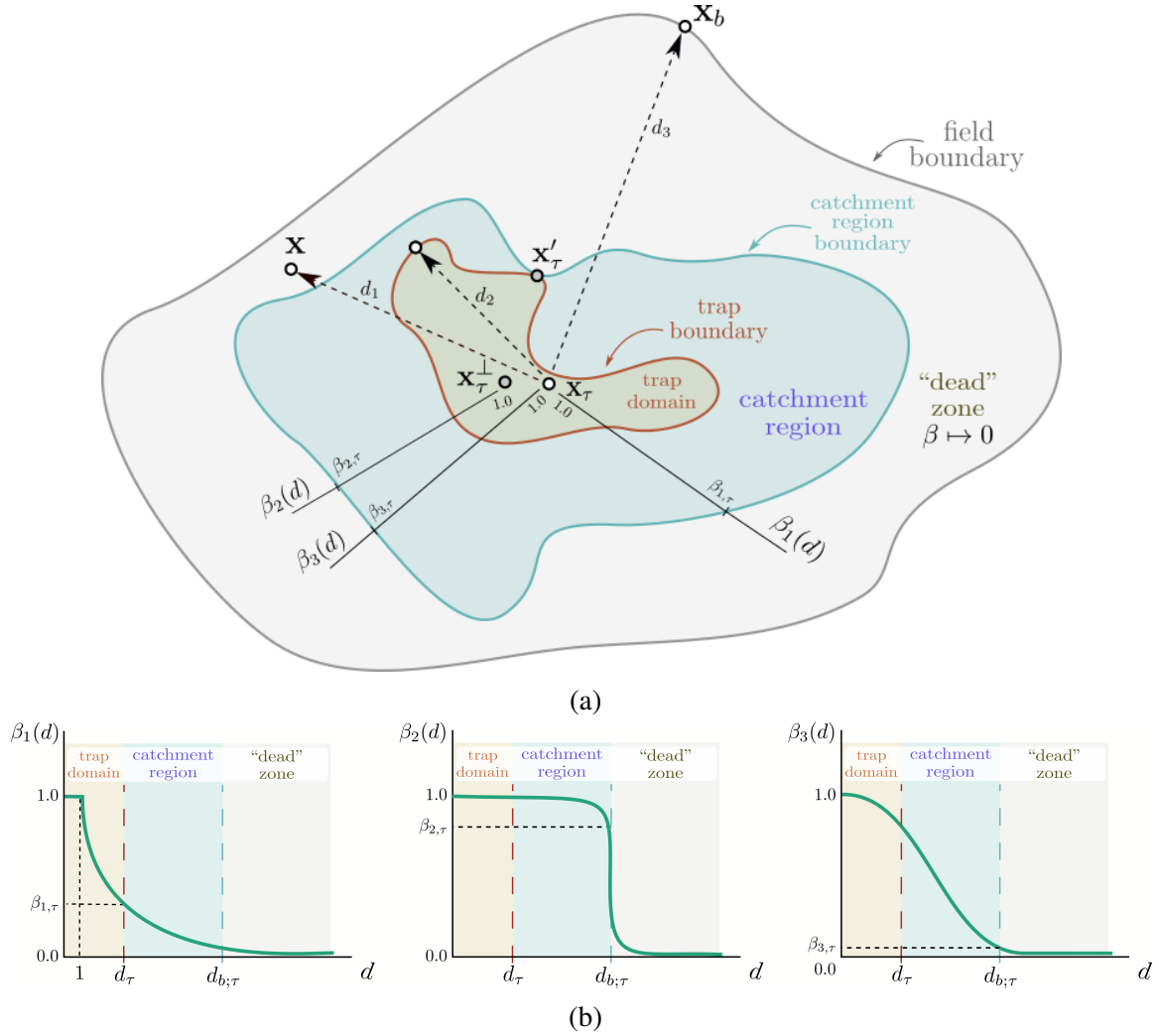
Figure 11 – Reduced-order schemes (out of scale) illustrating how the distance-to-trap functions are applied over the 3D model for an individual trap: (a) projection view of domains and isolines of the β functions. At the trap top ($\mathbf{x}_\tau$), or at its projection ($\mathbf{x}_\tau^\perp$) in case of β_2 only, any β function assumes a unit value — 100% of weighting effect over the functional — and decays asymptotically to zero at the "dead zone" – quasi-null weighting effect. (b) 1D representation β functions embodied in a few functionals (cf. Eqs. 3.12a - 3.12i). When applied over the whole field, they generate smoothly decaying isosurfaces as a function of distances computed in relation to $\mathbf{x}_\tau$ or $\mathbf{x}_\tau^\perp$ that behave in the following manner: inverted logarithm with small plateau near the trap top (β_1); logistic with abrupt jump around the catchment region boundary (β_2); and hybrid logistic (β_3).

Aside υ and the number of traps $n_{\mathcal{T}}$, the other parameters appearing in Eqs. (3.10a-3.10c) are:

$$d_1 = d(\mathbf{x}, \mathbf{x}_\tau), \ \mathbf{x} \neq \mathbf{x}_\tau, \tag{3.11a}$$

$$d_2 = \max_{1 \leq \tau \leq n_{\mathcal{T}}} \{d(\mathbf{x}_\tau^\perp, \mathbf{x}_{b;\tau})\}, \text{ and} \tag{3.11b}$$

$$d_3 = \max_{1 \leq \tau \leq n_{\mathcal{T}}} \{d(\mathbf{x}_\tau, \mathbf{x}_b)\}. \tag{3.11c}$$

As an illustration, we plotted the scattering of $\beta_{3,\tau}$ computed for two individual traps and of β_3 (Figure 12).
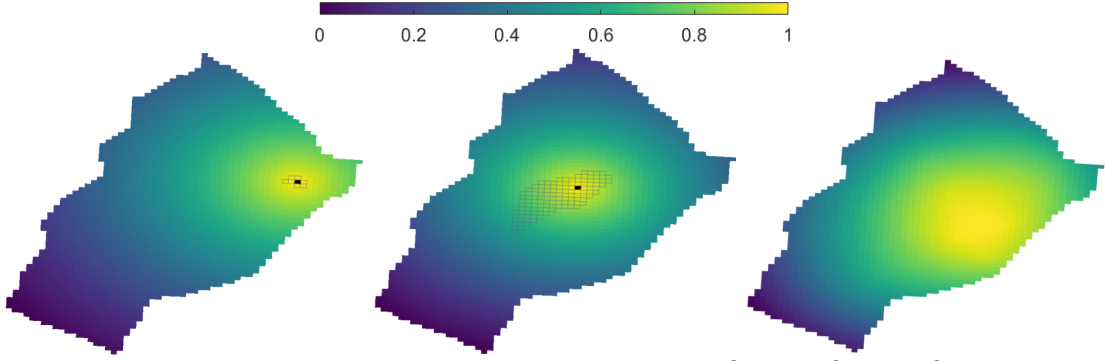
Figure 12 – Top view of the scattering over the grid model of: (a) $\beta_{3,4}$; (b) $\beta_{3,5}$; (c) β_3. The cell marked in black and the wireframe, where they appear, indicate the grid column which the trap's top lies and the projection of the trap volume onto the uppermost grid layer, respectively. As seen, these distance-to-trap functions create isosurfaces whose weighting value decays outward from the trap.

3.5.4 Qualifying functionals

As discussed in subsection 3.5.1, the derivation of a qualifying functional depends uniquely on its composition of functions. Beyond the flow deliverability function and the distance-to-trap functions, other commonplace quantities are admissible as underlying functions. This way, the family of qualifying functionals proposed here is the following:

$$\mathcal{F}_1(\mathbf{x}) \quad := \quad \phi(\mathbf{x})\kappa(\mathbf{x})s_w(\mathbf{x}), \tag{3.12a}$$

$$\mathcal{F}_2(\mathbf{x}) \quad := \quad \lambda(\mathbf{x})s_w(\mathbf{x})p(\mathbf{x}), \tag{3.12b}$$

$$\mathcal{F}_3(\mathbf{x}) \quad := \quad \mathcal{F}_2(\mathbf{x})\beta_1(\mathbf{x}), \tag{3.12c}$$

$$\mathcal{F}_4(\mathbf{x}) \quad := \quad \mathcal{F}_2(\mathbf{x})\beta_2(\mathbf{x}), \tag{3.12d}$$

$$\mathcal{F}_5(\mathbf{x}) \quad := \quad \mathcal{F}_2(\mathbf{x})\beta_3(\mathbf{x}), \tag{3.12e}$$

$$\mathcal{F}_6(\mathbf{x}) \quad := \quad s_w(\mathbf{x})p(\mathbf{x})\log(\kappa(\mathbf{x}))\log(d(\mathbf{x},\mathbf{x}_b)), \tag{3.12f}$$

$$\mathcal{F}_7(\mathbf{x}) \quad := \quad \mathcal{F}_6(\mathbf{x})\beta_1(\mathbf{x}), \tag{3.12g}$$

$$\mathcal{F}_8(\mathbf{x}) \quad := \quad \mathcal{F}_6(\mathbf{x})\beta_2(\mathbf{x}), \tag{3.12h}$$

$$\mathcal{F}_9(\mathbf{x}) \quad := \quad \mathcal{F}_6(\mathbf{x})\beta_3(\mathbf{x}), \tag{3.12i}$$

where s_w is the water saturation function and p is the pore pressure function. Noteworthy points necessary for enlightenment regarding Eqs. (3.12a-3.12i) are:

- *Unavailability of injectivity functionals.* To the best of the authors' knowledge, the literature lacks qualifying indicators grounded on a consistent mathematical basis when one takes CO_2 injection into account. This fact led us to adapt a few methods formerly used for assessing productivity potential to injectivity potential scores. As a result, Eqs. (3.12a) and (3.12f), inspired after (KHARGHORIA *et al.*, 2003) and (LIU; JALALI, 2006) respectively, are assumed as benchmarks, since they differ from the original form only by the water saturation, which replaces the oil saturation.

- *Inherited benchmarks.* Because $\mathcal{F}_1$ is a form inherited from the literature, the functionals from $\mathcal{F}_2$ to $\mathcal{F}_5$ are proposed as its direct competitors. It turns out that $\mathcal{F}_2$ acts upon $\mathcal{F}_3$, $\mathcal{F}_4$ and $\mathcal{F}_5$ as a nuclear group intended to verifying if the addition of the flow deliverability function and the pore pressure interfere for better qualification in terms of injectivity potential. As supplementary part, the β-functions weigh the functionals by infusing the distance-to-trap factor. Likewise, $\mathcal{F}_6$ is a second benchmark extracted from the literature that adds a log-regularity on the permeability field and on the interior field locations taking the boundary into account. In turn, the presence of another nuclear group in $\mathcal{F}_7$, $\mathcal{F}_8$, and $\mathcal{F}_9$ propose that these three last functionals are tested in contrast with $\mathcal{F}_6$ equally from the the distance-to-trap factor. Ultimately, all these functionals are propositions equally testable for site qualification.

- *Physical interpretation and nondimensionality.* Eq. 3.12a is a "transport potential", a measure of the capacity of the porous medium to transport fluid, influenced by properties such as permeability, porosity and saturation. Eq. 3.12b provides a combined metric that captures the flow capacity of the porous medium, the force driving the flow, and fluid availability, offering an estimate of the potential for injection or movement of fluids in the reservoir. Eq. 3.12f combines the flow capacity of the porous medium, the driving force of the flow, the presence of fluids and the transport efficiency over distance, and can be used to estimate and compare the injection potential of different zones, adjusting the influence of factors based on distance and linearizing the analysis through the permeability logarithm. Eqs. 3.12c-3.12e and Eqs. 3.12g-3.12i are used to estimate and compare the potential injectivity of different zones taking into account the influence of distance on fluid transport efficiency. If carefully inspected as for their dimension, it becomes clear that the functionals can transmit different meanings. By taking SI units, for instance, one verifies that $\mathcal{F}_1$, $\mathcal{F}_3$, and $\mathcal{F}_6$, in this order, could resemble area, force, and momentum. On the other hand, neither there is plausibility in choosing the (most) correct unit, nor comparing the performance of the functionals by their physical sense. Therefore, the functionals are made dimensionless and normalized.

- *Normalization and the $\mathfrak{J}$-forms.* As explained in the previous point, it is quite convenient to work with dimensionless and normalized functionals, so that its output value limits to the unit interval instead of $[0,+\infty)$. This process is conducted by Eq. (3.2), after which the $\mathfrak{J}$-forms remain unitless. Despite of that, we only consider the strictly positive values, i.e. $(0,1]$, for practical reasons, since 0 means null quality.

- *Pore pressure normalization.* One knows that the CO_2 injectable for permanent storage should be in a supercritical state. To reach this condition, the depth and in-situ pore pressure at the storage site should be, respectively, around $1000\,m$ and $7.39\,MPa$. This way,

for functionals that contain the pore pressure, Eq. (3.2) succeeds Eq. (3.13):

$$\bar{p}(\mathbf{x}) = \frac{p(\mathbf{x}) - p_{crit}}{\max\{p(\mathbf{x})\} - p_{crit}}, \tag{3.13}$$

where p_{crit} is the critical pressure, here fixed at 7.39 MPa (VESELY *et al.*, 2019).

- *Static and dynamic quantities*. The functionals are hybrid entities that absorb both static (porosity, permeability and distances) and dynamic (saturation and pressure) quantities, each of them treated as a function. Currently, we consider functionals at a fixed time instant, allowing them to vary only over space.

3.6 Computational framework

This section explains the discrete procedures for implementing the qualifying functionals computationally. To convert the concepts defined in the preceding subsections from continuum domains to discrete ones, the required change is the replacement of the spatial point notation $\mathbf{x}$ by the grid cell notation c. From that point on, the rationale for the novel technicalities introduced in this section results from progressive advancements extensively discussed in a series of earlier papers (OLIVEIRA *et al.*, 2016; ROQUE *et al.*, 2017; OLIVEIRA *et al.*, 2020; OLIVEIRA *et al.*, 2022)).

3.6.1 Grid description

The reduced model is represented by a complex cell-based corner-point grid denoted by

$$\overline{\Omega} = \{c_{(i,j,k)}; 1 \leq i \leq I, \ 1 \leq j \leq J, \ 1 \leq k \leq K\}, \tag{3.14}$$

for $I = 81$, $J = 58$, and $K = 4$ of cell extension over the 3D discrete domain $\overline{\Omega}$, with centroid $c_{(i,j,k)}$, $n_p = 8083$ active cells, and average pore volume of around $1.33 \times 10^4 \, \text{m}^3$. The porosity varies between 0.0 and 0.3 (Figure 13).

3.6.2 Discrete dynamic units and injectivity unit classes

A discrete dynamic unit (DDU) reflects a petrophysical dynamic unit (cf. section 3.2) under the discrete viewpoint. Each DDU is a set of cells of the computational grid that covers a region where the formation is statistically similar. They represent the physical containers where CO_2 injection wells should be placed for potential injectivity.

Injectivity unit class (IUC) is a set of one or more disjoint DDUs. The purpose of a class is to assign a single positive integer value to its members, so that they classify regions according
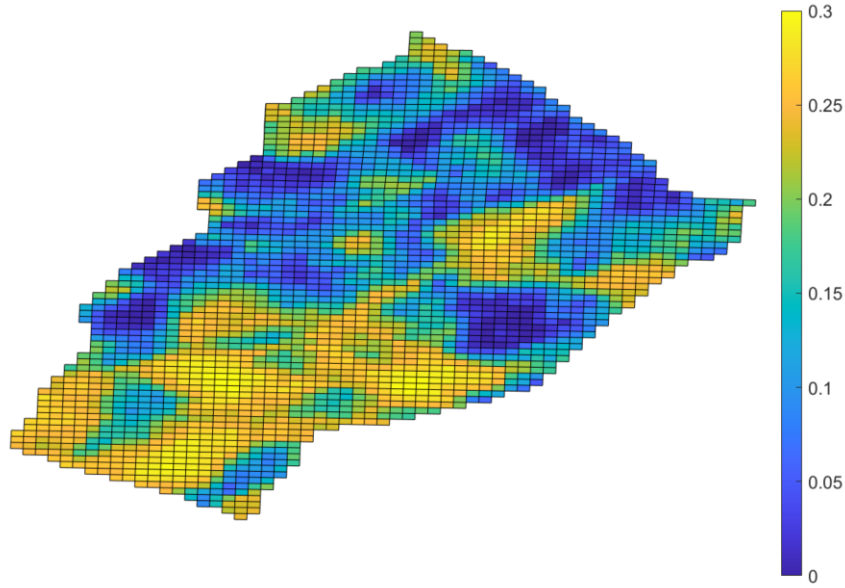
Figure 13 – Top surface view of the porosity field of the reduced model.

to the volumetric quality map quantitatively determined by a $\mathfrak{J}$-functional. The IUCs will rank the volumes for well placement, making them qualified sites after a binning transform like

$$\text{IUC}(c) = B(\mathfrak{J}(c)), \ \ \forall c \in \overline{\Omega}, \tag{3.15}$$

where IUC is the class label and B is a statistical method that creates partitions over the distribution of $\mathfrak{J}$ over all grid cells. In other words, the number of IUCs is equivalent to the number of bins of a histogram and the bin edges are the classification boundaries for the DDUs.

The transform of the $\mathfrak{J}$-distribution into IUCs employs a binning algorithm that creates class intervals automatically (Figure 14). Here, B matches one of the following options: `scott` (SCOTT, 2015); `freedman-diaconis` (FREEDMAN; DIACONIS, 1981); `sturges` (STURGES, 1926); or `sqrt` (DAVIES *et al.*, 1947).

- `Scott`'s rule is optimal if the data is close to being normally distributed, but is also appropriate for most other distributions. It uses a bin width of

$$B(\mathfrak{J}) = 3.5\sigma(\mathfrak{J})(\#\mathfrak{J})^{-1/3}, \tag{3.16}$$

where σ is the standard deviation and $\#\mathfrak{J}$ is the number of elements in $\mathfrak{J}$;

- `Freedman-Diaconis` (`fd`) rule is less sensitive to outliers in the data, and may be more suitable for data with heavy-tailed distributions. It uses a bin width of

$$B(\mathfrak{J}) = 2\,\text{IQR}(\mathfrak{J})(\#\mathfrak{J})^{-1/3}, \tag{3.17}$$

where IQR is the interquartile range;

- `Sturges`' rule is a simple rule that is popular due to its simplicity. It chooses the number of bins to be

$$B(\mathfrak{J}) = \lceil 1 + \log_2(\#\mathfrak{J}) \rceil, \tag{3.18}$$

where $\lceil \; \rceil$ rounds up the next integer (ceiling function);

- The Square Root (`sqrt`) rule is another simple rule widely used in other software packages.

$$B = \lceil \sqrt{\#\mathfrak{J}} \rceil. \tag{3.19}$$
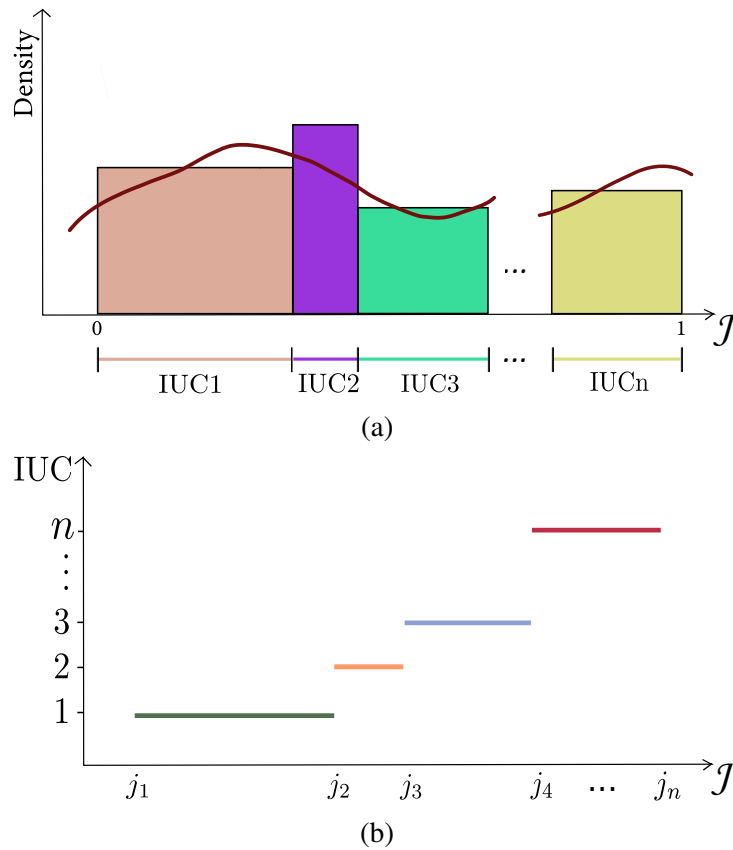
Figure 14 – Example of binning method applied to the distribution of a functional $\mathfrak{J}$: (a) histogram bins of injectivity unit classes (IUCs) overlaid by the density curve; (b) integer function resulting from the binning transform by Eq. (3.15).

In essence, Eq. (3.15) represents a classifier function that will generate up to N finite classes. It is desirable that N is small so that the number of injection sites and the "statistical power" balance each other to avoid excessive numerical simulations. The interpretation of this statistical power for our purposes is in the ability of the binning method to provide enough explainability of the distribution (see subsection 3.6.5).

3.6.3 *Injection site and well placement*

The IUCs lead to DDU partitions of cells whose $\mathfrak{J}$ values vary within a short range. The DDUs, in turn, become identifiable as smaller storages (clusters) defined by

$$C_{D,q} := \{c;\ \mathrm{IUC}(c) = D \text{ and } c \in N_6(c_s)\}, \tag{3.20}$$

where $q = 1, 2, \ldots, Q$ is the cluster index and N_6 is a 6-neighbor face-connected aggregator used to produce connectivity among cells belonging to the same IUC. Each cluster can comprise a distinct number of interconnected cells, represented by n_q. Consequently, $C_{D,q}$ represents either a constituent portion of or a unique DDU.

We associated the storage $C_{D,q}$ to a graph $G_{D,q}$ through a one-to-one function $\mathcal{G}$

$$\begin{aligned} \mathcal{G} &: C_{D,q} \to G_{D,q} \\ c_q^i &\mapsto v_q^i, \end{aligned} \tag{3.21}$$

that maps a cell of the storage onto a node of the graph, thus establishing a connectivity entanglement among the neighboring cells (Figure 15).
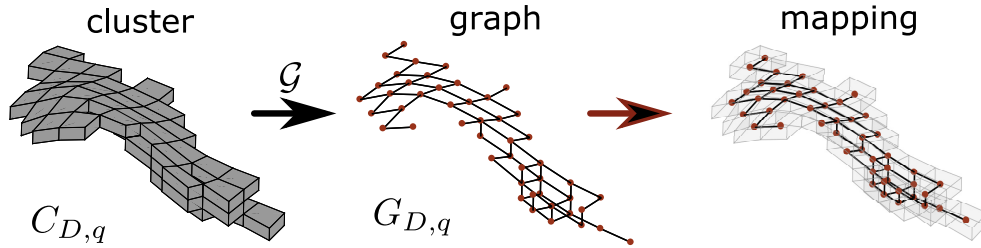
Figure 15 – Cluster-to-graph mapping for a storage site: $C_{D,q}$ is a cluster formed by face-connected grid cells mapped onto nodes of a graph $G_{D,q}$. The vertices math the cell centroids and the edges establish flux connectivity. Source: (OLIVEIRA *et al.*, 2021).

As with the clusters are used to model a volumetric injection site, we employed the metric known as *closeness centrality* to determine the exact injection well placement. The closeness centrality of each node $v_q \in G_{D,q}$ is computed as

$$\gamma(v_q) = \frac{1}{\displaystyle\sum_{i=1}^{\eta_\lambda} d(v_q, v_n)}, \quad \forall v_n \in G_{D,q},\ v_n \neq v_q, \tag{3.22}$$

where $d(v_q, v_n)$ is the shortest path distance between v_q and v_n (FREEMAN, 1978; NEWMAN, 2010). The closeness centrality relates to a communication control and interpreted here as a potential injection site for well placement.

However, since the γ values change per node, we computed the *maximum closeness centrality* (MCC) of the cluster $C_{D,q}$ to determine a single well placement locus that features the bottom hole point (Figure 16).
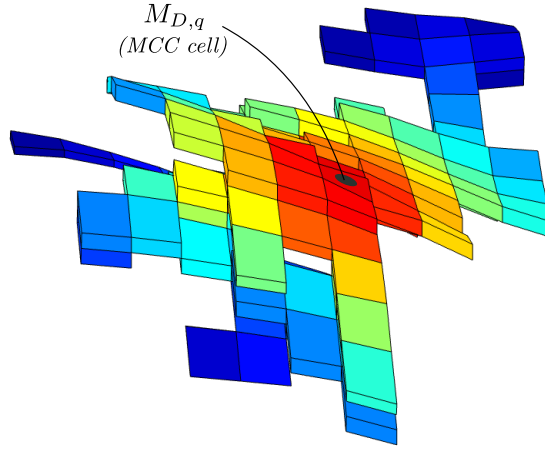
Figure 16 – Closeness centrality (γ) distribution over a hypothetical cluster. It varies from lower values (colder colors) to higher values (hotter colors) within the unit interval. The black dot indicates the maximum closeness centrality cell ($M_{D,q}$).

3.6.4 Volumetric quality map

The ideas formulated so far give rise to the definition of a volumetric quality map (VQM) directed to CO_2 storage site qualification. A VQM is a tuple formed by a qualifying functional, a binning method, and a collection of DDUs determined by IUCs and its respective clusters. In full form, a VQM is a triplet like $(\mathfrak{J}, B, \{C_{d,q}\})$. Once $\mathfrak{J}$ is fixed and B is variable, the collection $\{C_{d,q}\}$ becomes, in fact, a response to these two presets.

We can express a VQM as a leaf of a combinatorial tree headed by the qualifying functional at the first level and the binning method at the second level. Both unwrap the IUCs and DDUs into a third and fourth levels. This way, the elements that form a VQM are equivalent to field regions with different scores that may be potential storage sites.

By making an ordered correspondence of integer indices for the VQM's elements to facilitate the computational manipulation, one concludes that a VQM can be alternatively written as:

$$VQM_{j,b} := \{S_{j,b,d,q}\}, \tag{3.23}$$

for $j = 1, 2, \ldots 9$ enumerating the normalized versions of the qualifying functionals introduced in Eqs. (3.12a - 3.12i), $b = 1, \ldots, 4$ enumerating the binning methods – scott, fd, sturges and sqrt, in this order –, d enumerating the IUCs, and q enumerating the clusters as defined in Eq. (3.20). As such, $\{S_{j,b,d,q}\}$ represents a collection of single storage sites described by a given functional and a binning method (Figure 17).

3.6.5 Intersecting sites

Due to the statistical nature of the binning methods, it is possible that two or more elements correspond to the same physical storage site – at least by a minimum threshold of volume

(a)

(b)

(c)
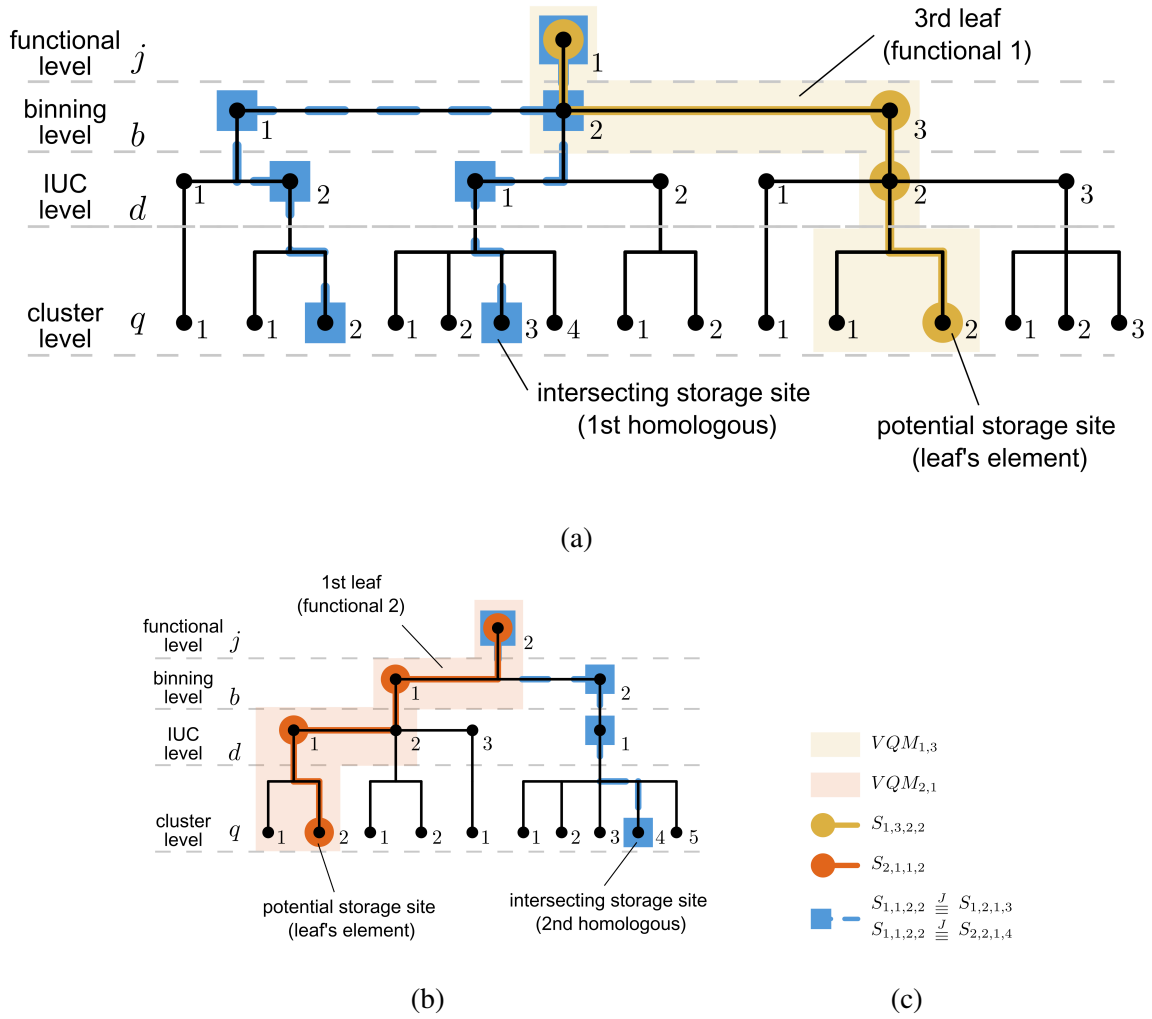
Figure 17 – (a) Illustrative scheme of a combinatorial tree for a hypothetical functional (denoted by 1) highlighting its third leaf and an homologous site; (b) Illustrative scheme of a combinatorial tree for a second hypothetical functional (denoted by 2) highlighting its first leaf and another homologous site; (c) Legend written in formal notation according to Eq. (3.23). The symbol $\overset{J}{\equiv}$ stands for "equivalent by Jaccard". Hierarchical view of a small combinatorial tree formed by two functionals: (a) the first functional ($j = 1$), alongside three binning methods ($b = 1, 2, 3$), anchors 3 VQMs (shaded stripe in light yellow) and a varying number of IUCs and clusters per VQM. In total, it returns 15 storage sites; (b) the second functional ($j = 2$), alongside two binning methods ($b = 1, 2$), anchors 2 VQMs (shaded stripe in light orange) and a varying number of IUCs and clusters, summing ten storage sites. Among all 25 storage sites, two are equivalent by Jaccard to $S_{1,1,2,2}$ (connected lines in blue) and negligible for simulation. It turns out that the storage sites (elements), generically denoted by $S_{j,b,d,q,}$, are the endpoints of minor branches that make up a leaf. Also, the union of single combinatorial trees form a highly complex structure of leafs and elements when one organizes all the functionals and binning methods.

coverage – even though they lie in distinct VQMs (Figure 17a and Figure 17b). In case of existing homologous elements in other VQMs, the intersections are eliminated by removal of circular dependencies. A circular dependence occurs when some homologous yield intersections in the VQMs (Figure 18).

The technique implemented in this thesis to eschew intersecting VQMs resorts to the Jaccard index. The Jaccard index J measures the similarity between storage sites (VQM elements) based on their cell indices (JACCARD, 1912). Here, it is defined as

$$J(S_{j_1,b_1,d_1,q_1}, S_{j_2,b_2,d_2,q_2}) = \frac{\#(S_{j_1,b_1,d_1,q_1} \cap S_{j_2,b_2,d_2,q_2})}{\#(S_{j_1,b_1,d_1,q_1} \cup S_{j_2,b_2,d_2,q_2})}, \tag{3.24}$$

for $S_{j_1,b_1,d_1,q_1} \in VQM_{j_1,b_1}$ and $S_{j_2,b_2,d_2,q_2} \in VQM_{j_2,b_2}$. The numerator of this fraction is the number of cells of the intersection set between the two elements, whereas the denominator is the number of cells of the union of both elements. Given that $0 \leq J \leq 1$, we imposed that two elements yield circular dependence if their J value is higher than J^*, where J^* is the 3rd quartile of the distribution of all Jaccard numbers calculated for VQMs' elements (Figure 18). This threshold enforces that pairs of storage sites with high stratigraphic coverage by a volume percentage above J^* should be treated as identical and considered as a single site. Consequently, all the elements homologous to a leading element in the hierarchy of the combinatorial tree are neglected for further analysis. The positive effect of the Jaccard filtering is the reduction of computer simulations.
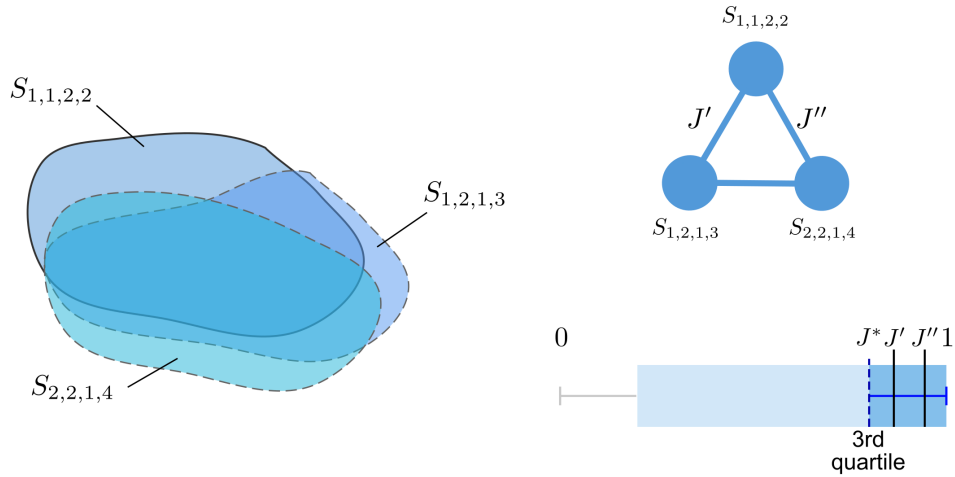
Figure 18 – Scheme depicting how intersecting storage sites are identifiable and its application to the case of Figure 17. The intersecting sites $S_{1,1,2,3}$, $S_{1,2,1,3}$, and $S_{2,2,1,4}$ cover, two-by-two, the same volume (left) at a given extension and create a "circular dependence" portrayed by a simple graph (top right). The threshold for the volume coverage stems from the Jaccard index J, which varies from 0, when there is no intersection between two elements, to 1, when they match exactly (bottom right). In this example, $J' = J(S_{1,1,2,3}, S_{1,2,1,3})$ and $J'' = J(S_{1,1,2,3}, S_{2,2,1,4})$. Both overcome the threshold J^*, taken as the third quartile of all Jaccard indices computed for viable pairs of elements within the tree. Viable pairs are those formed by elements belonging to different VQMs.

3.6.6   Fluid flow model

The processes of CO_2 injection and migration are approximated by the interaction of brine (aqueous) and supercritical gas phases indicated by w and g, respectively. The fluid flow

dynamics is modeled by the multiphase version of the mass conservation equation coupled to the Darcy's flux model, resulting on the following set of equations

$$\frac{\partial(\phi\rho_\alpha s_\alpha)}{\partial t} + \nabla \cdot (\rho_\alpha \mathbf{u}_\alpha) = \rho_\alpha q_\alpha \tag{3.25a}$$

$$\mathbf{u}_\alpha = \kappa\lambda_\alpha(\nabla p_\alpha - \rho_\alpha \mathbf{g}) \tag{3.25b}$$

$$\sum_\alpha s_\alpha = 1, \quad \alpha = w, g, \tag{3.25c}$$

where ρ is the fluid density, s is the fluid saturation, $\mathbf{u}$ is the fluid velocity, q is the volumetric flux from any source or sink, λ is the mobility, and $\mathbf{g}$ is the gravitational acceleration (LIE, 2019).

Equations 3.25a-3.25c are firstly integrated vertically by assuming that the fluid phases are subject to hydrostatic equilibrium and totally segregated. One admits that CO_2 and brine are separated by a sharp interface and each vertical column of the aquifer is divided into a three-zone model as follows (Fig. 19):

- gas plume zone of thickness h, where CO_2 flows freely. Here, CO_2 saturation is $1 - s_{w,r}$ and brine saturation is $s_{w,r}$.

- residual zone of thickness $h_{max} - h$, where brine re-invades the pore space previously occupied by the plume. In this zone, CO_2 residual saturation is $s_{g,r}$ and brine saturation is $1 - s_{g,r}$.

- brine only zone of thickness $H - h_{max}$, where H is the aquifer thickness.

Vertically-averaged quantities for permeability, mobility and Darcy fluxes define the so-called h-formulation of the vertical equilibrium (VE) model, for which a transport equation is numerically solved by an explicit method. See the Appendix B for more details.

3.6.7 Trapping mechanisms

Using a sharp-interface VE model (see Appendix B) allows for accurate carbon trapping inventories for specific scenarios, detailing how injected CO_2 volumes are divided into safely contained parts and those that might potentially leak back to the surface. Over time, CO_2 becomes more securely trapped due to various trapping processes occurring at different rates, ranging from days to thousands of years.

When CO_2 is injected into a deep subsurface rock formation, it forms a separate, typically dense phase (the CO_2 plume) that displaces other liquids in the pore space (usually brine). Since the CO_2 phase is almost always less dense than the resident fluids, it will rise and be replaced by other fluids. However, as the CO_2 volume fraction falls below a certain level, capillary pressure from the other fluids traps the CO_2 in the pore space between rock grains, preventing
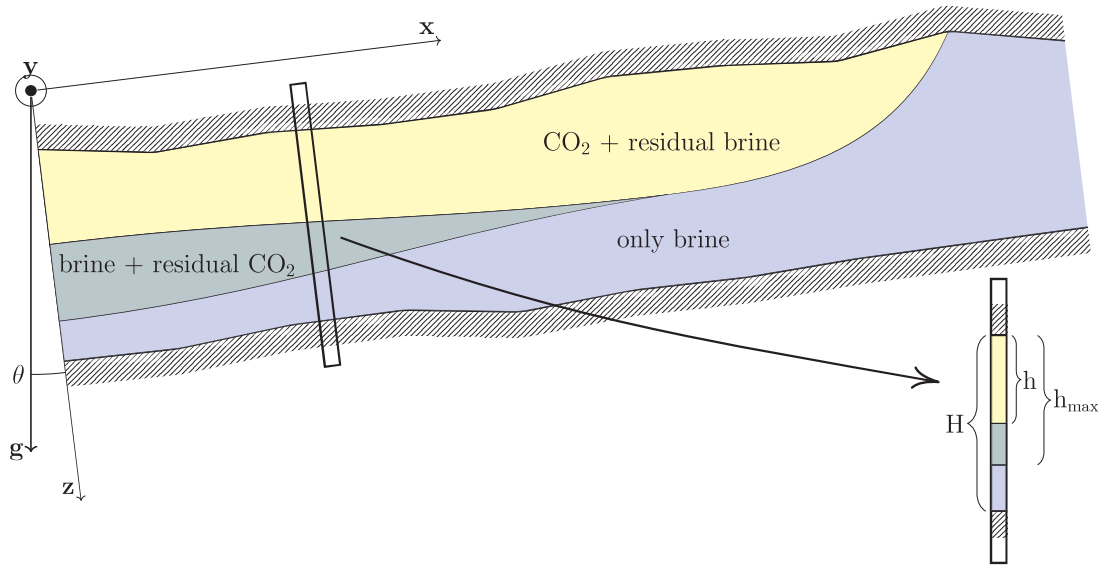
Figure 19 – Overview of the sharp-interface three-zone description for the vertical equilibrium (VE) model adopted here under a generalized configuration tilted by θ. h, h_{max}, and H divide a vertical column, thus defining the plume, residual plume and brine regions over the aquifer thickness. The top and bottom dashed areas represent impermeable walls (sealing rock). Source: (NILSEN *et al.*, 2017).
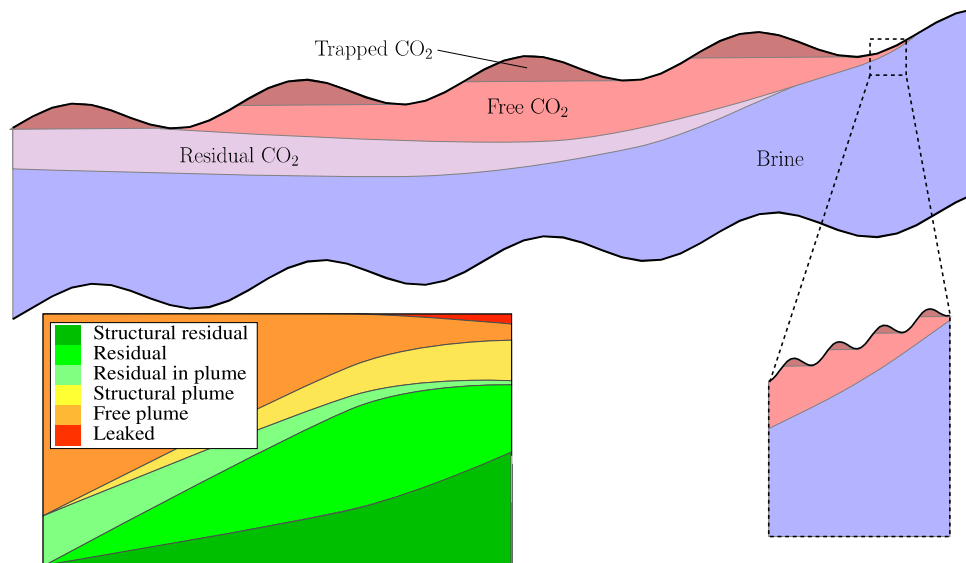
Figure 20 – Schematic of a vertical section of an aquifer showing the different ways in which injected CO_2 may be present during migration (adapted from (NILSEN; LIE; ANDERSEN, 2016)).

further movement. This process, known as residual trapping, results in CO_2 volumes categorized as *residual* in the inventory. Thus, the plume inventory is divided into two categories: *residual in plume*, representing the CO_2 fraction that will remain residually trapped when the plume moves, and *free plume*, which is the remaining part free to migrate from its current position.

In most relevant scenarios, CO_2 is injected beneath a sealing rock where the capillary pressure within pore throats exceeds the buoyancy pressure of the CO_2. This top seal prevents the plume from moving directly upward. If the seal is sloped, the CO_2 will form a thin layer underneath, gradually migrating upslope until it encounters a structural trap, such as a fold in the

top surface where the CO_2 will accumulate. Once inside a trap, the CO_2 remains structurally trapped unless the plume height creates enough capillary pressure to penetrate the seal. The structurally trapped volumes are categorized into two types: *structural residual*, which will stay immobile and never leak, and *structural plume*, which could potentially escape through a crack in the top seal. Once a trap fills, the CO_2 will spill over and continue migrating upward. To summarize, the *structural residual* and *residual* volumes are securely stored unless changes in the aquifer alter the residual saturation of CO_2. The *structural plume* volumes are immobilized and safely stored unless the structural traps have leakage points. The remaining volumes will continue migrating upslope. The *residual in plume* volumes will eventually become residually trapped, while the *free plume* volumes may leak if not trapped by another mechanism later. In the inventory shown in Figure 19, the various CO_2 volume categories are stacked by increasing leakage risk, from structural residual CO_2 (darker green) to volumes still plume (yellow/orange) or those that have already left the simulated domain (red). Each volume type is detailed below:

- *Structural residual volume*. CO_2 both residually and structurally trapped. The volume (V_{R_1}) is given by

$$V_{R_1} = \sum_{\mathbf{x} \in \bigcup \tau} s_{Rc}(pv)_{\mathbf{x}}, \tag{3.26}$$

  where s_{Rc} is the residual CO_2 saturation, pv is the pore volume and τ is a trap.

- *Residual volume (not structural)*: CO_2 residually (but not structurally) trapped, outside the free-flowing zone. The volume (V_{R_2}) is given by

$$V_{R_2} = \left[\sum_{\mathbf{x} \notin \bigcup \tau} \max(h_{\max} - \max(\hat{\mathbf{x}}, h_{\mathbf{x}}))(pv)_{\mathbf{x}} \right] s_{Rc}, \tag{3.27}$$

  where s_{Rc} is the residual CO_2 saturation and $\hat{\mathbf{x}} = \min(d(sp_\tau, \mathbf{x}), H_{\mathbf{x}})$, with sp_τ is the spill point of trap τ.

- *Residual in plume volume*: CO_2 still inside the free-flowing zone residually (but not structurally) trapped. The volume (V_{R_3}) is given by

$$V_{R_3} = \left[\sum_{\mathbf{x} \notin \bigcup \tau} (h_{\mathbf{x}} \cdot (pv)_{\mathbf{x}}) - (\min(\hat{\mathbf{x}}, h_{\mathbf{x}}) \cdot (pv)_{\mathbf{x}}) \right] s_{Rc}, \tag{3.28}$$

- *Structural plume volume*: CO_2 structurally (but not residually) trapped. The volume (V_{SP}) is given by

$$V_{SP} = \left[\sum_{\mathbf{x} \in \bigcup \tau} (\min(\hat{\mathbf{x}}, h_{\mathbf{x}}) \cdot (pv)_{\mathbf{x}}) \right] (1 - s_{Rw} - s_{Rc}), \tag{3.29}$$

  where s_{Rw} is the residual brine saturation.

- *Free plume volume*: CO_2 neither structurally nor residually trapped. The volume (V_{FP}) is given by

$$V_{FP} = \left[\sum_{\mathbf{x} \notin \bigcup \tau} (h_{\mathbf{x}} \cdot (pv)_{\mathbf{x}}) - \sum_{\mathbf{x} \notin \bigcup \tau} (\min(\hat{\mathbf{x}}, h_{\mathbf{x}}) \cdot (pv)_{\mathbf{x}}) \right] (1 - s_{Rw} - s_{Rc}), \tag{3.30}$$

where s_{Rc} is the residual CO_2 saturation and s_{Rw} is the residual brine saturation.

- *Leaked volume*: CO_2 escaped outward the simulated domain. The leaked volume (V_L) is given by

$$V_L = V_T - (V_{R_1} + V_{R_2} + V_{R_3} + V_{SP} + V_{FP}), \tag{3.31}$$

where V_T is the total injected volume.

4 RESULTS

In this chapter, a comprehensive overview of the results is presented, encompassing the identification of potential storage sites for each functional and the development of a volumetric quality map. The methodology employed involves Sobol sensibility analysis and Jaccard filtering, which assesses the number of intersection sites for each functional, contributing to a nuanced understanding of storage possibilities. The numerical simulations conducted using the `MRST-co2lab` simulator further enhance the reliability of the results.

The simulations were executed at each potential storage site, considering parameter values recommended in the existing literature. This approach ensures a robust foundation, aligning the study with established scientific principles. The use of the `MRST-co2lab` simulator adds a layer of sophistication to the analysis, allowing for a detailed exploration of the potential storage sites' viability. The results, elucidated for each functional, provide valuable insights into the dynamics of CO_2 storage. The focus extends to the existing wells of the UNISIM-I-D model, contributing to a holistic understanding of the interplay between various factors influencing storage outcomes. Notably, the analysis includes a meticulous examination of the percentage of residual CO_2 storage over a significant temporal spans, specifically 15, 30, 50 and 100 years post-injection and 1985, 1970, 1950 and 1900 years of plume migration, respectively.

By delving into the residual storage percentages, the study sheds light on the long-term effectiveness and sustainability of CO_2 storage at the identified sites. This temporal analysis is crucial for assessing the feasibility of these sites over extended periods, aligning with the need for sustainable carbon capture and storage strategies.

The chapter's emphasis on the UNISIM-I-D model, with their characteristics and legacy wells, provides a benchmark for evaluating the results against an established framework. This comparative approach enhances the applicability and reliability of the findings, fostering a deeper understanding of the potential storage sites' performance. The integration of numerical simulations and consideration of established parameter values contribute to the robustness of the findings, laying the groundwork for informed decision-making in the realm of carbon capture and storage.

4.1 Sobol sensibility analysis

Sobol sensitivity analysis (SSA) is a technique used in modeling and simulation to understand the relative importance of different input variables in relation to the model output. It allows decomposing the total variance of the model output into individual contributions of each input variable and their interactions (SOBOL, 2001).

SSA is especially useful when there are a large number of input variables and complex interactions between them. It provides a deeper understanding of the relationships between variables and helps us to identify which variables have the greatest impact on the model output (SALTELLI, 2002; SALTELLI *et al.*, 2010). SSA belongs to the Global Sensitivity Analysis (GSA) group, in which all model inputs vary simultaneously over the entire input range (SOBOL, 1993; SALTELLI, 2002). The contribution of the inputs to the model output and their interaction can be estimated using Equation 4.1:

$$D(\mathcal{F}) = \sum_i D_i + \sum_{i<j} D_{ij} + \sum_{i<j<k} D_{ijk} + D_{12...d_p} \tag{4.1}$$

where $D(\mathcal{F})$ represents the total variance or total effect on the model output, D_i indicates the first-order variance contribution, and D_{ij} signifies the second-order variance contribution, also known as the interaction between input parameters. Additionally, the remaining terms in Equation 4.1 represent higher-order interactions up to d_p (the total number of input parameters in the model). The first-order and total-order sensitivity indices are defined by equations 4.2 and 4.3 , respectively:

$$S_i = \frac{D_i}{D} \tag{4.2}$$

$$ST_i = 1 - S_i \tag{4.3}$$

The benefit of using the SSA method is that it considers the relationships between the model inputs and output, encompassing all input parameters and their interactions (ZHANG *et al.*, 2015; KUMAR *et al.*, 2020). Let us consider the model given by Equation 3.1. The input variables $X_1,\ldots,X_p$ represent the input variables having known probability distribution, and the model output is represented by Y which is a scalar. The decomposition nature of Sobol method converts output variance into contributed input factor. To estimate the relative influence of an input factor on the model output, the X_i is fixed as X_i^*, considering conditional variance $V_{\overline{X_i}}(Y \mid X_i = X_i^*)$, where $\overline{X_i}$ denotes all the inputs except X_i and also $E_X(Y)$ as the conditional expectation of X in relation to Y (PAPOULIS, 2002). The law of total variance (Equation 4.1) is the basic framework of Sobol method, which can be clearly seen in Equation 4.4:

$$V(Y) = V_{X_i}\left(E_{\overline{X_i}}(Y \mid X_i)\right) + E_{X_i}\left(V_{\overline{X_i}}(Y \mid X_i)\right) \tag{4.4}$$

After normalization,

$$1 = \frac{V_{X_i}\left(E_{\overline{X_i}}(Y \mid X_i)\right)}{V(Y)} + \frac{E_{X_i}\left(V_{\overline{X_i}}(Y \mid X_i)\right)}{V(Y)} \tag{4.5}$$

The first term of Equation 4.5 represents the first-order effect (FOE) for the parameter X_i, i.e.,

$$S_i = \frac{V_{X_i}\left(E_{\overline{X_i}}(Y \mid X_i)\right)}{V(Y)} \tag{4.6}$$

The second term of Equation 4.5 denotes second-order effect (SOE). The SOE represents the interaction of the factors (X_i and X_j) contributed to model output Y (i.e., sensitivity to X_i and X_j not expressed in V_i nor V_j) as in Equation 4.7.

$$S_{ij} = \frac{V_{ij}}{V(Y)} \tag{4.7}$$

and, by Homma and Saltelli (1996), the total-order sensitivity (ST_i) is defined as

$$ST_i = 1 - \frac{E_{\overline{X_i}}\left(V_{X_i}\left(Y \mid \overline{X_i}\right)\right)}{V(Y)} \tag{4.8}$$

Table 3 presents the Sobol sensibility analysis of the functionals $\mathcal{F}_1$-$\mathcal{F}_9$ (Eqs. 3.12a and 3.12i). Permeability κ (also incorporated in λ according to the Equation 3.4) has a greater influence compared to other parameters. Furthermore, there is no influence of pressure. Some justifications for this are the linearity of the distribution, the assumption of vertical equilibrium in the simulation and the short depth range of the reduced UNISIM-I-D, resulting in a small pressure variation.

Table 3 – Sobol sensibility analysis of the functionals $\mathcal{F}_1$-$\mathcal{F}_9$.

$\mathcal{F}_1$:

Parameters	S_1	ST
ϕ	0.01	0.01
κ	0.99	0.99

$\mathcal{F}_2$:

Parameters	S_1	ST
λ	1	1
p	0.00	0.00

$\mathcal{F}_3$:

Parameters	S_1	ST
λ	0.98	0.99
p	0.00	0.00
β_1	0.01	0.01

$\mathcal{F}_4$:

Parameters	S_1	ST
λ	0.48	0.60
p	0.00	0.00
β_2	0.40	0.51

$\mathcal{F}_5$:

Parameters	S_1	ST
λ	0.92	0.94
p	0.00	0.00
β_3	0.05	0.07

$\mathcal{F}_6$:

Parameters	S_1	ST
p	0.00	0.01
$\log \kappa$	0.58	0.80
$\log d$	0.19	0.40

$\mathcal{F}_7$:

Parameters	S_1	ST
p	0.00	0.00
$\log \kappa$	0.58	0.81
$\log d$	0.18	0.40
β_1	0.00	0.00

$\mathcal{F}_8$:

Parameters	S_1	ST
p	0.00	0.00
$\log \kappa$	0.47	0.75
$\log d$	0.14	0.36
β_2	0.07	0.22

$\mathcal{F}_9$:

Parameters	S_1	ST
p	0.00	0.00
$\log \kappa$	0.57	0.81
$\log d$	0.18	0.40
β_3	0.00	0.01

Regarding the influence of β-functions (Eqs. 3.10a-3.10c), it is possible to observe from the Table 3 that β_2 has a greater influence in relation to β_1 and β_3, evidenced by the greater S_1 and ST, that is, the logistic function (β_2) contributes significantly more compared to the inverted logarithmic function (β_1) and the logistic function β_3. This can be justified by the fact that β_2 has a value very close to 1 in both the trap and the catchment region, reaching a value close to the maximum for a larger number of cells.

4.2   Quality map generation

By constructing the complete combinatorial tree for the VQMs, a total of 36 leaves and 1450 possible storage sites were systematically generated. However, a meticulous filtering

process, guided by Eq. (3.24) for intersection removal, led to the selection of 184 sites for subsequent simulation. This culling process resulted in an absolute ratio of 12.7% (184 out of 1450) for the harnessing of potential storage sites (refer to Table 4 for detailed information). This careful selection ensures that the simulated sites are representative of a diverse range of conditions, enhancing the reliability and applicability of the ensuing analysis.

Table 4 – Detailed counting of storage sites per functional and volumetric quality map. The column denoted by $\#V_{j,b}$ indicates the number of storage sites of the VQM generated by the j-th functional and b-th binning method. The following columns, namely $\#S_j^H$, $\#S_j^J$ and e_j stand for the number of intersecting sites (homologous) for the j-th functional and all binning methods, the number of remaining potential storage sites after the Jaccard filtering, and the relative ratio of potential storage site harnessing.

j	$\#V_{j,1}$	$\#V_{j,2}$	$\#V_{j,3}$	$\#V_{j,4}$	$\#S_j^H$	$\#S_j^J$	e_j
1	32	17	41	12	348	25	7.2%
2	8	8	62	0	80	10	12.5%
3	10	0	72	0	50	7	14.0%
4	47	24	93	3	314	37	11.8%
5	12	1	70	0	66	7	10.6%
6	16	16	52	1	132	18	13.6%
7	39	11	39	1	168	41	24.4%
8	21	21	50	4	198	24	12.1%
9	12	12	38	0	94	15	16.0%
				Total	1450	184	

4.3 Numerical simulations

In order to conduct numerical simulations focused on CO_2 injection across the identified 184 potential storage sites, a meticulous setup of the `MRST-co2lab` simulator was undertaken. This setup involved configuring rock-fluid properties and numerical parameters in alignment with established literature, ensuring the simulations adhere to recognized standards and practices.

The placement of injection wells across each site was determined utilizing Eq. (3.22), which specifically designates the MCC cell within the corresponding cluster, representative of a potential storage site. This approach ensures a systematic and representative allocation of injection wells across the diverse range of potential storage conditions identified in the earlier stages of the study.

Each MCC cell is assigned a single well for the injection process, responsible for pumping CO_2 into the geological formation. The well allocation, detailed in Table 5, outlines the key properties and parameters associated with each injection well, emphasizing the specificity and consistency maintained throughout the simulation process.

This systematic approach to simulation setup and well placement is integral to the reliability and robustness of the subsequent analyses. It ensures that the numerical simulations

capture the inherent complexities of the identified potential storage sites, providing a foundation for in-depth insights into the dynamics of CO_2 injection and storage. For more details regarding relative permeability, see Appendix A.

Table 5 – Simulation setup used in `MRST-co2lab` for all numerical experiments.

Parameter	Value
Residual brine saturation	0.11
Residual CO_2 saturation	0.21
Brine viscosity	0.3086 cP
CO_2 viscosity	0.0566 cP
Brine density	975.86 kg/m^3
CO_2 density	686.54 kg/m^3
Brine relative permeability	0.2142
CO_2 relative permeability	0.8500
Gravity acceleration	9.8066 m/s^2
CO_2 injection rate	$0.1417 \cdot 10^6$ m^3/year
Injection time span	15-30-50-100 years
Migration time span	1985-1970-1950-1900 years
Average well bottomhole depth	3090 m

4.3.1 Injection performance

The numerical outputs of VQM and potential storage sites tested are detailed per injection periods (Tables 7 - 10). Among all, the best injection performances, i.e. those with the highest residual trapping proportions, were collected, summarized, and used for benchmarking. The color scheme employed should be interpreted as six different categories (Table 6) of CO_2 storage inventory states (NILSEN *et al.*, 2015a). For comparative analysis of the CO_2 containment performance, we consider the residual sum $\sum_{i=1}^{3} R_i$, where each R_i refers to a type of residual.

Table 6 – Default CO_2 storage inventory states and their description according to the `MRST-co2lab`.

State	Description	Color
Structural residual (R_1)	CO_2 both residually and structurally trapped	
Residual (R_2)	CO_2 residually (but not structurally) trapped, outside the free-flowing zone	
Residual in plume (R_3)	CO_2 still inside the free-flowing zone residually (but not structurally) trapped	
Structural plume (SP)	CO_2 structurally (but not residually) trapped	
Free plume (FP)	CO_2 neither structurally nor residually trapped	
Leaked (L)	CO_2 escaped outward the simulated domain	

Below we have the CO_2 inventory resulting from numerical simulations. Tables 7-10 presents the results referring to wells W that represent the largest group with nodes connected by functional (Group 1). Tables 11-14 presents the results referring to the W wells that represent the second largest group with nodes connected by functional (Group 2) and Tables 15-18 presents the results referring to the W wells that represent the third largest group with nodes connected by functional (Group 3).

Table 7 – Group 1: CO_2 inventory resulting from 15 years of injection plus 1985 years of migration.

Well	R_1	R_2	R_3	$\sum R_i$	SP	FP	L
$W_{3,1,26,1}$	13.49	43.54	0.64	**57.67**	39.56	2.07	0.70
$W_{7,1,12,2}$	13.94	42.23	0.69	**56.86**	40.91	2.23	0.00
$W_{2,1,31,1}$	13.94	42.23	0.69	**56.86**	40.91	2.23	0.00
$W_{6,3,12,1}$	13.46	42.44	0.62	**56.52**	39.45	2.01	2.01
$W_{4,1,8,1}$	13.49	41.80	0.61	**55.90**	39.52	1.98	2.60
$W_{8,1,6,1}$	14.38	40.14	0.76	**55.28**	42.26	2.46	0.00
$W_{9,1,17,1}$	14.47	39.81	0.75	**55.03**	42.54	2.43	0.00
$W_{5,1,24,1}$	14.69	38.29	0.89	**53.87**	43.26	2.87	0.00
$W_{1,1,1,8}$	15.24	36.12	0.87	**52.23**	44.95	2.82	0.00
legacy NA2	15.02	34.10	1.63	**50.76**	43.96	5.28	0.00
RJS19	17.25	23.82	1.56	**42.63**	52.31	5.06	0.00
NA3D	16.22	21.89	0.00	**38.11**	42.30	0.00	19.59
NA1A	20.42	17.62	0.00	**38.04**	61.96	0.00	0.00

Table 8 – Group 1: CO_2 inventory resulting from 30 years of injection plus 1970 years of migration.

Well	R_1	R_2	R_3	$\sum R_i$	SP	FP	L
$W_{3,1,26,1}$	15.16	36.11	0.94	**52.21**	44.73	3.05	0.00
$W_{6,3,12,1}$	15.26	35.54	0.95	**51.75**	45.06	3.08	0.12
$W_{4,1,8,1}$	15.36	35.07	0.96	**51.38**	45.37	3.09	0.16
$W_{7,1,12,2}$	15.48	34.63	0.97	**51.08**	45.76	3.15	0.00
$W_{2,1,31,1}$	15.48	34.63	0.97	**51.08**	45.76	3.15	0.00
$W_{8,1,6,1}$	15.65	33.81	1.00	**50.46**	46.31	3.23	0.00
$W_{9,1,17,1}$	15.73	33.50	0.99	**50.23**	46.56	3.22	0.00
$W_{5,1,24,1}$	15.69	33.44	1.05	**50.17**	46.44	3.39	0.00
$W_{1,1,1,8}$	16.18	31.33	1.06	**48.58**	48.00	3.42	0.00
legacy NA2	15.94	30.39	1.64	**47.97**	46.71	5.32	0.00
RJS19	17.57	22.37	1.57	**41.51**	53.41	5.08	0.00
NA3D	17.51	19.15	0.00	**36.66**	47.30	0.00	16.04
NA1A	20.84	15.11	0.00	**35.95**	64.05	0.00	0.00

Table 9 – Group 1: CO_2 inventory resulting from 50 years of injection plus 1950 years of migration.

Well	R_1	R_2	R_3	$\sum R_i$	SP	FP	L
$W_{3,1,26,1}$	15.99	31.99	1.09	**49.07**	47.42	3.52	0.00
$W_{6,3,12,1}$	16.08	31.56	1.09	**48.74**	47.72	3.54	0.00
$W_{4,1,8,1}$	16.18	31.15	1.10	**48.42**	48.02	3.56	0.00
$W_{7,1,12,2}$	16.24	30.85	1.11	**48.20**	48.22	3.58	0.00
$W_{2,1,31,1}$	16.24	30.85	1.11	**48.20**	48.22	3.58	0.00
$W_{5,1,24,1}$	16.30	30.44	1.14	**47.88**	48.42	3.70	0.00
$W_{8,1,6,1}$	16.34	30.37	1.12	**47.83**	48.54	3.62	0.00
$W_{9,1,17,1}$	16.41	30.10	1.12	**47.63**	48.75	3.62	0.00
$W_{1,1,1,8}$	16.69	28.76	1.15	**46.61**	49.66	3.73	0.00
legacy NA2	16.78	26.96	1.66	**45.40**	49.24	5.36	0.00
RJS19	17.88	21.08	1.57	**40.53**	54.38	5.09	0.00
NA3D	18.85	16.33	0.00	**35.17**	52.99	0.00	11.84
NA1A	21.19	12.93	0.00	**34.12**	65.88	0.00	0.00

Table 10 – Group 1: CO_2 inventory resulting from 100 years of injection plus 1900 years of migration.

Well	R_1	R_2	R_3	$\sum R_i$	SP	FP	L
$W_{9,1,17,1}$	16.41	30.10	1.12	**47.63**	48.75	3.62	0.00
$W_{3,1,26,1}$	16.90	27.40	1.24	**45.54**	50.44	4.02	0.00
$W_{6,3,12,1}$	16.97	27.09	1.24	**45.31**	50.66	4.03	0.00
$W_{4,1,8,1}$	17.04	26.80	1.25	**45.09**	50.88	4.04	0.00
$W_{7,1,12,2}$	17.08	26.62	1.25	**44.95**	51.00	4.05	0.00
$W_{2,1,31,1}$	17.08	26.62	1.25	**44.95**	51.00	4.05	0.00
$W_{5,1,24,1}$	17.06	26.59	1.27	**44.92**	50.97	4.11	0.00
$W_{8,1,6,1}$	17.13	26.37	1.26	**44.76**	51.17	4.07	0.00
$W_{1,1,1,8}$	17.34	25.42	1.27	**44.04**	51.85	4.12	0.00
legacy NA2	18.04	20.99	1.70	**40.72**	53.78	5.49	0.00
RJS19	18.41	18.29	1.60	**38.30**	56.51	5.19	0.00
NA3D	20.62	11.47	0.00	**32.09**	62.21	0.00	5.70
NA1A	21.57	9.62	0.00	**31.19**	68.81	0.00	0.00

Table 11 – Group 2: CO$_2$ inventory resulting from 15 years of injection plus 1985 years of migration.

	Well	R_1	R_2	R_3	$\sum R_i$	SP	FP	L
	$W_{2,1,13,1}$	6.37	50.45	6.36	**63.18**	16.20	20.59	0.03
	$W_{1,1,1,3}$	7.24	48.24	6.22	**61.70**	18.13	20.15	0.02
	$W_{5,1,23,1}$	13.91	40.71	1.09	**55.70**	40.76	3.53	0.00
	$W_{3,1,28,1}$	14.40	39.44	0.92	**54.75**	42.27	2.97	0.00
	$W_{8,1,15,1}$	15.04	35.82	1.54	**52.40**	42.61	4.99	0.00
	$W_{4,1,8,3}$	15.65	33.50	1.09	**50.23**	46.25	3.52	0.00
	$W_{9,1,20,2}$	15.72	33.46	1.03	**50.20**	46.48	3.32	0.00
	$W_{6,1,18,1}$	15.58	33.44	1.11	**50.13**	46.05	3.60	0.22
	$W_{7,1,10,6}$	20.55	18.25	0.00	**38.80**	61.20	0.01	0.00
legacy	NA2	15.02	34.10	1.63	**50.76**	43.96	5.28	0.00
	RJS19	17.25	23.82	1.56	**42.63**	52.31	5.06	0.00
	NA3D	16.22	21.89	0.00	**38.11**	42.30	0.00	19.59
	NA1A	20.42	17.62	0.00	**38.04**	61.96	0.00	0.00

Table 12 – Group 2: CO$_2$ inventory resulting from 30 years of injection plus 1970 years of migration.

	Well	R_1	R_2	R_3	$\sum R_i$	SP	FP	L
	$W_{2,1,13,1}$	6.17	42.32	8.44	**56.93**	15.31	27.33	0.43
	$W_{1,1,1,3}$	6.90	40.87	8.35	**56.12**	16.58	27.03	0.27
	$W_{5,1,23,1}$	15.09	35.67	1.13	**51.89**	44.45	3.67	0.00
	$W_{3,1,28,1}$	15.43	34.63	1.04	**51.09**	45.55	3.36	0.00
	$W_{8,1,15,1}$	15.83	31.88	1.54	**49.25**	45.75	5.00	0.00
	$W_{4,1,8,3}$	16.20	30.93	1.13	**48.27**	48.06	3.67	0.00
	$W_{6,1,18,1}$	16.19	30.94	1.15	**48.27**	48.02	3.71	0.00
	$W_{9,1,20,2}$	16.33	30.49	1.12	**47.93**	48.45	3.62	0.00
	$W_{7,1,10,6}$	20.93	15.74	0.00	**36.67**	63.33	0.00	0.00
legacy	NA2	15.94	30.39	1.64	**47.97**	46.71	5.32	0.00
	RJS19	17.57	22.37	1.57	**41.51**	53.41	5.08	0.00
	NA3D	17.51	19.15	0.00	**36.66**	47.30	0.00	16.04
	NA1A	20.84	15.11	0.00	**35.95**	64.05	0.00	0.00

Table 13 – Group 2: CO$_2$ inventory resulting from 50 years of injection plus 1950 years of migration.

	Well	R_1	R_2	R_3	$\sum R_i$	SP	FP	L
	$W_{2,1,13,1}$	5.75	35.41	10.29	**51.44**	13.97	33.31	1.28
	$W_{1,1,1,3}$	6.69	34.75	9.97	**51.41**	15.58	32.28	0.72
	$W_{5,1,23,1}$	15.86	32.39	1.13	**49.38**	46.95	3.67	0.00
	$W_{3,1,28,1}$	16.11	31.51	1.10	**48.72**	47.74	3.55	0.00
	$W_{4,1,8,3}$	16.63	28.94	1.18	**46.74**	49.45	3.81	0.00
	$W_{6,1,18,1}$	16.61	28.96	1.18	**46.75**	49.41	3.84	0.00
	$W_{9,1,20,2}$	16.73	28.54	1.17	**46.44**	49.77	3.79	0.00
	$W_{8,1,15,1}$	16.60	28.09	1.54	**46.24**	48.77	5.00	0.00
	$W_{7,1,10,6}$	21.21	13.67	0.00	**34.88**	65.12	0.00	0.00
legacy	NA2	16.78	26.96	1.66	**45.40**	49.24	5.36	0.00
	RJS19	17.88	21.08	1.57	**40.53**	54.38	5.09	0.00
	NA3D	18.85	16.33	0.00	**35.17**	52.99	0.00	11.84
	NA1A	21.19	12.93	0.00	**34.12**	65.88	0.00	0.00

Table 14 – Group 2: CO$_2$ inventory resulting from 100 years of injection plus 1900 years of migration.

	Well	R_1	R_2	R_3	$\sum R_i$	SP	FP	L
	$W_{5,1,23,1}$	16.85	27.94	1.17	**45.96**	50.23	3.80	0.00
	$W_{3,1,28,1}$	16.96	27.44	1.18	**45.59**	50.58	3.84	0.00
	$W_{1,1,1,3}$	6.66	26.67	11.42	**44.75**	15.19	36.99	3.07
	$W_{6,1,18,1}$	17.27	25.87	1.24	**44.38**	51.61	4.01	0.00
	$W_{4,1,8,3}$	17.28	25.84	1.23	**44.36**	51.65	4.00	0.00
	$W_{2,1,13,1}$	5.13	27.03	12.13	**44.29**	12.24	39.27	4.20
	$W_{9,1,20,2}$	17.36	25.52	1.23	**44.12**	51.90	3.98	0.00
	$W_{8,1,15,1}$	17.73	22.54	1.54	**41.81**	53.21	4.98	0.00
	$W_{7,1,10,6}$	21.59	10.45	0.00	**32.04**	67.96	0.00	0.00
legacy	NA2	18.04	20.99	1.70	**40.72**	53.78	5.49	0.00
	RJS19	18.41	18.29	1.60	**38.30**	56.51	5.19	0.00
	NA3D	20.62	11.47	0.00	**32.09**	62.21	0.00	5.70
	NA1A	21.57	9.62	0.00	**31.19**	68.81	0.00	0.00

Table 15 – Group 3: CO$_2$ inventory resulting from 15 years of injection plus 1985 years of migration.

Well	R_1	R_2	R_3	$\sum R_i$	SP	FP	L
$W_{2,4,93,1}$	14.14	40.19	0.99	**55.32**	41.46	3.22	0.00
$W_{1,1,1,6}$	9.95	43.38	0.91	**54.23**	27.47	2.94	15.37
$W_{9,1,16,1}$	15.70	36.36	0.62	**52.67**	45.34	1.99	0.00
$W_{8,1,6,2}$	15.34	34.58	1.13	**51.06**	45.27	3.67	0.00
$W_{3,1,3,1}$	14.92	35.40	0.00	**50.32**	43.75	0.00	5.93
$W_{6,1,15,4}$	20.55	18.25	0.00	**38.80**	61.20	0.01	0.00
$W_{7,1,9,7}$	0.55	17.45	16.50	**34.50**	1.76	53.44	10.29
$W_{4,1,3,3}$	11.68	22.12	0.00	**33.80**	25.95	0.00	40.25
$W_{5,1,12,1}$	0.55	23.07	7.98	**31.59**	1.72	25.83	40.86
legacy { NA2	15.02	34.10	1.63	**50.76**	43.96	5.28	0.00
RJS19	17.25	23.82	1.56	**42.63**	52.31	5.06	0.00
NA3D	16.22	21.89	0.00	**38.11**	42.30	0.00	19.59
NA1A	20.42	17.62	0.00	**38.04**	61.96	0.00	0.00

Table 16 – Group 3: CO$_2$ inventory resulting from 30 years of injection plus 1970 years of migration.

Well	R_1	R_2	R_3	$\sum R_i$	SP	FP	L
$W_{1,1,1,6}$	12.75	39.54	1.11	**53.40**	35.98	3.59	7.03
$W_{2,4,93,1}$	15.24	35.28	1.08	**51.59**	44.92	3.48	0.00
$W_{3,1,3,1}$	16.96	32.41	0.00	**49.37**	50.31	0.00	0.32
$W_{8,1,6,2}$	15.98	31.79	1.15	**48.92**	47.35	3.73	0.00
$W_{9,1,16,1}$	16.83	30.72	0.81	**48.35**	49.04	2.61	0.00
$W_{4,1,3,3}$	14.82	22.89	0.00	**37.71**	37.24	0.00	25.05
$W_{6,1,15,4}$	20.93	15.74	0.00	**36.67**	63.33	0.00	0.00
$W_{5,1,12,1}$	0.55	22.32	9.34	**32.21**	1.76	30.25	35.78
$W_{7,1,9,7}$	0.54	14.58	16.40	**31.53**	1.76	53.12	13.60
legacy { NA2	15.94	30.39	1.64	**47.97**	46.71	5.32	0.00
RJS19	17.57	22.37	1.57	**41.51**	53.41	5.08	0.00
NA3D	17.51	19.15	0.00	**36.66**	47.30	0.00	16.04
NA1A	20.84	15.11	0.00	**35.95**	64.05	0.00	0.00

Table 17 – Group 3: CO$_2$ inventory resulting from 50 years of injection plus 1950 years of migration.

Well	R_1	R_2	R_3	$\sum R_i$	SP	FP	L
$W_{1,1,1,6}$	14.75	34.47	1.20	**50.43**	42.41	3.90	3.27
$W_{2,4,93,1}$	15.96	32.09	1.11	**49.15**	47.25	3.59	0.00
$W_{8,1,6,2}$	16.48	29.57	1.17	**47.23**	48.99	3.79	0.00
$W_{3,1,3,1}$	18.10	27.80	0.00	**45.90**	54.09	0.00	0.00
$W_{9,1,16,1}$	17.57	27.02	0.90	**45.50**	51.57	2.93	0.00
$W_{4,1,3,3}$	17.51	21.15	0.00	**38.66**	48.15	0.00	13.19
$W_{6,1,15,4}$	21.21	13.67	0.00	**34.88**	65.12	0.00	0.00
$W_{5,1,12,1}$	0.55	21.50	11.02	**33.06**	1.77	35.67	29.50
$W_{7,1,9,7}$	0.54	12.87	15.02	**28.44**	1.76	48.64	21.16
legacy { NA2	16.78	26.96	1.66	**45.40**	49.24	5.36	0.00
RJS19	17.88	21.08	1.57	**40.53**	54.38	5.09	0.00
NA3D	18.85	16.33	0.00	**35.17**	52.99	0.00	11.84
NA1A	21.19	12.93	0.00	**34.12**	65.88	0.00	0.00

Table 18 – Group 3: CO$_2$ inventory resulting from 100 years of injection plus 1900 years of migration.

Well	R_1	R_2	R_3	$\sum R_i$	SP	FP	L
$W_{2,4,93,1}$	16.88	27.82	1.18	**45.87**	50.32	3.81	0.00
$W_{8,1,6,2}$	17.20	26.24	1.22	**44.66**	51.38	3.96	0.00
$W_{1,1,1,6}$	17.32	25.67	1.13	**44.12**	51.16	3.65	1.08
$W_{9,1,16,1}$	18.50	22.39	0.99	**41.88**	54.91	3.21	0.00
$W_{3,1,3,1}$	19.53	20.86	0.00	**40.39**	59.61	0.00	0.00
$W_{4,1,3,3}$	20.16	15.19	0.00	**35.35**	60.82	0.00	3.82
$W_{5,1,12,1}$	0.54	19.72	12.93	**33.19**	1.76	41.86	23.18
$W_{6,1,15,4}$	21.59	10.45	0.00	**32.04**	67.96	0.00	0.00
$W_{7,1,9,7}$	0.54	11.13	11.14	**22.82**	1.76	36.08	39.35
legacy { NA2	18.04	20.99	1.70	**40.72**	53.78	5.49	0.00
RJS19	18.41	18.29	1.60	**38.30**	56.51	5.19	0.00
NA3D	20.62	11.47	0.00	**32.09**	62.21	0.00	5.70
NA1A	21.57	9.62	0.00	**31.19**	68.81	0.00	0.00

Results presented in the Tables 7-18 showed a great influence directly proportional to the number of nodes connected in the functional equipped with β-functions in relation to the percentage gain in residual storage. NA1A, NA2, NA3D e RJS19 are legacy wells from UNISIM-I-D.
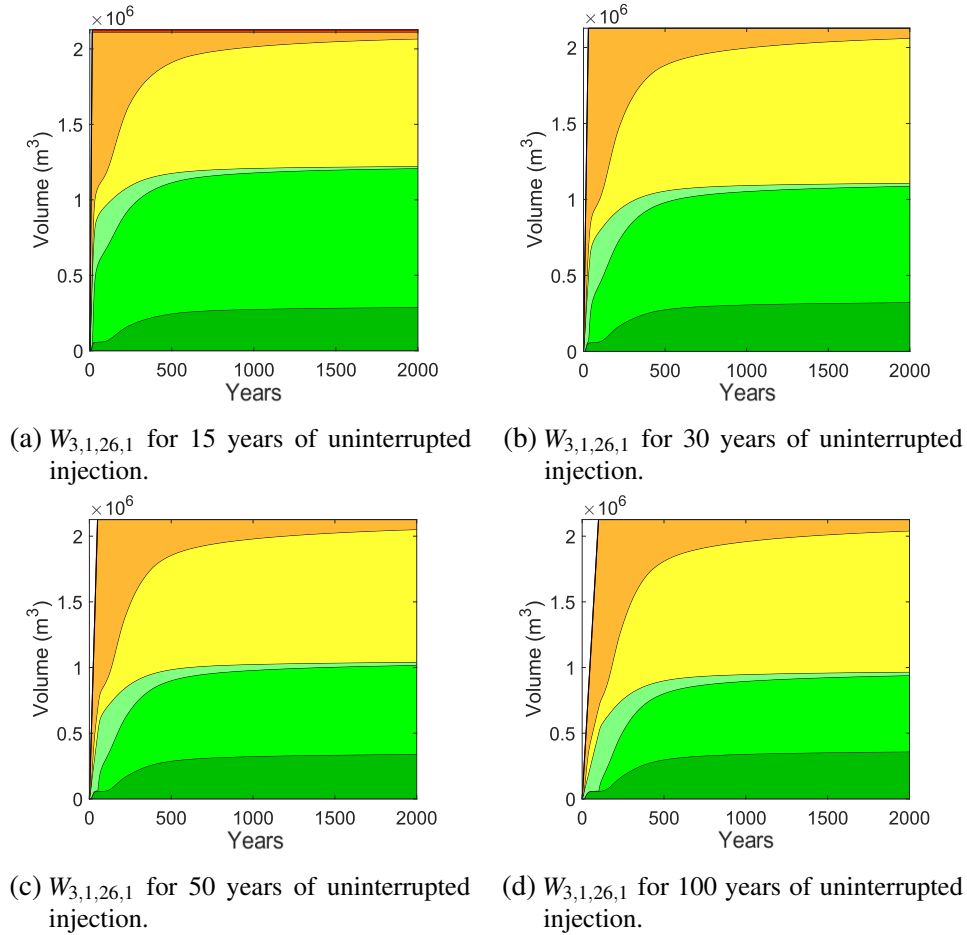

(a) $W_{3,1,26,1}$ for 15 years of uninterrupted injection.

(b) $W_{3,1,26,1}$ for 30 years of uninterrupted injection.

(c) $W_{3,1,26,1}$ for 50 years of uninterrupted injection.

(d) $W_{3,1,26,1}$ for 100 years of uninterrupted injection.

Figure 21 – CO_2 volume injected over time and storage dynamics for all four injection periods tested. The colors appearing in the plots correspond to volume proportions for each inventory state in the exact same way as described in Table 6. The time frame considers: (a) 1985 years of migration; (b) 1970 years of migration; (c) 1950 years of migration; and (d) 1900 years of migration.

The dynamics of the inventory states can be viewed through a time vs. injected volume plot in which the colored areas represent proportions of the total volume of CO_2 injected into a specific storage site (Fig. 21). All cases simulated have a similar dynamics (Fig. 22) due to the shareable numerical setup (Table 5). Initially, a fast and steep change in mass emerges as a response to the continuous injection process that lasts for 15, 30, 50 or 100 years. Next, during the post-injection stage, one observes asymptotic behaviors representing slow CO_2 migration inside the formation, or outsets of plateaus in the early post-injection period for residual storage and leakage that extend towards the late post-injection period over around 2000 years since the beginning of injection (Fig. 21). Furthermore, the amount of structural plume (SP) and free plume (FP) is greater in cases not suggested by the functional ones (Fig. 28), that is, greater
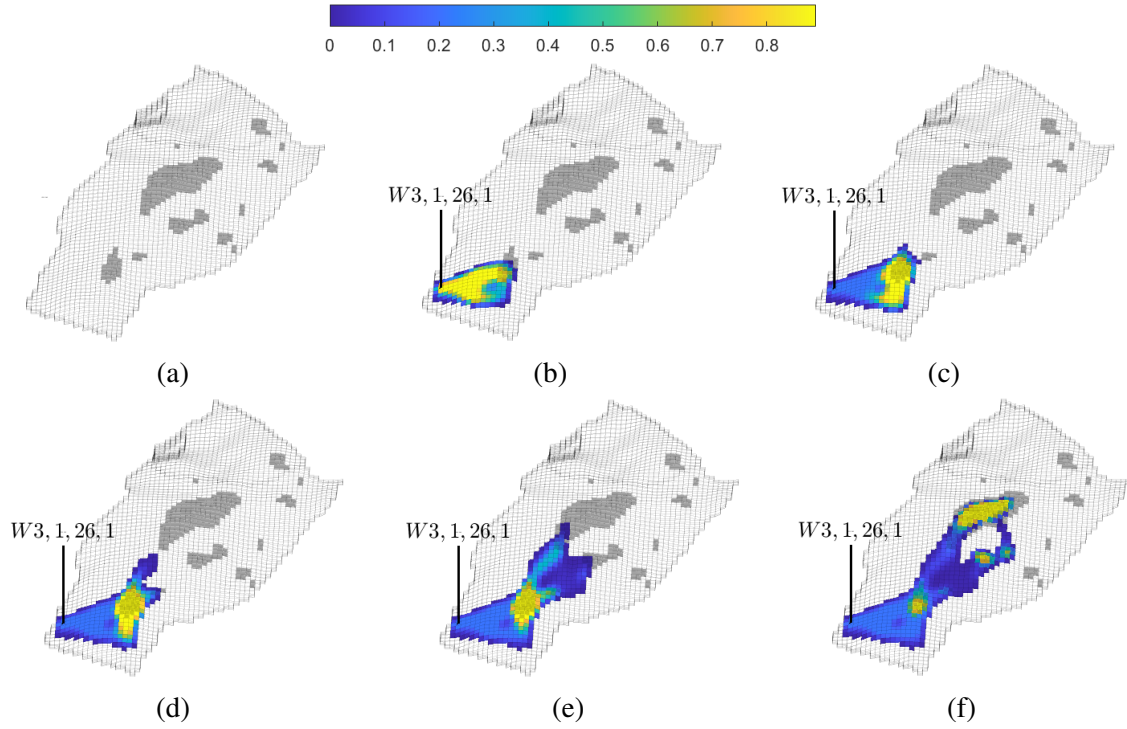
Figure 22 – Overlay of the CO$_2$ migrating gas plume (colored cells) and identified traps (dark gray regions) for the case described in Table 7: (a) portrays the initial condition; (b) the CO$_2$ saturation exactly at 15 years after injection; (c) to (f) portray the post-injection time. As seen, the gas flows mostly into the largest trap characterized.
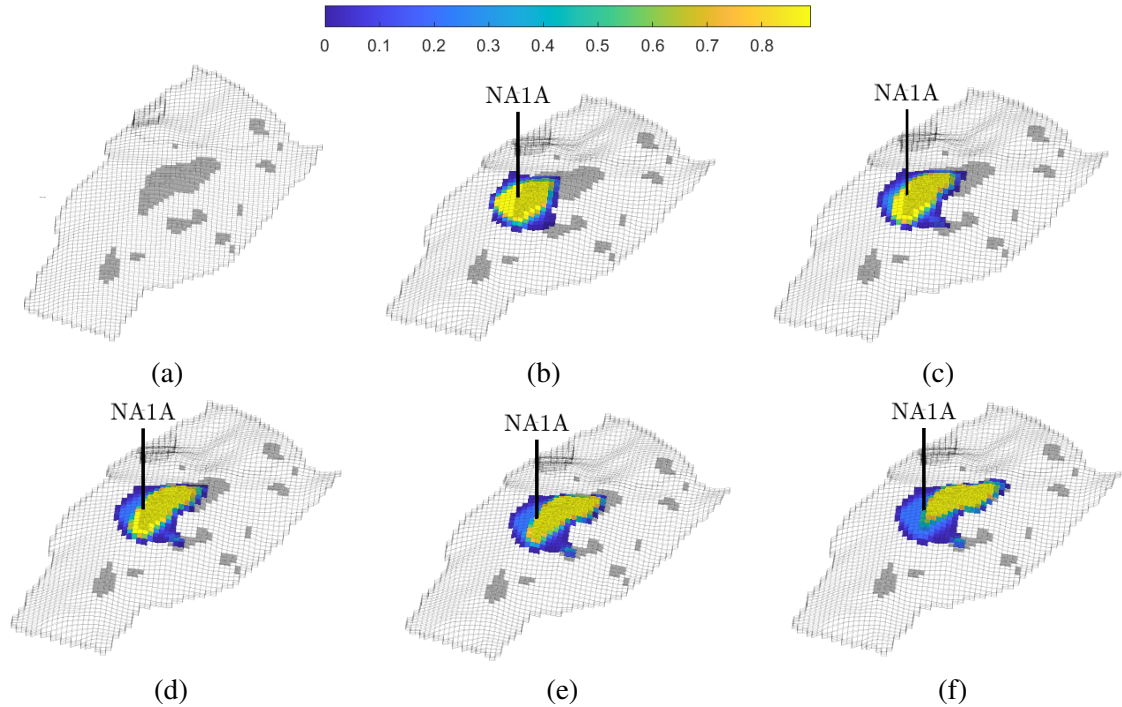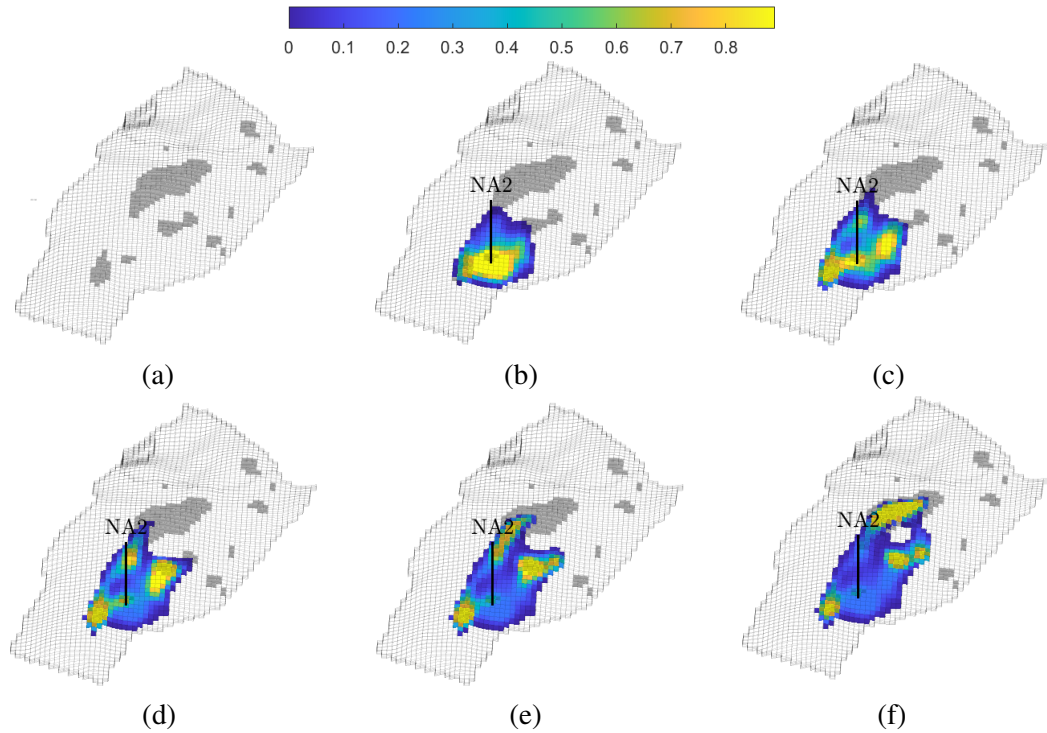

Figure 23 – Overlay of the CO$_2$ migrating gas plume (colored cells) and identified traps (dark gray regions) for the NA1A well case: (a) portrays the initial condition; (b) the CO$_2$ saturation exactly at 15 years after injection; (c) to (f) portray the post-injection time. As seen, the gas flows mostly into the largest trap characterized.
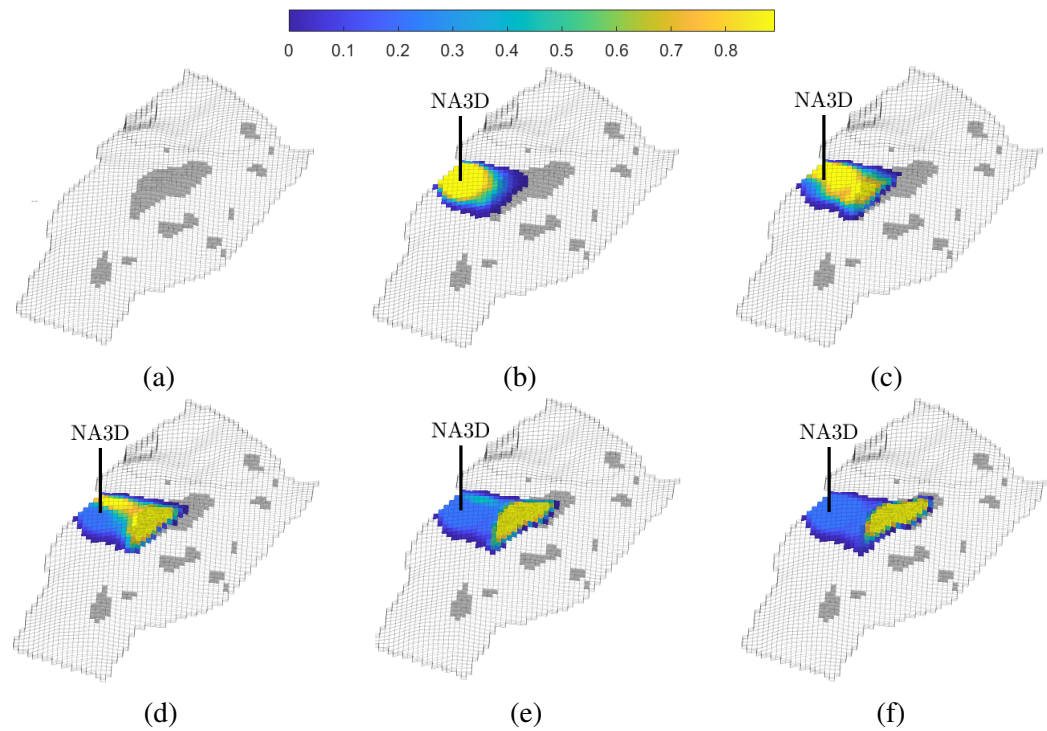
Figure 24 – Overlay of the CO_2 migrating gas plume (colored cells) and identified traps (dark gray regions) for the NA2 well case: (a) portrays the initial condition; (b) the CO_2 saturation exactly at 15 years after injection; (c) to (f) portray the post-injection time. As seen, the gas flows mostly into the largest trap characterized.

Figure 25 – Overlay of the CO_2 migrating gas plume (colored cells) and identified traps (dark gray regions) for the NA3D well case: (a) portrays the initial condition; (b) the CO_2 saturation exactly at 15 years after injection; (c) to (f) portray the post-injection time. As seen, the gas flows mostly into the largest trap characterized.
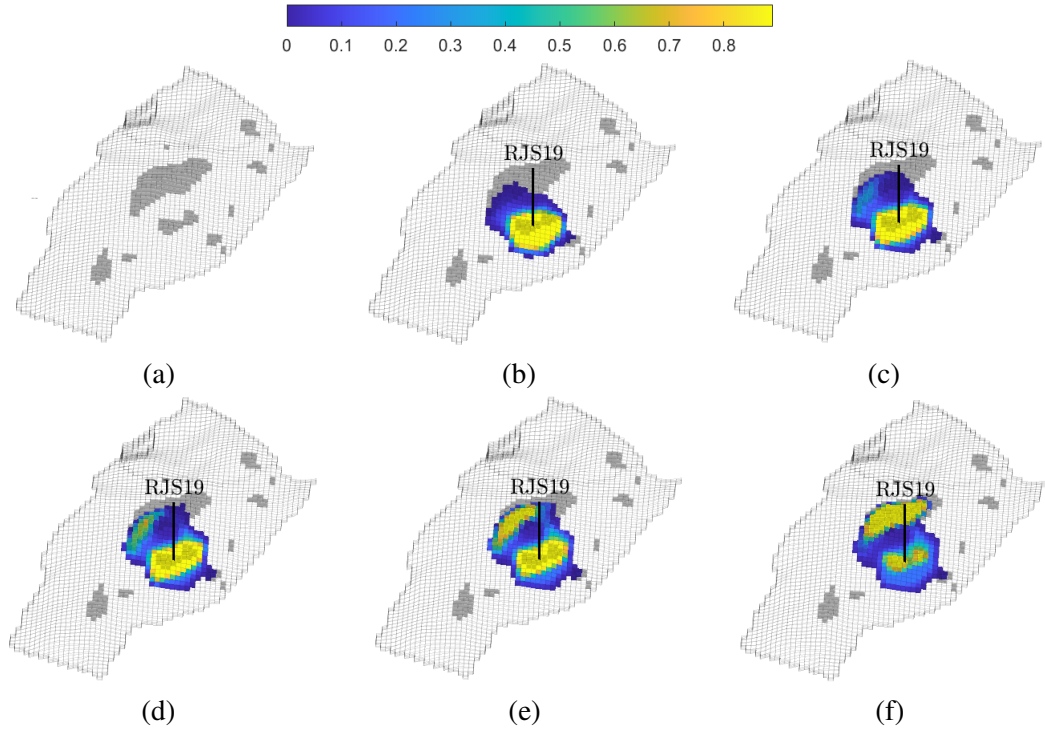
Figure 26 – Overlay of the CO_2 migrating gas plume (colored cells) and identified traps (dark gray regions) for the RJS19 well case: (a) portrays the initial condition; (b) the CO_2 saturation exactly at 15 years after injection; (c) to (f) portray the post-injection time. As seen, the gas flows mostly into the largest trap characterized.
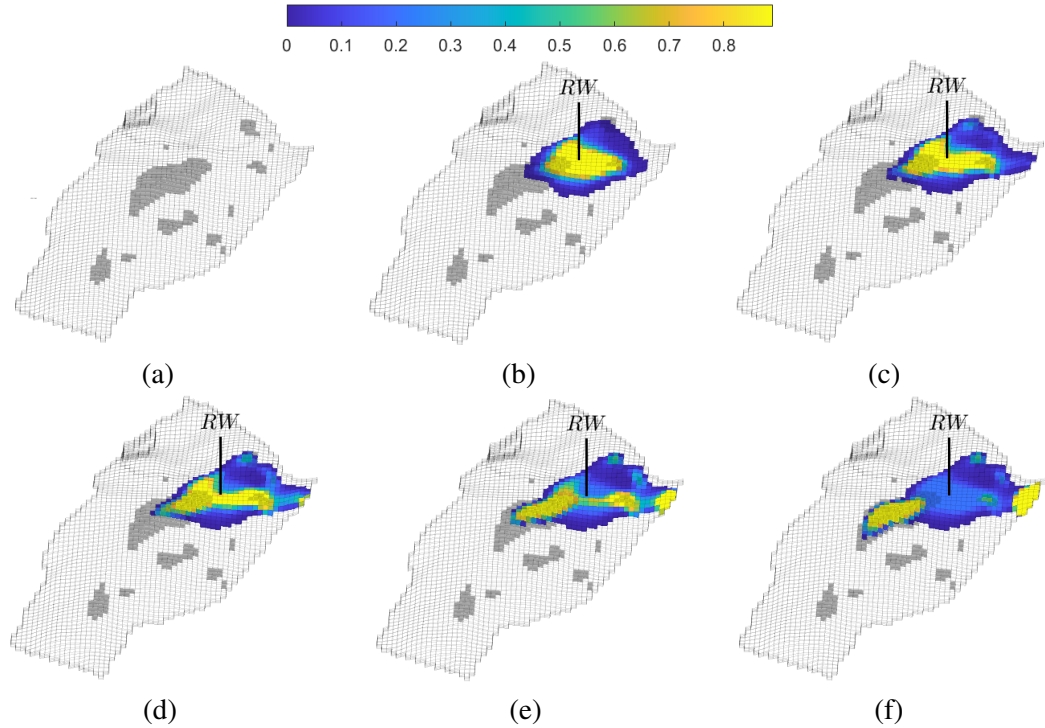

Figure 27 – Overlay of the CO_2 migrating gas plume (colored cells) and identified traps (dark gray regions) for the random well (*RW*) case: (a) portrays the initial condition; (b) the CO_2 saturation exactly at 15 years after injection; (c) to (f) portray the post-injection time. As seen, the gas flows mostly into the largest trap characterized.
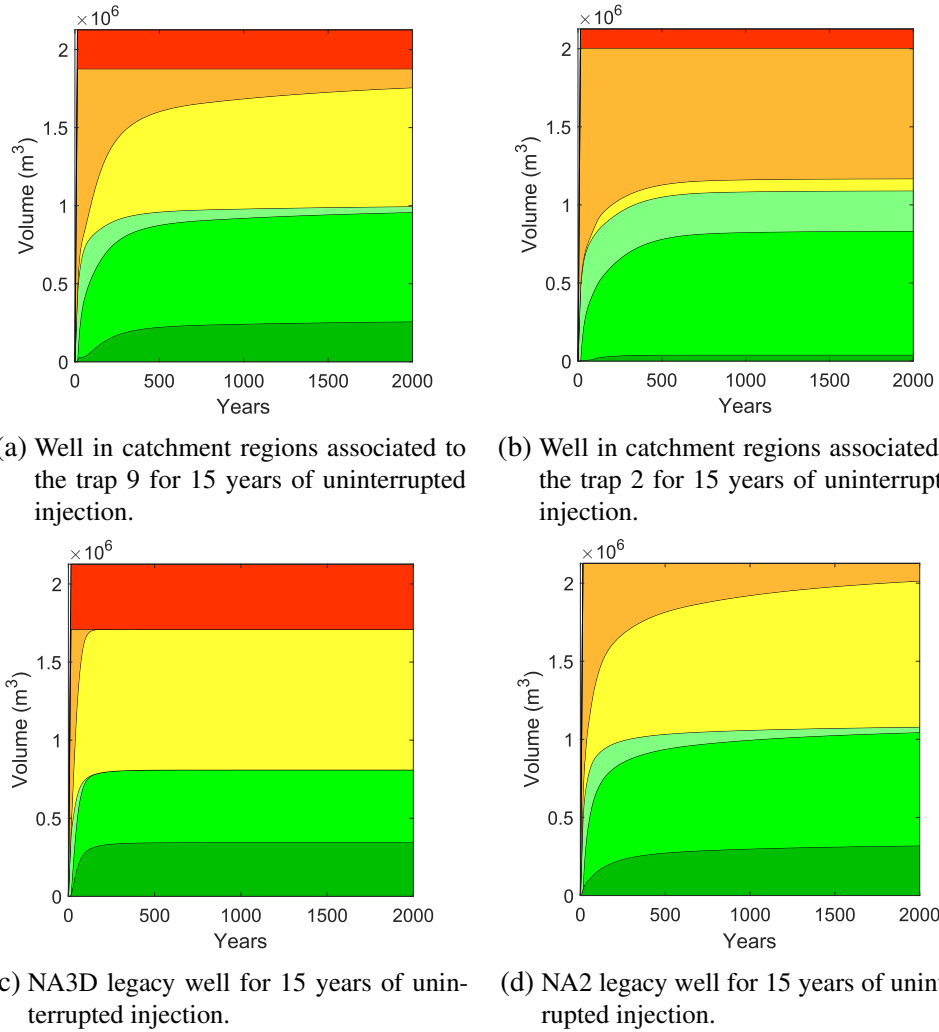
quantity in non-residual states.

(a) Well in catchment regions associated to the trap 9 for 15 years of uninterrupted injection.

(b) Well in catchment regions associated to the trap 2 for 15 years of uninterrupted injection.

(c) NA3D legacy well for 15 years of uninterrupted injection.

(d) NA2 legacy well for 15 years of uninterrupted injection.

Figure 28 – CO_2 volume injected over time and storage dynamics for an injection periods tested. The colors appearing in the plots correspond to volume proportions for each inventory state in the exact same way as described in Table 6. The time frame considers 1985 years of migration.

4.3.2 Benchmarking

An efficient way to highlight the injection performance of the potential storage sites is comparing visually the residual gas proportions reached after the simulations. To this end, two analyses are presented: the *physical benchmark* and the *analytic benchmark*, which are specific charts derived from the bar chart (Figs. 29 - 32) relative to the best CO_2 injection performances collected before (Tables 7 - 10).

The physical benchmarks (Figs. 29b, 30b, 31b, and 32b) rely on the legacy well infrastructure existing in the Namorado field model when assuming that it is already located in potential storage sites immediately exploitable for abatement interests. There are four legacy wells for scrutiny (NA2, RJS19, NA3D, and NA1A) whose maximum residual storages achieved after simulations were 50.76%, 47.97%, 45.40%, and 40.72% at the well NA2 for 15, 30, 50, and

100 years of injection, respectively (Tables 7-10). These upper bounds dominated over the other legacy well residual sum and are annotated as a dashed line in dark grey on the right (Fig. 29a, 30a, 31a, 32a). In contrast, all the best-simulated storage performances obtained by wells perforated according to the proposed functionals reached higher storage. For instance, for 15 years of injection, the well $W_{3,1,26,1}$, related to the storage site $S_{3,1,26,1}$, reached 57.67%, whereas the well $W_{1,1,1,8}$, related to the storage site $S_{1,1,1,8}$, reached 52.23% (Table 7). In terms of relative gain, the storage surplus delivered by the storage sites proposed by the qualifying functions varied from around 12% when compared to the legacy well NA2 to around 43% when compared to the legacy well NA1A and NA3D (Fig. 29b).

In Figure 29a, proportion chart for the best-performance wells (cf. Table 7) identified by the volumetric quality map approach (analytical benchmark) and those placed at the legacy sites (physical benchmark). From left to right, $W_{3,1,26,1}$ is the well that reached the best mark for residual storage (around 57.67%); $W_{5,1,24,1}$ the worst among the analytical functionals (around 53.87%); NA2 is the best-performance legacy well (around 50.76%); and NA1A is the legacy well with the worst performance (around 38.04%), besides considerable leakage. In Figure 29b, lollipop chart displaying the relative gain in CO_2 storage (surplus) of the wells placed at the sites qualified by the functionals compared to the legacy wells. For instance, the chart underscores that the well $W_{6,3,12,1}$ obtained a residual storage about 40% higher than NA1A, whereas the well $W_{9,1,17,1}$ led to 25% more residual storage when compared to the well RJS19. In Figure 29c likewise, this lollipop chart shows the relative surplus comparing the best wells provided by the novel functional formulae and the well derived by the $\mathcal{J}_1$ functional benchmark. One sees that the gain is positive in all cases, but milder than the results achieved for the legacy wells. Globally, one verifies that the functional approach improved the CO_2 containment rates.

Complementarily, the analytical benchmarks (Figs. 29c, 30c, 31c, and 32c) take into account only the best-simulated injection performances obtained by the most fundamental functional, namely $\mathcal{J}_1$, at the well $W_{1,1,1,8}$ over the storage site $S_{1,1,1,8}$, as reference, and measures how the other theoretical functionals perform against it at their associated wells and storage sites. In order of appearance, one sees that the well $W_{3,1,26,1}$, corresponding to the storage site $S_{3,1,26,1}$ reached the best surplus among all other theoretical functionals by around 13%, 10%, 5.5%, and 4%, respectively, in the order of injection cases. Oppositely, the worst performance verified for the theoretical functionals were: $\mathcal{J}_5$, for the cases of 15- and 30-years injection, since the well $W_{5,1,24,1}$, placed over the storage site $S_{5,1,24,1}$, only improved the residual storage by around 3%; $\mathcal{J}_9$, for the case of 50-years injection, since the well $W_{9,1,17,1}$, placed over the storage site $S_{9,1,17,1}$, only improved the residual storage by around 2.2%; and $\mathcal{J}_8$, for the cases of 100-years injection, since the well $W_{8,1,6,1}$, placed over the storage site $S_{8,1,6,1}$, only improved the residual storage by around 1.63%.
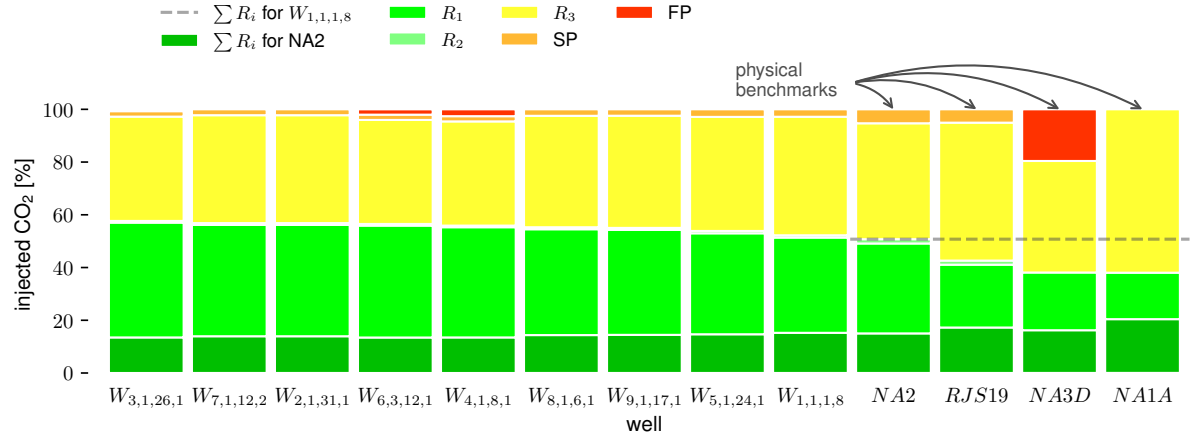
(a) CO_2 storage states per best-performance well for 15 years of injection. Green yellow/orange, and red colors stand for residual storage, flowing storage, and leakage, respectively.
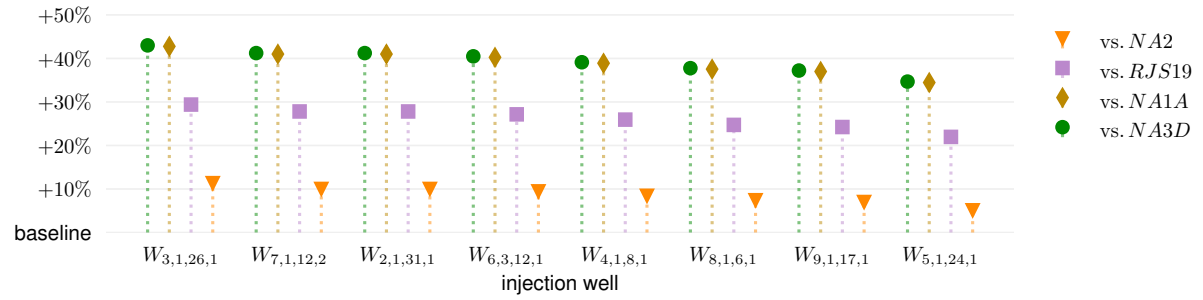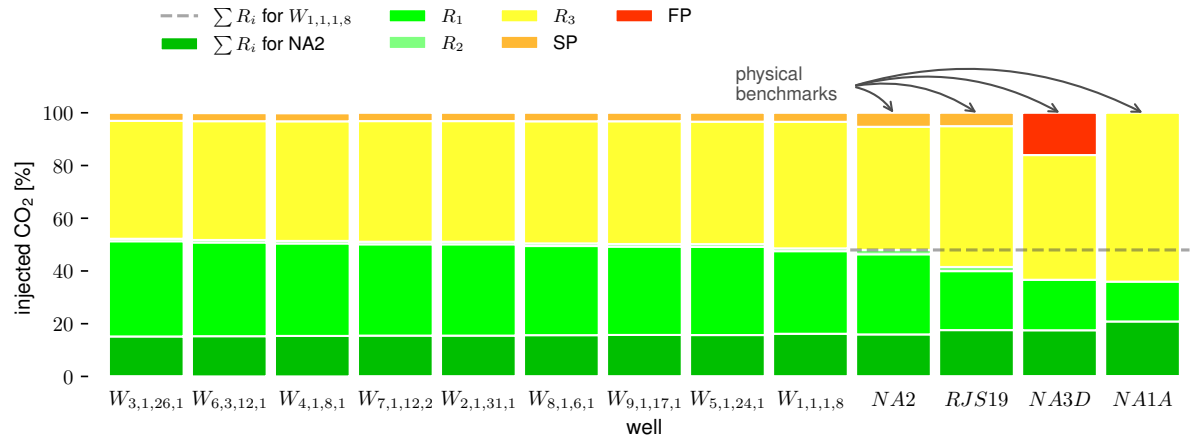

(b) Relative gain in CO_2 storage - physical benchmarks for 15 years of injection. The 4-stems groups represent the individual performances of the well $W_{j,d,b,q}$ compared to each one of the legacy wells.
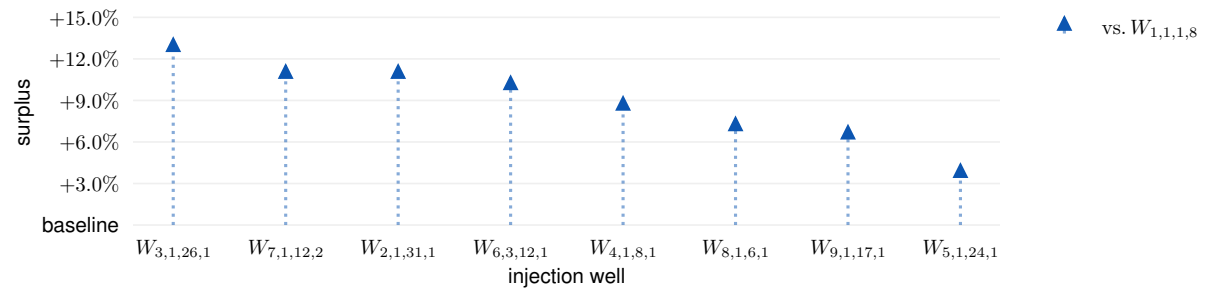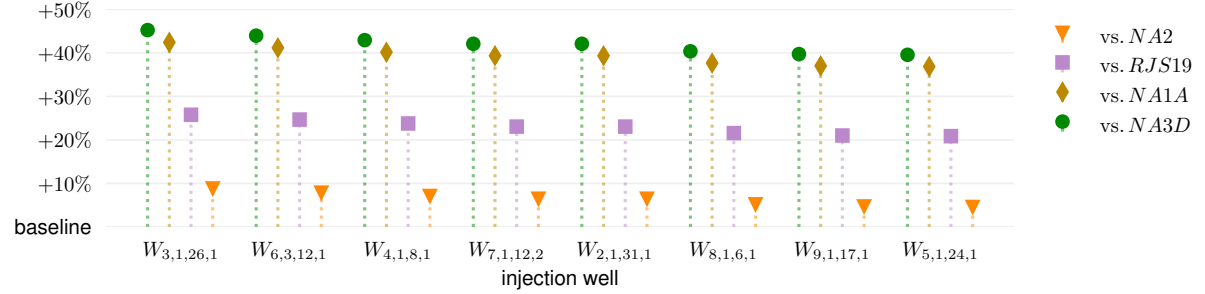

(c) Relative gain in CO_2 storage - analytic benchmarks for 15 years of injection. The stems represent the individual performances of wells $W_{j,d,b,q}$ compared to $W_{1,1,34,1}$, the best-performance well associated to the underlying functional $\mathcal{J}_1$.

Figure 29 – Comparative performance of CO_2 injection by largest group with nodes connected by functional (Group 1).

(a) CO_2 storage states per best-performance well for 30 years of injection. Green yellow/orange, and red colors stand for residual storage, flowing storage, and leakage, respectively.

(b) Relative gain in CO_2 storage - physical benchmarks for 30 years of injection. The 4-stems groups represent the individual performances of the well $W_{j,d,b,q}$ compared to each one of the legacy wells.

(c) Relative gain in CO_2 storage - analytical benchmarks for 30 years of injection. The stems represent the individual performances of wells $W_{j,d,b,q}$ compared to $W_{1,1,34,1}$, the best-performance well associated to the underlying functional $\mathcal{J}_1$.
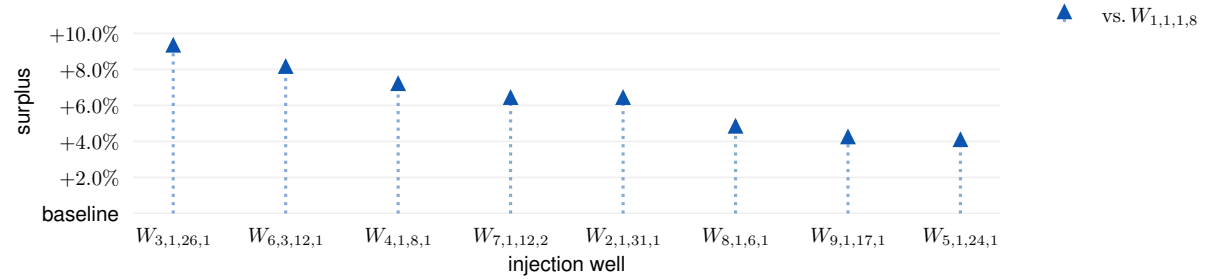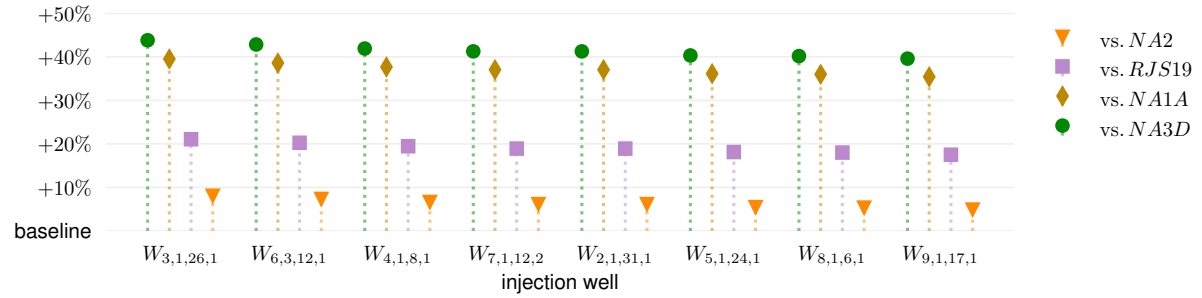
Figure 30 – Comparative performance of CO_2 injection for 30 years of injection by largest group with nodes connected by functional (Group 1) (cf. Table 8). Similar interpretation as that from Figure 29 applies here: (a) proportion chart for the best performance wells; (b) lollipop chart displaying the relative gain in CO_2 storage (surplus) of the wells placed at the sites qualified by the functionals compared to the legacy wells; (c) lollipop chart of the relative surplus comparing the best wells provided by the novel functional formulae and the well derived by the $\mathcal{J}_1$ functional benchmark. One sees that the gain is positive in all cases, but milder than the results achieved for the legacy wells. Globally, one verifies that the functional approach improved the CO_2 containment rates.

4.3.3 Pressure field

A few considerations on the pressure field can be useful to give an overview of the magnitudes treated here (order of 30 MPa). Since that the injection rate applied to the simulations
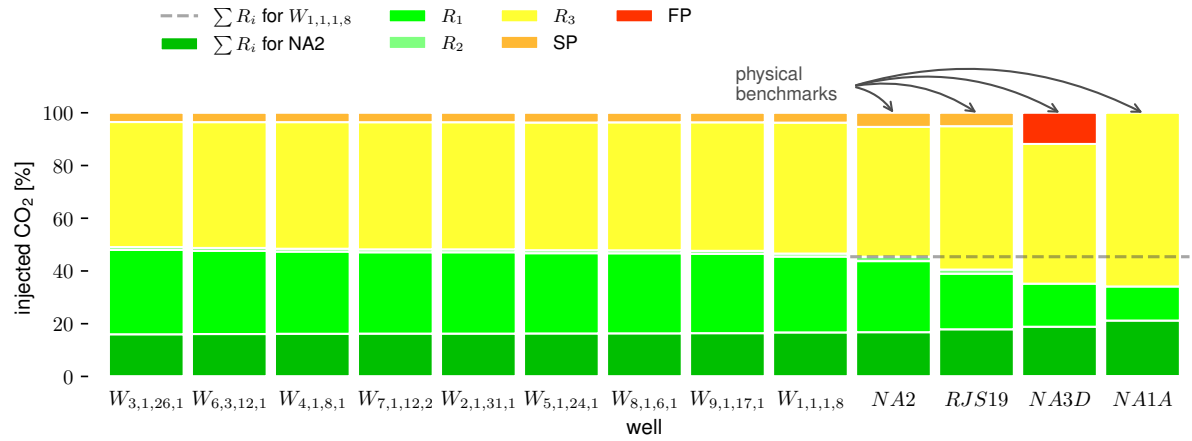
(a) CO₂ storage states per best-performance well for 50 years of injection. Green yellow/orange, and red colors stand for residual storage, flowing storage, and leakage, respectively.

(b) Relative gain in CO₂ storage - physical benchmarks for 50 years of injection. The 4-stems groups represent the individual performances of the well $W_{j,d,b,q}$ compared to each one of the legacy wells.
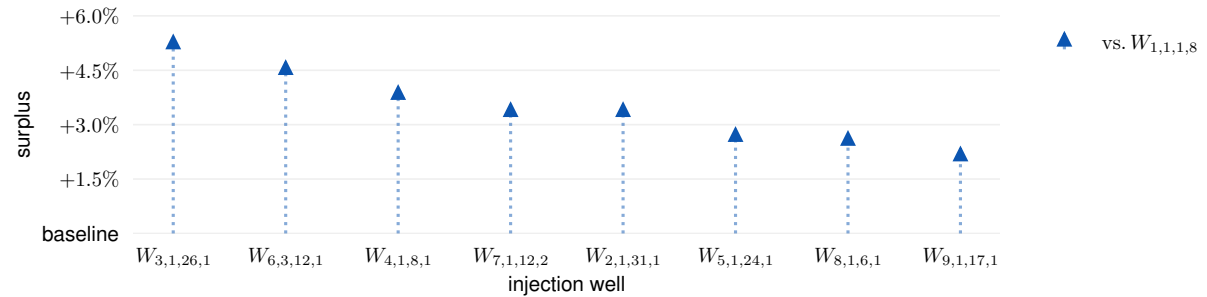
(c) Relative gain in CO₂ storage - analytical benchmarks for 50 years of injection. The stems represent the individual performances of wells $W_{j,d,b,q}$ compared to $W_{1,1,34,1}$, the best-performance well associated to the underlying functional $\mathcal{J}_1$.

Figure 31 – Comparative performance of CO₂ injection for 50 years of injection by largest group with nodes connected by functional (Group 1) (cf. Table 9). Similar interpretation as that from Figures 29 and 30 apply here: (a) proportion chart for the best performance wells; (b) lollipop chart displaying the relative gain in CO₂ storage (surplus) of the wells placed at the sites qualified by the functionals compared to the legacy wells; (c) lollipop chart of the relative surplus comparing the best wells provided by the novel functional formulae and the well derived by the $\mathcal{J}_1$ functional benchmark. One sees that the gain is positive in all cases, but milder than the results achieved for the legacy wells. Globally, one verifies that the functional approach improved the CO₂ containment rates.

were backed by literature data, the pressure field is expected to be limited within a marginally safe range.

(a) CO_2 storage states per best-performance well for 100 years of injection. Green yellow/orange, and red colors stand for residual storage, flowing storage, and leakage, respectively.
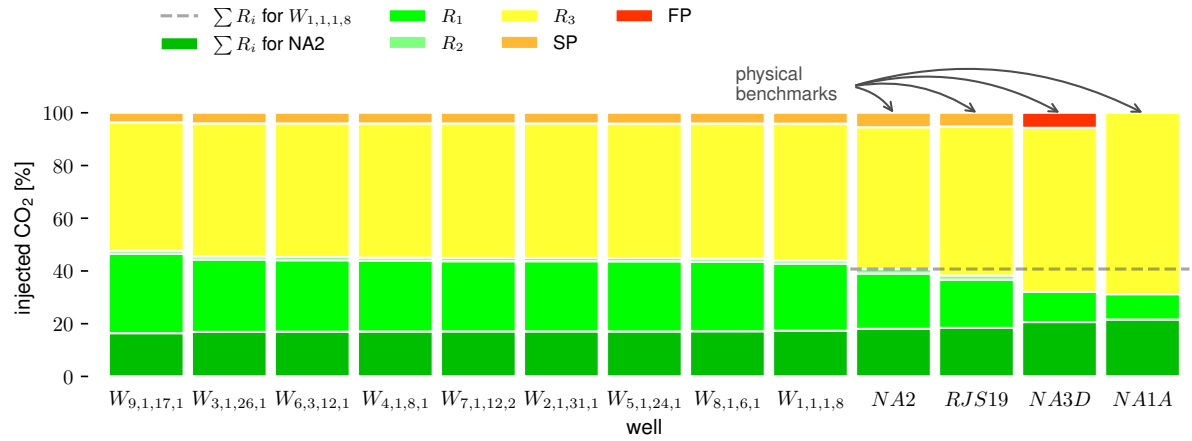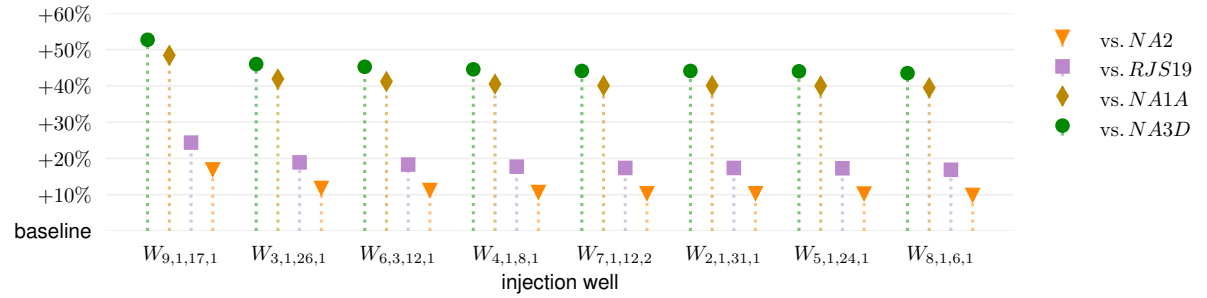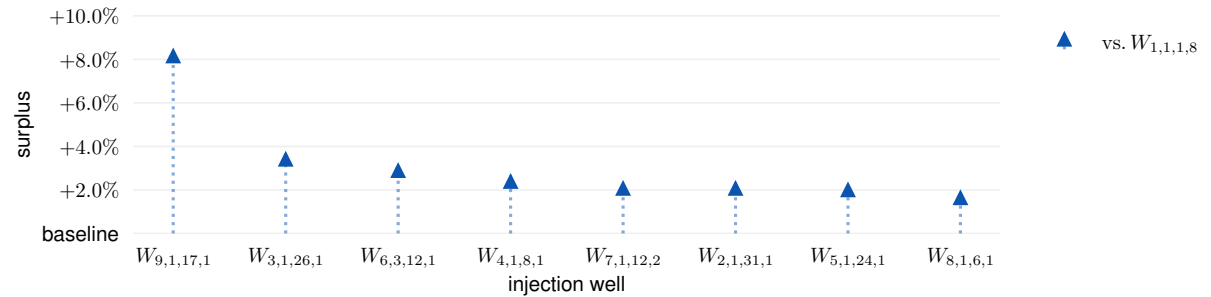

(b) Relative gain in CO_2 storage - physical benchmarks for 100 years of injection. The 4-stems groups represent the individual performances of the well $W_{j,d,b,q}$ compared to each one of the legacy wells.

(c) Relative gain in CO_2 storage - analytical benchmarks for 100 years of injection. The stems represent the individual performances of wells $W_{j,d,b,q}$ compared to $W_{1,1,34,1}$, the best-performance well associated to the underlying functional $\mathcal{J}_1$.

Figure 32 – Comparative performance of CO_2 injection for 100 years of injection by largest group with nodes connected by functional (Group 1) (cf. Table 10). Similar interpretation as that from Figures 29, 30, and 31 apply here: (a) proportion chart for the best performance wells; (b) lollipop chart displaying the relative gain in CO_2 storage (surplus) of the wells placed at the sites qualified by the functionals compared to the legacy wells; (c) lollipop chart of the relative surplus comparing the best wells provided by the novel functional formulae and the well derived by the $\mathcal{J}_1$ functional benchmark. One sees that the gain is positive in all cases, but milder than the results achieved for the legacy wells. Globally, one verifies that the functional approach improved the CO_2 containment rates.

Because of the VE model assumption, there is no considerable pressure variation and the simulator responses are similar for all cases. For completeness, we plotted 2D views of the

pressure field for the same case depicted in Figure 22 at 1 year and 15 years after injection (Figs. 33, 34, 35, 36 and 37). As seen, both images are consistent with expectancy and show quasi-static behaviors, so that it is irrelevant to analyze changes over time or along the third direction in depth.
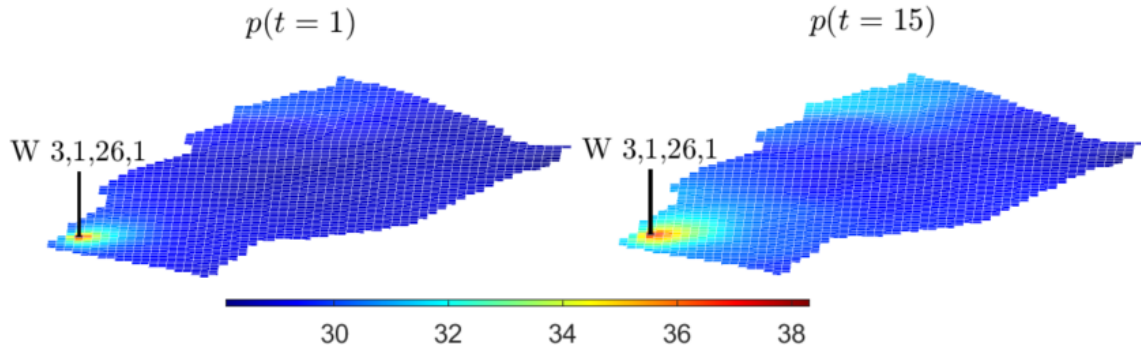

Figure 33 – 2D views of the pressure field for the case presented in Figure 22 at two fixed time instants: 1 year and 15 years after injection. Due to the VE formulation, the depth-wise variation is projected onto the grid top layer, so that high gradients are noticed only in the well neighborhood. The pressure is quantitatively measured in MPa and remains under equilibrium over time after the well opening (see Figure 38).

Figure 34 – 2D views of the pressure field for the NA1A well case at two fixed time instants: 1 year and 15 years after injection. Due to the VE formulation, the depth-wise variation is projected onto the grid top layer, so that high gradients are noticed only in the well neighborhood. The pressure is quantitatively measured in MPa and remains under equilibrium over time after the well opening (see Figure 40).

Plots over time of the local pressure field for cells randomly chosen in the model also show that it undergoes just a natural initial burst because of the well opening, but it stabilizes quite soon due to the vertical equilibrium (see Appendix B). The first plot concerns a cell inside the volume covered by the biggest trap; the second to a cell in the middle and the third to a cell near the lateral boundary of the reservoir (Fig. 38).

Figure 35 – 2D views of the pressure field for the NA2 well case at two fixed time instants: 1 year and 15 years after injection. Due to the VE formulation, the depth-wise variation is projected onto the grid top layer, so that high gradients are noticed only in the well neighborhood. The pressure is quantitatively measured in MPa and remains under equilibrium over time after the well opening (see Figure 40).
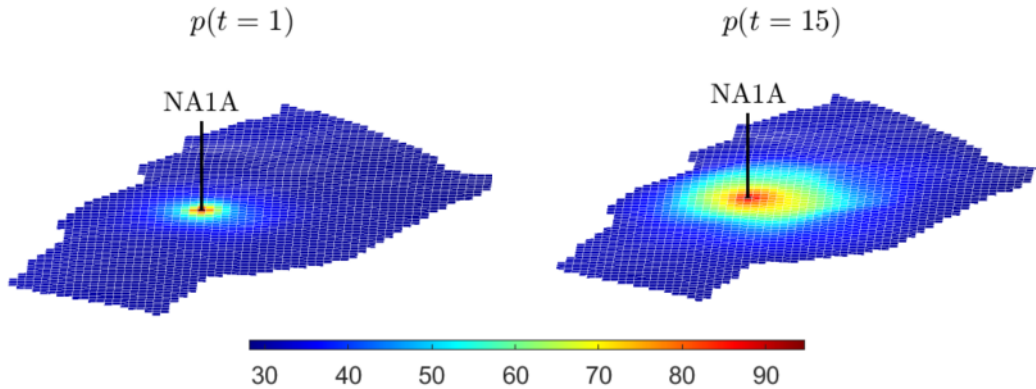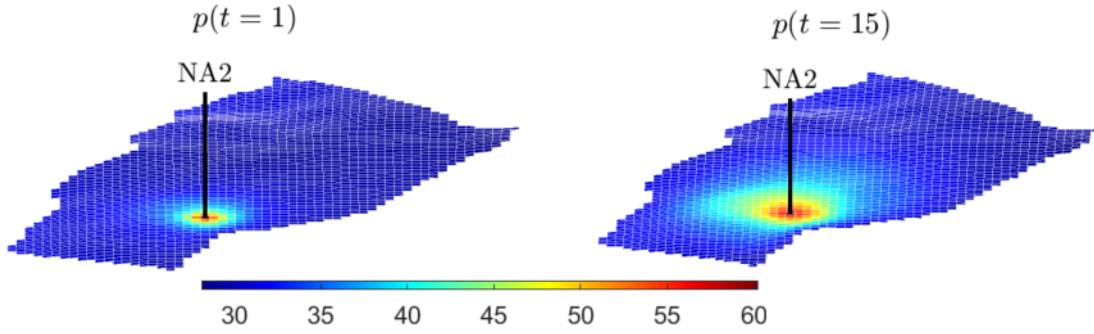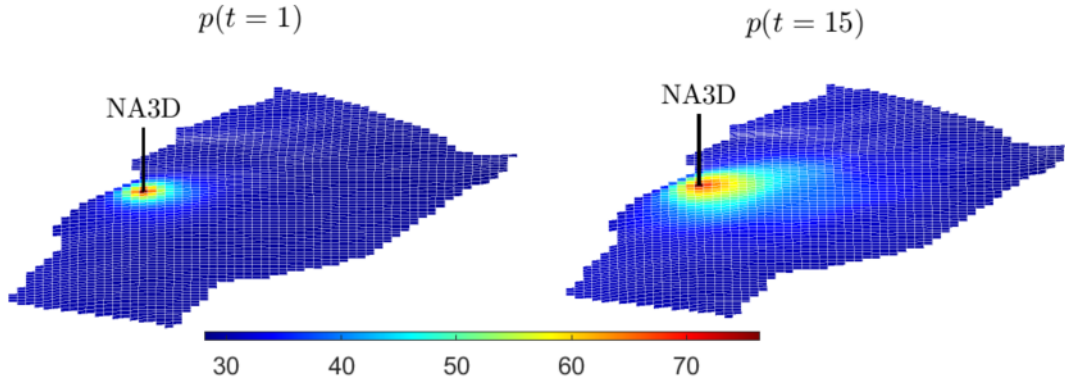

Figure 36 – 2D views of the pressure field for the NA3D well case at two fixed time instants: 1 year and 15 years after injection. Due to the VE formulation, the depth-wise variation is projected onto the grid top layer, so that high gradients are noticed only in the well neighborhood. The pressure is quantitatively measured in MPa and remains under equilibrium over time after the well opening (see Figure 40).
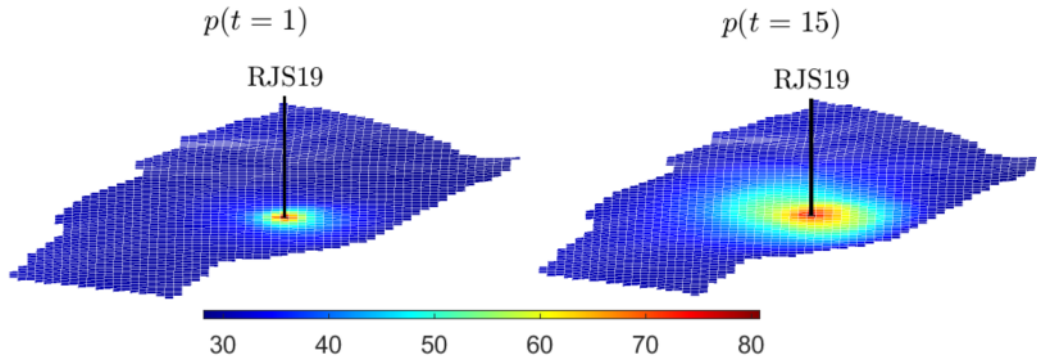
Figure 37 – 2D views of the pressure field for the RJS19 well case at two fixed time instants: 1 year and 15 years after injection. Due to the VE formulation, the depth-wise variation is projected onto the grid top layer, so that high gradients are noticed only in the well neighborhood. The pressure is quantitatively measured in MPa and remains under equilibrium over time after the well opening (see Figure 40).

4.4 Discussion

A few comments to clarify the results are drawn in this section and arranged in the form of topics. First, we underscore the positive aspects:

Figure 38 – Plots over time of the local pressure field for three cells sampled in different locations: inside the biggest trap (cell 1); in the central region of (cell 2); and at the lateral boundary (cell 3) of the model. As seen, the pressure remains stable almost over all the simulation time, by following the VE formulation assumptions. The initial perturbations reflect the instantaneous well opening.

- *Functional choice and usability*. The family of functionals introduced here comprises different levels of complexity in terms of their constituent properties. In contrast to the analytical benchmark $\mathcal{J}_1$, their construction aggregates nonlinear effects that improve the site qualification. Out of nine best wells selected for comparison appearing in all cases of injection, seven wells had total residual storage varying from 55.03% to 57.67% for $t = 15$ (Table 7), 50.23% to 52.21% for $t = 30$ (Table 8), 47.63% to 49.07% for $t = 50$ (Table 9) and 44.76% to 45.54% for $t = 100$ (Table 10). The other two wells,

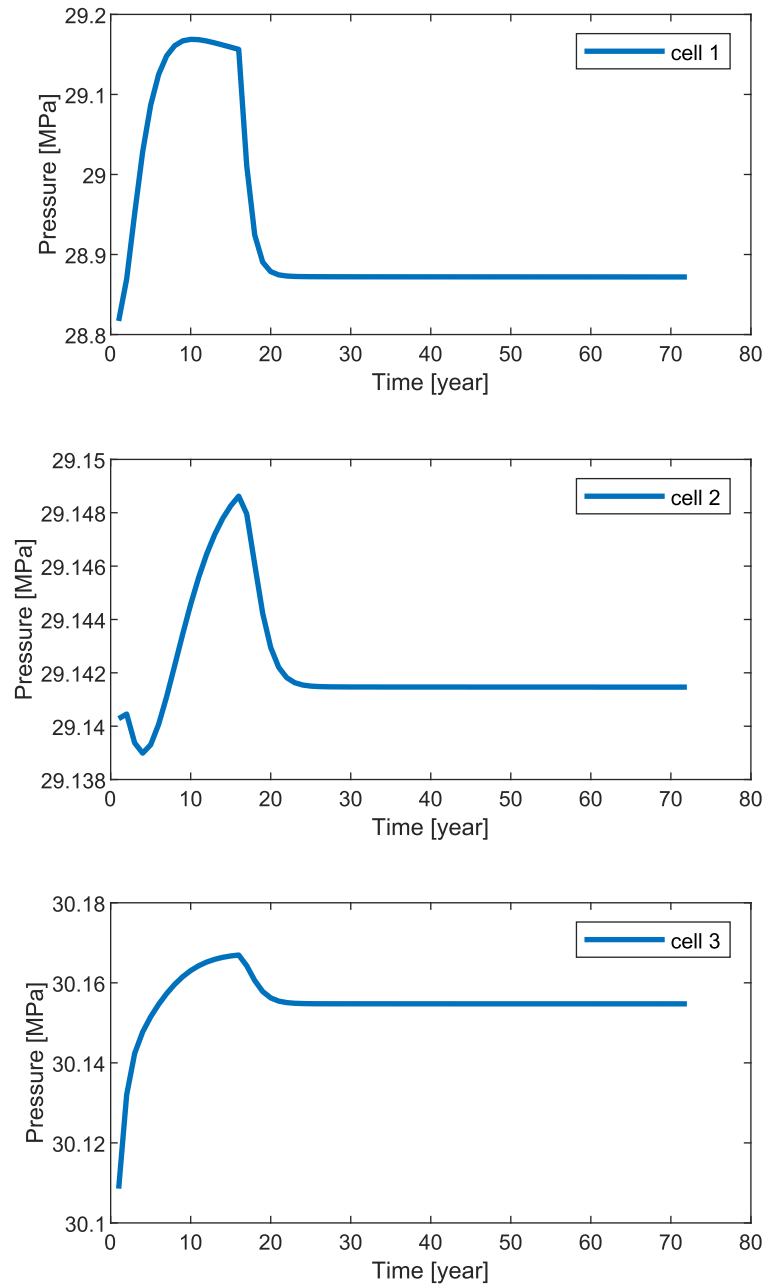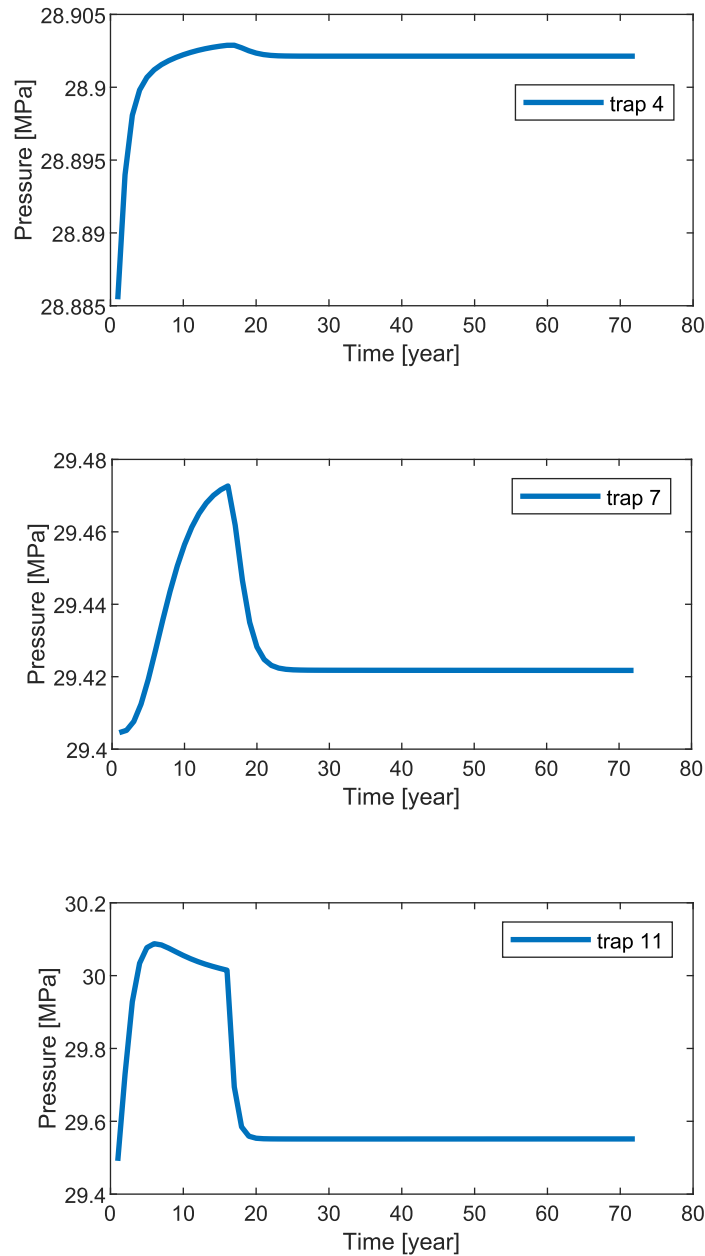Figure 39 – Plots over time of the local pressure field for three cells sampled in different locations: inside the trap 4; inside the trap 7; and inside the trap 11 of the model. As seen, the pressure remains stable almost over all the simulation time, as seen in the Figure 38, by following the VE formulation assumptions. The initial perturbations reflect the instantaneous well opening.

$W_{5,1,24,1}$ and $W_{1,1,1,8}$, had worse performances. A possible reason why that seven wells had superior performance is due to the inclusion of the distance-to-trap functions, which are absent in J_5 and J_1. While it is clear that the β functions had a positive effect upon the benchmark functional, the surpluses are below 2% due to modeling factors, such as fixed brine saturation and small variations of pressure. This modest gain is, however, an indication that the functionals improve the site qualification and have usability for the industry. Based on the current study case, it is not clear which functional must occupy the first rank because their performance is tightly competitive. However, it is undeniable that the incorporation of parameters related to the traps into the β-functions place functionals
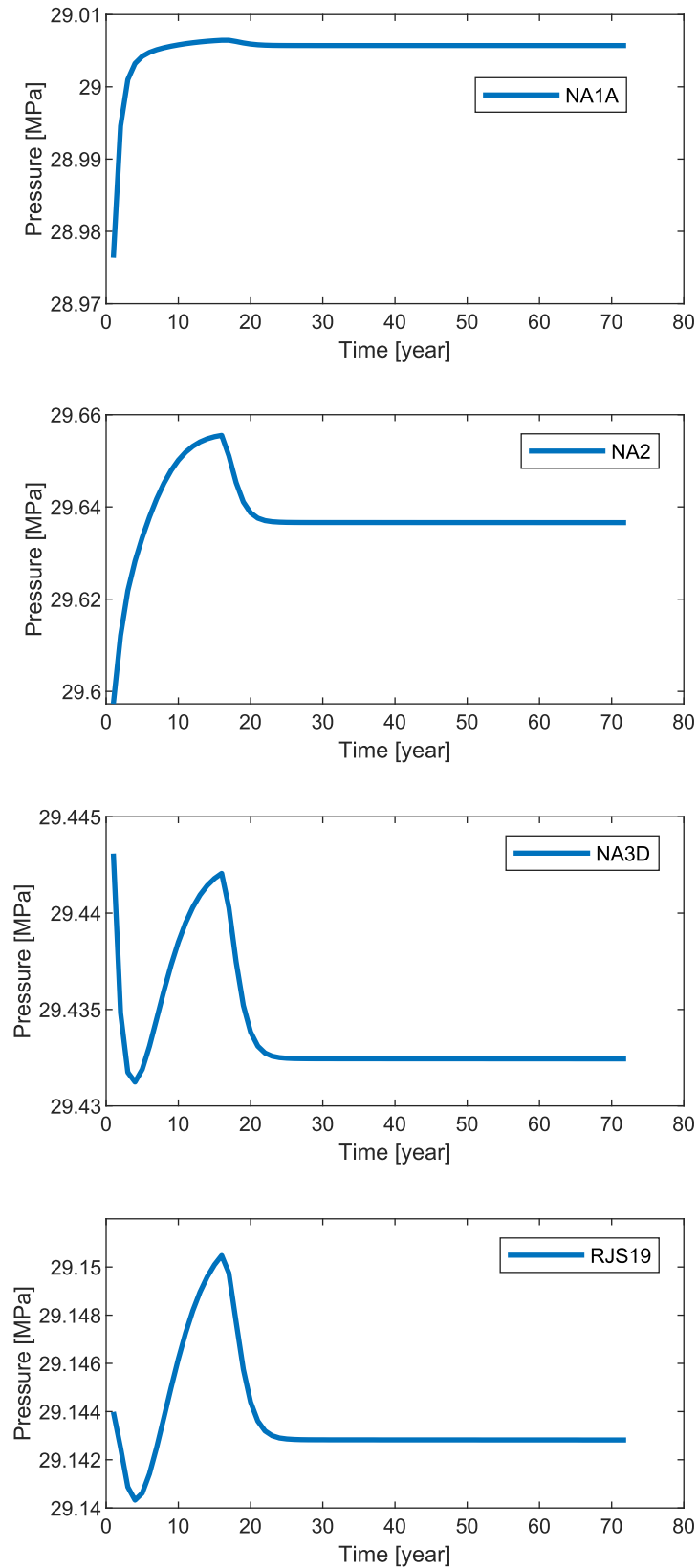
Figure 40 – Plots over time of the local pressure field for UNISIM-I-D wells: NA1A, NA2, NA3D and RJS19. As seen, the pressure remains stable almost over all the simulation time, as seen in the Figure 38 and Figure 39, by following the VE formulation assumptions. The initial perturbations reflect the instantaneous well opening.

like $\mathcal{J}_3$ and $\mathcal{J}_6$ at the top of the best performances.

- *Efficiency of the volumetric quality map approach*. The number of possible storage sites found through the VQM approach may vary from zero, like $V_{2,2}$, $V_{2,4}$, and $V_{5,4}$, to a few dozens, like $V_{7,1}$, $V_{4,2}$, and $V_{8,3}$, with 39, 24, and 50 sites, respectively (Table 4). This, in turn, is a consequence of the combined action of the binning methods and partitioning criterion. On one hand, each binning method has its own power to explain the statistical nuances of the field model; on the other hand, the clustering depends on a minimum number of grid cells fixed in 10, which correspond to a minimum storage site of $134\,550\,\mathrm{m}^3$ in pore volume. For the current study, the average relative ratio of harnessing per VQM was 13.6%. In absolute counting, this ratio reverts to 12.7%, since 1450 storage sites were found in total, but only 184 were taken for analysis. The Jaccard filtering is an important mechanism to avoid duplicata sites and excessive simulation, but replaceable with a different approach. If a minimum effort criterion was adopted, `sqrt` ($b = 4$) would be the most appropriate binning method to use. However, it would also be the poorest in explaining the regions. Working with a specific binning method is a matter of decision and depends on the balance between statistical explainability and computational effort. However, after the IUC/clustering implementation, it becomes clear which VQM performs better. Based on the resulting residual storages, only `scott` ($b = 1$) and `sturges` ($b = 3$) were efficient.

- *Performance in relation to legacy wells*. Under the assumption that the locations of the legacy wells existing in the model were previously determined by screening and selection, it is straightforward to think they reach potential storage sites. This way, the physical benchmarks delivered dramatic contrasts. One sees that the injection performance of the functionals overcame the marks of all legacy wells. In particular, the surplus for NA3D jumped to around 45% for $W_{3,1,26,1}$ (Fig. 29b), mainly because of the high leakage portion observed in the simulation (Fig. 29). Even so, the surplus for the other wells were quite better in all cases, with rates from 6% to 42%, thus demonstrating that the functionals have the ability to improve site selection through their qualification scores.

- *Trapping mechanisms*. The injection dynamics over time pointed out that a considerable portion of the CO_2 inventory was kept stored residually. The total volumetric capacity of structural traps computed for this study was 2.13×10^6 m^3, corresponding to 2% of the available bulk pore volume.

On the other hand, it is worthwhile mentioning a few drawbacks and limitations of this study:

- *Field coverage and gridding*. Due to numerical limitations to cope with the gas plume over noncontiguous layers of the grid, the model created for the current test reduced the

total coverage of the field to much less layers. As a consequence both from the VE formulation and the reduced reservoir thickness, the pressure field is almost unchanged. Moreover, the functionals soon reach a saturated state of structural residual storage (R_1), by featuring a strong dominance of buoyancy forces. This limitation affected the analytical tests.

- *Fully-dynamic functionals*. The current functionals deal with properties inherently dynamic, such as pressure and saturation, but they are maintained fixed at a time instant. In the future, we intend to incorporate a more extensive range of processes and properties that vary with time.

- *Generalization*. For the time being, the functionals were tested in a single reservoir model. Further study is required to assess the performance in other models for generalization.

5 CONCLUSION

This study presented a set of injectivity functionals that can be used to qualify CO_2 storage sites. These functionals are promising in supporting geologic carbon storage ventures, as they can improve injection performance for wells located in strategic positions.

Since there are many physical properties affecting gas dynamics in deep storage, this study handled them statically. However, time-varying quantities are necessary for a more realistic behavior.

For the Brazilian context, this research is useful in developing a comprehensive understanding of CO_2 injection processes. It is important to note that the comparisons showed a storage surplus increase of up to 50% when legacy and novels wells are compared, and 22% when novels and random wells are compared.

In relation to the use of reservoir process speed without the use of β-functions shows a storage increase of up to 66% when legacy and novels wells are compared. Results presented showed a great influence directly proportional to the number of nodes connected in the functional units equipped with β-functions in relation to the percentage gain in residual storage.

Storage efficiency is influenced by several geological and operational factors. Detailed future studies are needed to better understand these factors and optimize injection and monitoring techniques.

The thesis did not cover geomechanical couplings, which take into account dynamic variations of properties, and anisotropy analyses, which provide precise control over the gas plume. These subjects will be explored in future research.

BIBLIOGRAPHY

ABBASZADEH, M. *et al.* Permeability prediction by hydraulic flow units - theory and applications. **SPE Formation Evaluation**, Society of Petroleum Engineers (SPE), v. 11, n. 4, p. 263 – 271, 1996. ISSN 0885923X. Citation on page 45.

ABBASZADEH, M.; SHARIATIPOUR, S. M. Investigating the impact of reservoir properties and injection parameters on carbon dioxide dissolution in saline aquifers. **Fluids**, MDPI, v. 3, n. 4, p. 76, 2018. Citation on page 32.

ABUOV, Y.; SEISENBAYEV, N.; LEE, W. Co2 storage potential in sedimentary basins of kazakhstan. **International Journal of Greenhouse Gas Control**, Elsevier, v. 103, p. 103186, 2020. Citation on page 33.

AGENCY, I. E. **20 years of carbon capture and storage: Accelerating future deployment**. [S.l.]: International Energy Agency, 2016. Citation on page 25.

AHMADINIA, M.; SHARIATIPOUR, S. Investigating the impact of caprock morphology on co2 plume migration and trapping mechanisms using the mrst-co2lab and eclipse-blackoil codes. In: **14th Greenhouse Gas Control Technologies Conference Melbourne**. [S.l.: s.n.], 2018. p. 21–26. Citation on page 32.

AJAYI, T.; GOMES, J. S.; BERA, A. A review of co2 storage in geological formations emphasizing modeling, monitoring and capacity estimation approaches. **Petroleum Science**, Springer, v. 16, p. 1028–1063, 2019. Citation on page 32.

AKAI, T.; SAITO, N.; HIYAMA, M.; OKABE, H. Numerical modelling on co2 storage capacity in depleted gas reservoirs. **Energies**, MDPI, v. 14, n. 13, p. 3978, 2021. Citation on page 33.

ALLEN, R.; NILSEN, H. M.; ANDERSEN, O.; LIE, K.-A. On obtaining optimal well rates and placement for co2 storage. **Computational Geosciences**, Springer, v. 21, n. 5-6, p. 1403–1422, 2017. Citation on page 32.

ALQAHTANI, A. *et al.* Uncertainty analysis of co2 storage in deep saline aquifers using machine learning and bayesian optimization. **Energies**, MDPI, v. 16, n. 4, p. 1684, 2023. Citation on page 36.

AMINU, M. D.; NABAVI, S. A.; ROCHELLE, C. A.; MANOVIC, V. A review of developments in carbon dioxide storage. **Applied Energy**, Elsevier, v. 208, p. 1389–1419, 2017. Citation on page 37.

AVANSI, G. D.; SCHIOZER, D. J. Unisim-i: synthetic model for reservoir development and management applications. **International Journal of Modeling and Simulation for the Petroleum Industry**, Brazil, v. 9, n. 1, p. 21–30, 2015. Citation on page 49.

BABU, D.; ODEH, A. S. Productivity of a horizontal well. **SPE Reservoir Engineering (Society of Petroleum Engineers)**, v. 4, n. 4, p. 417–421 18298, 1989. ISSN 08859248. Citation on page 44.

BACHU, S. Sequestration of co2 in geological media: criteria and approach for site selection in response to climate change. **Energy conversion and management**, Elsevier, v. 41, n. 9, p. 953–970, 2000. Citation on page 29.

_____. Sequestration of co2 in geological media in response to climate change: road map for site selection using the transform of the geological space into the co2 phase space. **Energy Conversion and Management**, v. 43, n. 1, p. 87–102, 2002. ISSN 0196-8904. Citation on page 30.

_____. Screening and selection criteria, and characterisation techniques for the geological sequestration of carbon dioxide (co2).) **Capture and Storage Technology**, Elsevier Ltd, v. 2, p. 27 – 56, 2010. Citation on page 47.

_____. Review of co2 storage efficiency in deep saline aquifers. **International Journal of Greenhouse Gas Control**, Elsevier, v. 40, p. 188–202, 2015. Citation on page 41.

BANDILLA, K. W. *et al.* Impact of model complexity on co2 plume modeling at sleipner. **Energy Procedia**, Elsevier, v. 63, p. 3405–3415, 2014. Citation on page 41.

BEAR, J. **Dynamics of fluids in porous media**. [S.l.]: Dover Publications, 1972. Citation on page 53.

BENSON, S. M.; COLE, D. R. Co2 sequestration in deep sedimentary formations. **Elements**, Mineralogical Association of Canada, v. 4, n. 5, p. 325–331, 2008. Citation on page 39.

BOUCKAERT, S. *et al.* Net zero by 2050: A roadmap for the global energy sector. **International Energy Agency**, 2021. Citations on pages 19 and 22.

BRINCKERHOFF, P. *et al.* Accelerating the uptake of ccs: industrial use of captured carbon dioxide. **Global CCS Institute**, v. 260, 2011. Citation on page 24.

BRUHN, T. *et al.* Separating the debate on co2 utilisation from carbon capture and storage. **Environmental Science & Policy**, Elsevier, v. 60, p. 38–43, 2016. Citation on page 25.

CALLAS, C. *et al.* Criteria and workflow for selecting depleted hydrocarbon reservoirs for carbon storage. **Applied Energy**, Elsevier Ltd, v. 324, 2022. ISSN 03062619. Citations on pages 34 and 47.

_____. Incorporating data confidence and scoring sensitivity into site selection ranking in depleted hydrocarbon reservoirs. In: OTC. **Offshore Technology Conference**. [S.l.], 2023. Citation on page 35.

CÂMARA, G. A. B.; ANDRADE, J. C. S.; ROCHA, P. Tecnologia de armazenamento geológico de dióxido de carbono: panorama mundial e situação brasileira. UFF, 2011. Citation on page 27.

CÂMARA, G. A. B.; BATISTA, A.; CARVALHO, L. F. d. J.; ANDRADE, J. C. S.; ROCHA, P. The use of ccs technologies in large scale: an analysis of the brazilian legal framework. **Brazilian Journal of Petroleum and Gas**, v. 10, n. 4, 2016. Citation on page 27.

CAÑAS, S. S. M. Prospectivity mapping of the irati formation for co2 geological storage in the paraná basin. **San Martín CANAS, S. Perspectives to CO2 Geological Storage and Greenhouse Gas Negative Emissions in South-Southeastern Brazil: Paraná and Santos Sedimentary Basins, Sao Paulo: Blucher**, p. 61–72, 2022. Citation on page 28.

CANNON, S. **Petrophysics: a practical guide**. [S.l.]: John Wiley & Sons, 2015. Citation on page 45.

CARPENTER, M. *et al.* The co2qualstore guideline for selection, characterisation and qualification of sites and projects for geological storage of co2. **International Journal of Greenhouse Gas Control**, Elsevier Ltd, v. 5, n. 4, p. 942 – 951, 2011. ISSN 17505836. Citation on page 47.

CIOTTA, M. *et al.* Co2 storage potential of offshore oil and gas fields in brazil. **International Journal of Greenhouse Gas Control**, Elsevier Ltd, v. 112, 2021. ISSN 17505836. Citations on pages 19, 26, and 28.

COOK, J. *et al.* Consensus on consensus: a synthesis of consensus estimates on human-caused global warming. **Environmental Research Letters**, IOP Publishing, v. 11, n. 4, p. 048002, 2016. Citation on page 22.

COOPER, C. *et al.* A technical basis for carbon dioxide storage. **Energy Procedia**, v. 1, n. 1, p. 1727 – 1733, 2009. ISSN 18766102. Citation on page 47.

CRUZ, P. S. D. *et al.* The quality map: a tool for reservoir uncertainty quantification and decision making. **SPE Reservoir Evaluation and Engineering**, Society of Petroleum Engineers, v. 7, n. 1, p. 6 – 14, 2004. ISSN 10946470. Citation on page 44.

DAVIES, D.; SOMERVILLE, J.; HW, U. *et al.* Well location selection from a static model and multiple realizations of a geomodel using productivity-potential map technique. Society of Petroleum Engineers, 2006. Citation on page 45.

DAVIES, O. L. *et al.* **Statistical methods in research and production.** [S.l.]: Oliver and Boyd, London, 1947. Citation on page 60.

DECC, C. Roadmap: Supporting deployment of carbon capture and storage in the uk. **UK Department of Energy and Climate Change**, 2012. Citation on page 25.

DING, S. *et al.* Optimization of well placement by combination of a modified particle swarm optimization algorithm and quality map method. **Computational Geosciences**, Kluwer Academic Publishers, v. 18, n. 5, p. 747 – 762, 2014. ISSN 14200597. Citation on page 45.

_____. Well placement optimization using direct mapping of productivity potential and threshold value of productivity potential management strategy. **Computers and Chemical Engineering**, v. 121, p. 327–337, 2019. Citation on page 45.

DREXLER, S. *et al.* Impact of rock aging time on the initial wettability of minerals and analogue rocks using pre-salt fluids under reservoir conditions. **Offshore Technology Conference Brasil 2019, OTCB 2019**, Offshore Technology Conference, 2020. Citations on pages 19 and 26.

EIGESTAD, G. T.; DAHLE, H. K.; HELLEVANG, B.; RIIS, F.; JOHANSEN, W. T.; ØIAN, E. Geological modeling and simulation of co2 injection in the johansen formation. **Computational Geosciences**, Springer, v. 13, n. 4, p. 435–450, 2009. Citation on page 40.

ENERDATA. **World Energy & Climate Statistics - Yearbook 2023**. 2023. <https://yearbook.enerdata.net/co2/emissions-co2-data-from-fuel-combustion.html>. Citation on page 23.

ESPINOZA, D. *et al.* Optimization of co2 injector location and rate in compartmentalized reservoirs. **56th U.S. Rock Mechanics/Geomechanics Symposium**, American Rock Mechanics Association (ARMA), 2022. Citation on page 20.

FARAMARZI-PALANGAR, M.; MIRZAEI-PAIAMAN, A. Investigating dynamic rock quality in two-phase flow systems using tem-function: A comparative study of different rock typing indices. **Petroleum Research**, KeAi Publishing Communications Ltd., v. 6, n. 1, p. 16 – 25, 2021. ISSN 20962495. Citation on page 54.

FEDERAL, G. Plano nacional sobre mudança do clima-pnmc. **Brasília: Governo federal**, 2008. Citations on pages 19 and 26.

FOTIAS, S. P.; ISMAIL, I.; GAGANIS, V. Optimization of well placement in carbon capture and storage (ccs): Bayesian optimization framework under permutation invariance. **Applied Sciences**, MDPI, v. 14, n. 8, p. 3528, 2024. Citation on page 36.

FREEDMAN, D.; DIACONIS, P. On the histogram as a density estimator: L 2 theory. **Zeitschrift für Wahrscheinlichkeitstheorie und verwandte Gebiete**, Citeseer, v. 57, n. 4, p. 453–476, 1981. Citation on page 60.

FREEMAN, L. Centrality in social networks conceptual clarification. **Social Networks**, v. 1, n. 3, p. 215 – 239, 1978. ISSN 03788733. Citation on page 62.

FURRE, A.-K. *et al.* 20 years of monitoring co2-injection at sleipner. **Energy Procedia**, Elsevier Ltd, v. 114, p. 3916 – 3926, 2017. ISSN 18766102. Citation on page 19.

GASDA, S. e. a. Vertical equilibrium with sub-scale analytical methods for geological co2 sequestration. **Computational Geosciences**, v. 13, n. 4, p. 469 – 481, 2009. ISSN 14200597. Citations on pages 109 and 110.

GELFAND, I.; FOMIN, S. Calculus of variations prentice-hall. **Inc., Englewood Cliffs**, 1963. Citation on page 53.

GONZALEZ, S. P. *et al.* Evaluation of consolidation parameter data trendings and comparison between prediction models for well-log velocities: A case study from the namorado oilfield (southern brazil). **Journal of Petroleum Science and Engineering**, Elsevier B.V., v. 180, p. 41 – 47, 2019. ISSN 09204105. Citation on page 49.

GOODMAN, A. *et al.* Us doe methodology for the development of geologic storage potential for carbon dioxide at the national and regional scale. **International Journal of Greenhouse Gas Control**, Elsevier Ltd, v. 5, n. 4, p. 952 – 965, 2011. ISSN 17505836. Citation on page 47.

GRATALOUP, S.; BONIJOLY, D.; BROSSE, E.; DREUX, R.; GARCIA, D.; HASANOV, V.; LESCANNE, M.; RENOUX, P.; THORAVAL, A. A site selection methodology for co2 underground storage in deep saline aquifers: case of the paris basin. **Energy Procedia**, Elsevier, v. 1, n. 1, p. 2929–2936, 2009. Citation on page 30.

GUERRA, N. Y.; NARAYANASAMY, R. Well location selection from multiple realizations of a geomodel using productivity potential maps–a heuristic technique. In: SPE. **SPE International Oil Conference and Exhibition in Mexico**. [S.l.], 2006. p. SPE–102903. Citation on page 45.

HEARN, C. *et al.* Geological factors influencing reservoir performance of the hartzog draw field, wyoming. **JPT, Journal of Petroleum Technology**, v. 36, n. 9, p. 1335 – 1344, 1984. ISSN 01492136. Citation on page 45.

HESSE, M. A.; ORR, F. M. *et al.* Gravity currents with residual trapping. **Journal of Fluid Mechanics**, Cambridge University Press, v. 611, p. 35–60, 2008. Citation on page 39.

HOLLOWAY, S.; SAVAGE, D. The potential for aquifer disposal of carbon dioxide in the uk. **Energy Conversion and Management**, Elsevier, v. 34, n. 9-11, p. 925–932, 1993. Citation on page 29.

HOMMA, T.; SALTELLI, A. Importance measures in global sensitivity analysis of nonlinear models. **Reliability Engineering & System Safety**, Elsevier, v. 52, n. 1, p. 1–17, 1996. Citation on page 72.

HOVORKA, S. D.; MECKEL, T. A.; TREVINO, R. H. Monitoring a large-volume injection at cranfield, mississippi—project design and recommendations. **International Journal of Greenhouse Gas Control**, Elsevier, v. 18, p. 345–360, 2013. Citation on page 37.

HU, T. *et al.* A study of co2 injection well selection in the naturally fractured undulating formation in the jurong oilfield, china. **International Journal of Greenhouse Gas Control**, Elsevier Ltd, v. 109, 2021. ISSN 17505836. Citation on page 20.

IEA. **Net Zero Roadmap: A Global Pathway to Keep the 1.5°C Goal in Reach**. [S.l.], 2023. Citation on page 19.

IGLESIAS, R. S. *et al.* Carbon capture and geological storage in brazil: an overview. **Greenhouse Gases: Science and Technology**, v. 5, n. 2, p. 119 – 130, 2015. ISSN 21523878. Citations on pages 19, 25, and 26.

INSTITUTE, G. C. **The Global Status of CCS 2018**. 2018. <https://www.globalccsinstitute.com/resources/publications-reports-research/global-status-of-ccs-report-2018/>. Citation on page 26.

IPCC, I. special report on carbon dioxide capture and storage. 2005. **Intergovernmental Panel on Climate Change, Working Group III**, 2005. Citations on pages 25, 29, and 38.

IZADPANAHI, A.; BLUNT, M. J.; KUMAR, N.; ALI, M.; TASSINARI, C. C. G.; SAMPAIO, M. A. A review of carbon storage in saline aquifers: Mechanisms, prerequisites, and key considerations. **Fuel**, Elsevier, v. 369, p. 131744, 2024. Citation on page 36.

JACCARD, P. The distribution of the flora in the alpine zone. 1. **New Phytologist**, v. 11, n. 2, p. 37 – 50, 1912. ISSN 0028646X. Citation on page 65.

JENKINS, C. R.; COOK, P. J.; ENNIS-KING, J.; UNDERSHULTZ, J.; BOREHAM, C.; DANCE, T.; CARITAT, P. D.; ETHERIDGE, D. M.; FREIFELD, B. M.; HORTLE, A. *et al.* Safe storage and effective monitoring of co2 in depleted gas fields. **Proceedings of the National Academy of Sciences**, National Acad Sciences, v. 109, n. 2, p. E35–E41, 2012. Citation on page 31.

JR, W. E. Flow unit concept-integrated approach to reservoir description for engineering projects. **AAPG (Am. Assoc. Pet. Geol.) Bull.;(United States)**, ARCO Oil and Gas Co., Plano, TX, v. 71, n. CONF-870606-, 1987. Citation on page 45.

JR, W. E. *et al.* Flow units for reservoir characterization: Part 6. geological methods. **ME 10: Development Geology Reference Manual**, AAPG Special Volumes, 1992. Citation on page 45.

JUANES, R.; MACMINN, C. W. *et al.* The footprint of the co2 plume during carbon dioxide storage in saline aquifers: storage efficiency for capillary trapping at the basin scale. **Transport in porous media**, Springer, v. 82, p. 19–30, 2010. Citation on page 40.

JUN, C. *et al.* Optimization of well placement and operating conditions for various well patterns in co2 sequestration in the pohang basin, korea. **International Journal of Greenhouse Gas Control**, Elsevier Ltd, v. 90, 2019. ISSN 17505836. Citation on page 19.

KETZER, J. *et al.* **Brazilian atlas of CO2 capture and geological storage**. [S.l.]: EDIPUCRS, 2015. Citation on page 26.

KHARAKA, Y. K.; COLE, D. R.; HOVORKA, S. D.; GUNTER, W.; KNAUSS, K. G.; FREIFELD, B. Gas-water-rock interactions in frio formation following co2 injection: Implications for the storage of greenhouse gases in sedimentary basins. **Geology**, Geological Society of America, v. 34, n. 7, p. 577–580, 2006. Citation on page 37.

KHARGHORIA, A. *et al.* Productivity-based method for selection of reservoir drilling target and steering strategy. In: SPE. **SPE/IADC Middle East Drilling Technology Conference and Exhibition**. [S.l.], 2003. p. SPE–85341. Citations on pages 45 and 57.

KOPP, A.; CLASS, H.; HELMIG, R. Investigations on co2 storage capacity in saline aquifers—part 2: Estimation of storage capacity coefficients. **International Journal of Greenhouse Gas Control**, Elsevier, v. 3, n. 3, p. 277–287, 2009. Citation on page 40.

KUMAR, A.; OZAH, R.; NOH, M.; POPE, G. A.; BRYANT, S.; SEPEHRNOORI, K.; LAKE, L. W. Reservoir simulation of co2 storage in deep saline aquifers. **Spe Journal**, OnePetro, v. 10, n. 03, p. 336–348, 2005. Citations on pages 30 and 38.

KUMAR, D.; SINGH, A.; KUMAR, P.; JHA, R. K.; SAHOO, S. K.; JHA, V. Sobol sensitivity analysis for risk assessment of uranium in groundwater. **Environmental Geochemistry and health**, Springer, v. 42, p. 1789–1801, 2020. Citation on page 71.

LAKE, L. W. Enhanced oil recovery. Old Tappan, NJ; Prentice Hall Inc., 1989. Citation on page 40.

LI, C.; MAGGI, F.; ZHANG, K.; GUO, C.; GAN, Y.; EL-ZEIN, A.; PAN, Z.; SHEN, L. Effects of variable injection rate on reservoir responses and implications for co2 storage in saline aquifers. **Greenhouse Gases: Science and Technology**, Wiley Online Library, v. 9, n. 4, p. 652–671, 2019. Citation on page 42.

LIE, K.-A. An introduction to reservoir simulation using matlab: user guide for the matlab reservoir simulation toolbox (mrst). **Sintef Ict**, Departement of Applied Mathematics Oslo, Norway, v. 118, 2016. Citation on page 108.

_____. **An introduction to reservoir simulation using MATLAB/GNU Octave: User guide for the MATLAB Reservoir Simulation Toolbox (MRST)**. [S.l.]: Cambridge University Press, 2019. Citations on pages 49, 66, and 112.

LIE, K.-A.; NILSEN, H. M.; ANDERSEN, O.; MøYNER, O. A simulation workflow for large-scale co2 storage in the norwegian north sea. **Computational Geosciences**, Springer International Publishing, v. 20, n. 3, p. 607 – 622, 2016. ISSN 14200597. Citation on page 31.

LIU, N.; JALALI, Y. Closing the loop between reservoir modeling and well placement and positioning. In: **SPE Intelligent Energy International Conference and Exhibition**. [S.l.: s.n.], 2006. v. 1, p. 11–23. Citations on pages 45 and 57.

LUBOŃ, K. Influence of injection well location on co2 geological storage efficiency. **Energies**, MDPI, v. 14, n. 24, 2021. ISSN 19961073. Citations on pages 19 and 33.

LUO, J. *et al.* Advances in subsea carbon dioxide utilization and storage. **Energy Reviews**, Elsevier, p. 100016, 2023. Citation on page 27.

MACDOWELL, N.; FLORIN, N.; BUCHARD, A.; HALLETT, J.; GALINDO, A.; JACKSON, G.; ADJIMAN, C. S.; WILLIAMS, C. K.; SHAH, N.; FENNELL, P. An overview of co2 capture technologies. **Energy & Environmental Science**, Royal Society of Chemistry, v. 3, n. 11, p. 1645–1669, 2010. Citation on page 22.

MARTINI, R. *et al.* Use of quality maps in reservoir management. **Journal of the Brazilian Society of Mechanical Sciences and Engineering**, v. 27, n. 4, p. 463–468, 2005. Citation on page 44.

MCBRIDE-WRIGHT, M.; MAITLAND, G. C.; TRUSLER, J. M. Viscosity and density of aqueous solutions of carbon dioxide at temperatures from (274 to 449) k and at pressures up to 100 mpa. **Journal of Chemical & Engineering Data**, ACS Publications, v. 60, n. 1, p. 171–180, 2015. Citation on page 37.

MEYER, R.; MAY, F.; MÜLLER, C.; GEEL, K.; BERNSTONE, C. Regional search, selection and geological characterization of a large anticlinal structure, as a candidate site for co2-storage in northern germany. **Environmental Geology**, Springer, v. 54, n. 8, p. 1607–1618, 2008. Citation on page 30.

MICHAEL, K. *et al.* Geological storage of co2 in saline aquifers—a review of the experience from existing storage operations. **International journal of greenhouse gas control**, Elsevier, v. 4, n. 4, p. 659–667, 2010. Citation on page 29.

MIN, B. *et al.* Optimal well placement based on artificial neural network incorporating the productivity potential. **Energy Sources, Part A: Recovery, Utilization and Environmental Effects**, v. 33, n. 18, p. 1726–1738, 2011. Citation on page 45.

MIRZAEI-PAIAMAN, A.; GHANBARIAN, B. A new method for characterizing dynamic reservoir quality: Implications for quality maps in reservoir simulation and rock type classification. **Journal of Petroleum Science and Engineering**, Elsevier B.V., v. 218, 2022. ISSN 09204105. Citation on page 54.

MIRZAEI-PAIAMAN, A. *et al.* A new approach in petrophysical rock typing. **Journal of Petroleum Science and Engineering**, Elsevier B.V., v. 166, p. 445 – 464, 2018. ISSN 09204105. Citations on pages 45 and 54.

_____. A further verification of fzi* and psrti: Newly developed petrophysical rock typing indices. **Journal of Petroleum Science and Engineering**, v. 175, p. 693–705, 2019. Citations on pages 45 and 54.

MIYAGI, A. *et al.* Well placement optimization for carbon dioxide capture and storage via cma-es with mixed integer support. In: **GECCO 2018 Companion - Proceedings of the 2018 Genetic and Evolutionary Computation Conference Companion**. [S.l.]: Association for Computing Machinery, Inc, 2018. p. 1696 – 1703. ISBN 978-145035764-7. Citation on page 20.

NA, J.; XU, T.; YUAN, Y.; FENG, B.; TIAN, H.; BAO, X. An integrated study of fluid–rock interaction in a co2-based enhanced geothermal system: A case study of songliao basin, china. **Applied Geochemistry**, Elsevier, v. 59, p. 166–177, 2015. Citation on page 29.

NAKAJIMA, L.; SCHIOZER, D. Horizontal well placement optimization using quality map definition. In: ONEPETRO. **Canadian International Petroleum Conference**. [S.l.], 2003. p. PETSOC–2003–053. Citation on page 44.

NASA. **NASA, NOAA Analyses Reveal Record-Shattering Global Warm Temperatures in 2015**. 2015. <https://www.nasa.gov/news-release/nasa-noaa-analyses-reveal-record-shattering-global-warm-temperatures-in-2015/>. Citation on page 22.

NEWMAN, M. **Networks: An Introduction**. New York: Oxford University Press, 2010. Citation on page 62.

NILSEN, H. M.; LIE, K.-A.; ANDERSEN, O. Robust simulation of sharp-interface models for fast estimation of co2 trapping capacity in large-scale aquifer systems. **Computational Geosciences**, Springer International Publishing, v. 20, n. 1, p. 93 – 113, 2016. ISSN 14200597. Citations on pages 12, 41, 67, 112, and 113.

NILSEN, H. M. *et al.* Field-case simulation of co2-plume migration using vertical-equilibrium models. **Energy Procedia**, Elsevier, v. 4, p. 3801–3808, 2011. Citations on pages 40 and 112.

____. Analysis of co2 trapping capacities and long-term migration for geological formations in the norwegian north sea using mrst-co2lab. **Computers and Geosciences**, Elsevier Ltd, v. 79, p. 15 – 26, 2015. ISSN 00983004. Citations on pages 31 and 74.

____. Spill-point analysis and structural trapping capacity in saline aquifers using mrst-co2lab. **Computers and Geosciences**, Elsevier Ltd, v. 75, p. 33 – 43, 2015. ISSN 00983004. Citations on pages 31, 49, 50, 51, and 53.

____. Using sensitivities and vertical-equilibrium models for parameter estimation of co2 injection models with application to sleipner data. **Energy Procedia**, Elsevier, v. 114, p. 3476–3495, 2017. Citations on pages 67 and 112.

NORDBOTTEN, J. M.; CELIA, M. A. Similarity solutions for fluid injection into confined aquifers. **Journal of Fluid Mechanics**, Cambridge University Press, v. 561, p. 307–327, 2006. Citation on page 108.

NORDBOTTEN, J. M.; CELIA, M. A.; BACHU, S. Injection and storage of co2 in deep saline aquifers: analytical solution for co2 plume evolution during injection. **Transport in Porous media**, Springer, v. 58, p. 339–360, 2005. Citations on pages 30 and 108.

NUNES, R. de C.; COSTA, H. K. de M. Operacao e fechamento de instalacoes de armazenamento para atividades de ccs no brasil. In: **10º CONGRESSO BRASILEIRO DE PESQUISA E DESENVOLVIMENTO EM PETRÓLEO E GÁS**. [S.l.: s.n.], 2019. p. 1–8. Citation on page 27.

OLIVEIRA, G. *et al.* Competitive placement of oil perforation zones in hydraulic flow units from centrality measures. **Journal of Petroleum Science and Engineering**, Elsevier B.V., v. 147, p. 282 – 291, 2016. ISSN 09204105. Citation on page 59.

_____. Non-uniform injector/producer well pattern designs induced by morphology and anisotropy of flow units. **Journal of Petroleum Science and Engineering**, Elsevier B.V., v. 186, 2020. ISSN 09204105. Citation on page 59.

_____. Well placement subclustering within partially oil-saturated flow units. **Journal of Petroleum Science and Engineering**, Elsevier B.V., v. 196, 2021. ISSN 09204105. Citation on page 62.

OLIVEIRA, G. P. *et al.* Gawps: A mrst-based module for wellbore profiling and graphical analysis of flow units. **Advances in Geo-Energy Research**, Yandy Scientific Press, v. 6, n. 1, p. 38 – 53, 2022. ISSN 22079963. Citations on pages 54 and 59.

OLIVEIRA, S. B. de; TASSINARI, C. C.; ABRAHAM-A, R. M.; TORRESI, I. 3d implicit modeling applied to the evaluation of co2 geological storage in the shales of the irati formation, paraná basin, southeastern brazil. **Greenhouse Gases: Science and Technology**, Wiley Online Library, v. 11, n. 5, p. 1024–1042, 2021. Citation on page 28.

PAPOULIS, S. **Probability, Random Variables and Stochastic Processes by Athanasios**. [S.l.]: Boston: McGraw-Hill, 2002. Citation on page 71.

PETTERSEN, Ø. Basics of reservoir simulation with the eclipse reservoir simulator. **Lecture Notes. University of Bergen, Norway**, v. 114, 2006. Citation on page 32.

POULADI, B. *et al.* Enhancement of spsa algorithm performance using reservoir quality maps: Application to coupled well placement and control optimization problems. **Journal of Petroleum Science and Engineering**, v. 189, 2020. Citation on page 45.

RASOOL, M. H. *et al.* Selecting geological formations for co2 storage: A comparative rating system. **Sustainability**, MDPI, v. 15, n. 8, p. 6599, 2023. Citation on page 34.

RAVALEC, M. L. Optimizing well placement with quality maps derived from multi-fidelity meta-models. In: ONEPETRO. **SPE Europec/EAGE Annual Conference**. [S.l.], 2012. p. SPE–154416–MS. Citation on page 45.

RAZA, A.; GHOLAMI, R.; REZAEE, R.; BING, C. H.; NAGARAJAN, R.; HAMID, M. A. Co2 storage in depleted gas reservoirs: A study on the effect of residual gas saturation. **Petroleum**, Elsevier, v. 4, n. 1, p. 95–107, 2018. Citation on page 42.

RINGROSE, P. S. The ccs hub in norway: some insights from 22 years of saline aquifer storage. **Energy Procedia**, Elsevier, v. 146, p. 166–172, 2018. Citation on page 32.

RISE, S.-L. A semi-empirical approach to projecting future. **Mineral. Petrol**, v. 147, p. 155, 2004. Citation on page 22.

RODRIGUES, H. W. *et al.* Multi-objective optimization of co2 recycling operations for ccus in pre-salt carbonate reservoirs. **International Journal of Greenhouse Gas Control**, Elsevier Ltd, v. 119, 2022. ISSN 17505836. Citations on pages 19 and 26.

ROMEO, L.; THOMAS, R.; MARK-MOSER, M.; BEAN, A.; BAUER, J.; ROSE, K. Data-driven offshore co2 saline storage assessment methodology. **International Journal of Greenhouse Gas Control**, Elsevier, v. 119, p. 103736, 2022. Citation on page 33.

ROQUE, W. *et al.* Production zone placements based on maximum closeness centrality as strategy for oil recovery. **Journal of Petroleum Science and Engineering**, v. 156, p. 430–441, 2017. Citation on page 59.

ROSE, S. K. *et al.* The paris agreement and next steps in limiting global warming. **Climatic Change**, Springer, v. 142, n. 1-2, p. 255–270, 2017. Citation on page 22.

SÁINZ, A.; NARDI, A.; ABARCA, E.; GRANDIA, F. Effect of the injection well location on the co2 storage in dome-shaped reservoir. In: UNIVERSITAT POLITÈCNICA DE CATALUNYA. DEPARTAMENT D'ENGINYERIA DEL TERRENY, CARTOGRÀFICA I GEOFÍSICA. **International Symposium on Energy Geotechnics (1st.: 2015: Barcelona)**. [S.l.], 2015. Citation on page 41.

SALTELLI, A. Making best use of model evaluations to compute sensitivity indices. **Computer physics communications**, Elsevier, v. 145, n. 2, p. 280–297, 2002. Citation on page 71.

SALTELLI, A.; ANNONI, P.; AZZINI, I.; CAMPOLONGO, F.; RATTO, M.; TARANTOLA, S. Variance based sensitivity analysis of model output. design and estimator for the total sensitivity index. **Computer Physics Communications**, v. 181, n. 2, p. 259–270, 2010. ISSN 0010-4655. Citation on page 71.

SCHNAAR, G.; DIGIULIO, D. C. Computational modeling of the geologic sequestration of carbon dioxide. **Vadose Zone Journal**, Soil Science Society of America, v. 8, n. 2, p. 389–403, 2009. Citation on page 30.

SCOTT, D. W. **Multivariate density estimation: theory, practice, and visualization**. [S.l.]: John Wiley & Sons, 2015. Citation on page 60.

SHUKLA, R.; RANJITH, P.; HAQUE, A.; CHOI, X. A review of studies on co2 sequestration and caprock integrity. **Fuel**, Elsevier, v. 89, n. 10, p. 2651–2664, 2010. Citation on page 31.

SIQUEIRA, T. A.; IGLESIAS, R. S.; KETZER, J. M. Carbon dioxide injection in carbonate reservoirs–a review of co2-water-rock interaction studies. **Greenhouse Gases: Science and Technology**, Wiley Online Library, v. 7, n. 5, p. 802–816, 2017. Citation on page 37.

SLATT, R. M. *et al.* Scaling geologic reservoir description to engineering needs. **JPT, Journal of Petroleum Technology**, v. 42, n. 2, p. 202–210 18136, 1990. ISSN 01492136. Citation on page 45.

SOBOL, I. Sensitivity estimates for nonlinear mathematical models. **Math. Model. Comput. Exp.**, v. 1, p. 407, 1993. Citation on page 71.

_____. Global sensitivity indices for nonlinear mathematical models and their monte carlo estimates. **Mathematics and Computers in Simulation**, v. 55, n. 1, p. 271–280, 2001. Citation on page 70.

SOLOMON, S. e. a. Irreversible climate change due to carbon dioxide emissions. **Proceedings of the national academy of sciences**, National Acad Sciences, v. 106, n. 6, p. 1704–1709, 2009. Citation on page 22.

STANGELAND, A. A model for the co2 capture potential. **international journal of greenhouse gas control**, Elsevier, v. 1, n. 4, p. 418–429, 2007. Citation on page 30.

STOCKER, T. **Climate change 2013: the physical science basis: Working Group I contribution to the Fifth assessment report of the Intergovernmental Panel on Climate Change**. [S.l.]: Cambridge university press, 2014. Citation on page 22.

STOPA, J. *et al.* Optimization of well placement and control to maximize co2 trapping during geologic sequestration. **AGH Drilling, Oil, Gas**, Akademia Górniczo-Hutnicza im. Stanisława Staszica w Krakowie. Wydawnictwo AGH, v. 33, n. 1, p. 93–104, 2016. Citation on page 20.

STURGES, H. A. The choice of a class interval. **Journal of the American Statistical Association**, v. 21, n. 153, p. 65 – 66, 1926. ISSN 01621459. Citation on page 60.

TAWARE, S. *et al.* Well placement optimization in a mature carbonate waterflood using streamline-based quality maps. **Society of Petroleum Engineers - SPE Oil and Gas India Conference and Exhibition 2012, OGIC**, 2012. Citation on page 45.

URYCH, T.; CHEĆKO, J.; MAGDZIARCZYK, M.; SMOLIŃSKI, A. Numerical simulations of carbon dioxide storage in selected geological structures in north-western poland. **Frontiers in Energy Research**, v. 10, p. 827794, 2022. Citation on page 42.

VERHEGGEN, B. *et al.* Scientists' views about attribution of global warming. **Environmental science and technology**, ACS Publications, v. 48, n. 16, p. 8963–8971, 2014. Citation on page 22.

VESELY, L. *et al.* Effect of impurities on compressor and cooler in supercritical co2 cycles. **Journal of Energy Resources Technology, Transactions of the ASME**, American Society of Mechanical Engineers (ASME), v. 141, n. 1, 2019. ISSN 01950738. Citation on page 59.

WEI, N.; LI, X.; JIAO, Z.; STAUFFER, P. H.; ELLETT, K. M.; MIDDLETON, R. S. R. A hierarchical framework for co2 storage capacity in deep saline aquifer formations. **Frontiers in Earth Science**, Los Alamos National Lab.(LANL), Los Alamos, NM (United States), v. 9, n. LA-UR-21-21834, 2022. Citation on page 33.

YAMASAKI, A. An overview of co2 mitigation options for global warming—emphasizing co2 sequestration options. **Journal of chemical engineering of Japan**, The Society of Chemical Engineers, Japan, v. 36, n. 4, p. 361–375, 2003. Citation on page 23.

YANG, B. *et al.* Advances in carbon dioxide storage projects: Assessment and perspectives. **Energy & Fuels**, ACS Publications, v. 37, n. 3, p. 1757–1776, 2023. Citation on page 35.

YANG, H.; XU, Z.; FAN, M.; GUPTA, R.; SLIMANE, R. B.; BLAND, A. E.; WRIGHT, I. Progress in carbon dioxide separation and capture: A review. **Journal of environmental sciences**, Elsevier, v. 20, n. 1, p. 14–27, 2008. Citation on page 29.

YANG, L.; RUI, W.; QINGMIN, Z.; ZHAOJIE, X.; YINBANG, Z. A co2 storage potential evaluation method for saline aquifers in a petroliferous basin. **Petroleum Exploration and Development**, Elsevier, v. 50, n. 2, p. 484–491, 2023. Citation on page 34.

YUE, P.; ZHANG, R.; SHENG, J. J.; YU, G.; LIU, F. Study on the influential factors of co2 storage in low permeability reservoir. **Energies**, MDPI, v. 15, n. 1, p. 344, 2022. Citation on page 42.

ZHANG, X.-Y.; TRAME, M. N.; LESKO, L. J.; SCHMIDT, S. Sobol sensitivity analysis: a tool to guide the development and evaluation of systems pharmacology models. **CPT: pharmacometrics & systems pharmacology**, Wiley Online Library, v. 4, n. 2, p. 69–79, 2015. Citation on page 71.

ZHAO, X. *et al.* The co2 storage capacity evaluation: Methodology and determination of key factors. **Journal of the Energy Institute**, Elsevier, v. 87, n. 4, p. 297–305, 2014. Citation on page 31.

ZOBACK, M.; SMIT, D. Meeting the challenges of large-scale carbon storage and hydrogen production. **Proceedings of the National Academy of Sciences of the United States of America**, National Academy of Sciences, v. 120, n. 11, 2023. ISSN 00278424. Citation on page 19.

ZUCATELLI, P. J. Estudo sobre a influência da permeabilidade no meio poroso em projetos de injeção e armazenamento geológico de co2. **Latin American Journal of Energy Research**, v. 3, n. 1, p. 17–24, 2016. Citation on page 42.

ZUCATELLI, P. J. *et al.* Estudo sobre o sequestro geológico de co2 em aquíferos salinos utilizando simulador com informações de caracterização de reservatórios. In: SOCIETY OF EXPLORATION GEOPHYSICISTS AND BRAZILIAN GEOPHYSICAL SOCIETY. **13th International Congress of the Brazilian Geophysical Society & EXPOGEF, Rio de Janeiro, Brazil, 26–29 August 2013**. [S.l.], 2013. p. 998–1003. Citation on page 41.

APPENDIX A - RELATIVE PERMEABILITY

Relative permeability measures the ability of a specific fluid (such as oil, water, or gas) to flow through a reservoir when other fluids are also present. It is crucial for reservoir simulation, as it directly affects the movement and production of fluids within the reservoir.

$$\kappa_{r,\alpha} = \kappa_{\alpha}^{e}/\kappa \qquad (A.1)$$

Relative permeabilities will generally be functions of saturation, which means that for a two-phase system we can write

$$\kappa_{r,w} = \kappa_{r,w}(s_w) \quad \text{and} \quad \kappa_{r,c} = \kappa_{r,c}(s_c) \qquad (A.2)$$

It is important to note that relative permeabilities are generally nonlinear functions of saturations, meaning the sum of these functions at a specific location (with a specific composition) is not necessarily equal to one. Therefore, it is common practice to associate a unique set of curves with each rock type represented in the geological model. While relative permeabilities may also depend on pore-size distribution, fluid viscosity, and temperature, these factors are typically ignored in models of conventional reservoirs.

In simplified models, it is common to assume that $\kappa_{r,\alpha}$ are monotone functions that assume unique values in $[0,1]$ for all values $s_\alpha \in [0,1]$, so that $\kappa_{r,\alpha} = 1$ corresponds to the case with fluid α occupying the entire pore space, and $\kappa_{r,\alpha} = 0$ when $s_\alpha = 0$ (Figure 41).
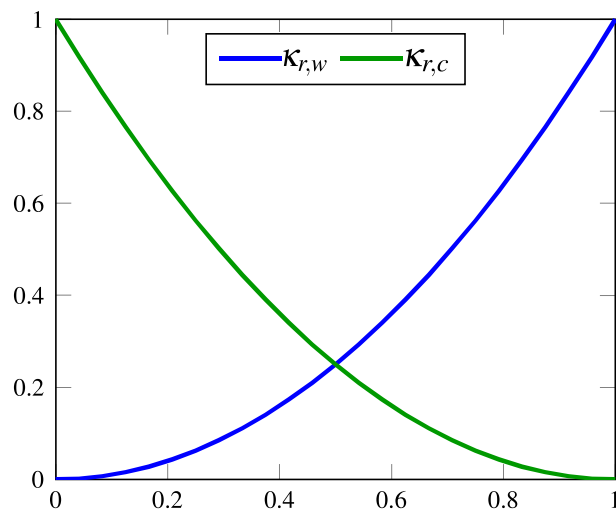

Figure 41 – Illustration of relative permeabilities for a two-phase system. Source: (LIE, 2016).

Due to the significant density difference between the injected CO_2 and the resident brine (NORDBOTTEN; CELIA; BACHU, 2005), the system exhibits strong buoyant segregation (NORDBOTTEN; CELIA, 2006). To develop the equations for the numerical simulator,

we start with a three-dimensional system (x, y, z), where two fluids, the non-wetting (CO_2-rich) phase (c) and the wetting (brine) phase (w), are separated by a sharp interface within an aquifer of thickness H (Figure 42). Initially, the system is saturated with the wetting phase. The distance from the datum to the bottom of the aquifer is b_1, to the interface is b_2, and to the top of the aquifer is b_3. Thus, $b_3 - b_1 = H$ and $b_3 - b_2 = h$, as shown in Figure 42. We consider incompressible flow within this system. For simplicity, we present the approximation for a primary drainage system, with the imbibition process discussed later.
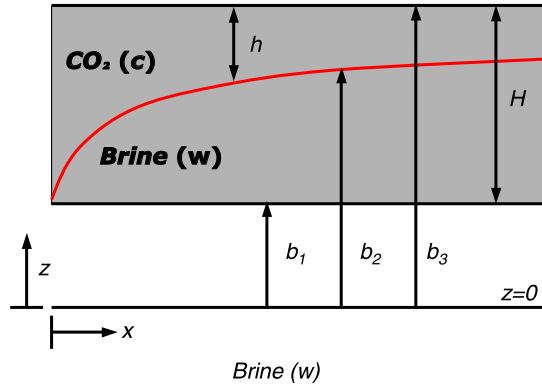

Figure 42 – Schematic of vertically averaged CO_2-brine system. Source: adapted by (GASDA, 2009).

We consider the system starts fully saturated with brine, which is then displaced by the injected CO_2, leaving only residual brine behind the CO_2–brine interface. With the assumption of a sharp interface between the two fluids, the local relative permeability in each phase, $\kappa_{r,\alpha}$, is the endpoint value at maximum saturation of the phase, $\kappa_{r,\alpha}^{\circ}$, as shown in Figure 43. Relative permeability is found by special core analysis (SCAL).

In the case of the brine phase, the local relative permeability is $\kappa_{rw}^{\circ} = 1$ because the region is still fully saturated with the brine phase. For the CO_2 phase, the relative permeability at maximum saturation, $\kappa_{r,c}^{\circ}$, is the value of the local function at $s_c = (1 - s_{Rw})$. Within the context of a vertically averaged system, the local values of relative permeability are scaled by the height of the interface relative to the total thickness of the aquifer. The interface height can in turn be related to the vertically averaged saturation through Equation A.3 and Equation A.4, leading to pseudo-relative permeability functions. *In the simple case where the intrinsic permeability is homogenous in the vertical direction, the pseudo-relative permeability functions reduce to scalars and are linear with respect to vertically averaged saturation:*

$$\tilde{\kappa}_{r,w} = \frac{H - h}{H} = \bar{s}_w - \frac{h}{H} s_{Rw}, \tag{A.3}$$

$$\tilde{\kappa}_{r,c} = \kappa_{r,c}^{\circ} \frac{h}{H} = \kappa_{r,c}^{\circ} \frac{\bar{s}_n}{(1 - s_{Rw})} \tag{A.4}$$

Once the injection operation is completed, the system will undergo imbibition in some portions of the domain where the CO_2–brine interface is receding. It is still possible to have
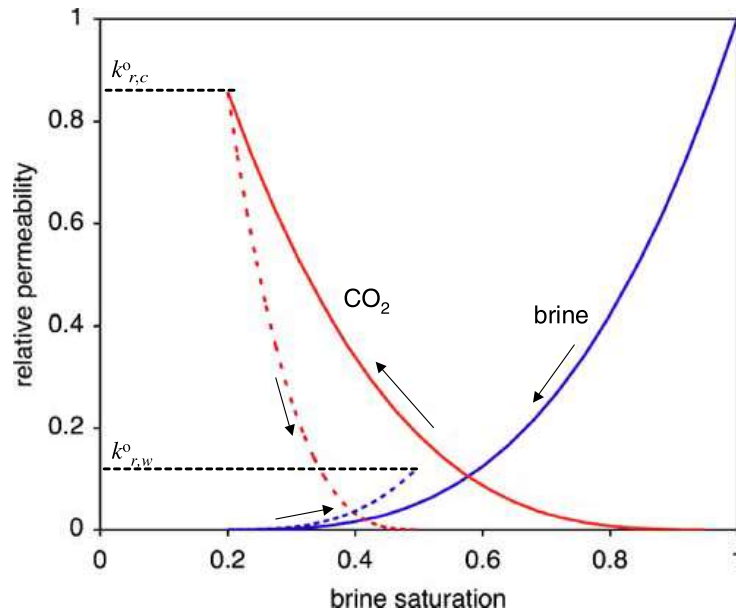
Figure 43 – Hypothetical local relative permeability drainage (solid line) and imbibition (dotted line) curves for CO_2 and brine. The maximum values of relative permeability for the CO_2 phase at residual brine and for the brine phase at residual CO_2 are indicated on the figure. Source: (GASDA, 2009).

primary drainage along the leading edge of the plume, especially if there is angle to the top surface of the aquifer along which the CO_2 will migrate upslope over time. Residual CO_2 will be trapped in the pore space during imbibition, leaving some residual saturation of the CO_2 behind. This phenomenon leads to local and average relative permeability functions that are hysteretic in nature. Thus when solving this system, different relative permeability values are calculated depending on whether the system is in drainage or imbibition. It should be noted that residual CO_2 will only be trapped within the fraction of the aquifer between the current location of the interface and the historically lowest height of the interface at that spatial location, which corresponds to the maximum thickness of CO_2 which we refer to as $h_{\max}(x,y)$. Thus wherever imbibition has occurred, the vertically averaged phase saturations become,

$$\bar{s}_w = \frac{1}{H}\left[(H - h_{\max}) + h s_{Rw} + (h_{\max} - h)(1 - s_{Rc})\right], \tag{A.5}$$

$$\bar{s}_c = \frac{1}{H}\left[h(1 - s_{Rw}) + (h_{\max} - h)s_{Rc}\right] \tag{A.6}$$

The corresponding effective relative permeability functions are similar to drainage case, except now instead of two regions with either fully saturated brine or partially saturated CO_2 with immobile brine, there is an additional region of partially saturated brine with immobile CO_2. Therefore, the brine phase effective relative permeability needs to account for the ad-

ditional region of partially saturated brine and the reduced local relative permeability in that region $(\kappa_{r,w}^{\circ} < 1)$,

$$\tilde{\kappa}_{r,w} = \frac{1}{H} \left[H - h_{\max} + \kappa_{r,w}^{\circ} (h_{\max} - h) \right] \tag{A.7}$$

In the Appendix B we will see the importance of relative permeability in calculating upscaled relative mobilities.

APPENDIX B - VERTICAL-EQUILIBRIUM MODEL

CO_2 exhibits high mobility, and when introduced into a porous rock formation, the resulting plume of supercritical fluid can traverse considerable distances. A typical saline aquifer earmarked for CO_2 storage can be conceptualized as a thin, gently inclined sheet spanning thousands of square kilometers. Within this sheet, the flow of CO_2 is typically confined to slender layers beneath the sealing caprock or other vertically impeding barriers with low permeability. This leads to a substantial contrast in lateral and vertical scales. Coupled with variations in density between the supercritical CO_2 plume and the underlying brine, this results in nearly instantaneous vertical fluid segregation compared to the upward migration. The tendency of CO_2 to form a relatively flat fluid interface arises from pressure distribution, which, in turn, is highly dependent on vertical flow. To prevent significant inaccuracies in predicting upward migration, it is imperative to accurately represent the vertical fluid distribution. In practical terms, this necessitates the utilization of a higher grid resolution than what is typically feasible in conventional 3D simulators. Consequently, such simulations are often under-resolved unless executed using large-scale systems designed for high-performance computing.

In a vertical equilibrium model, the fundamental assumption is that the flow system achieves a state of vertical equilibrium, enabling the determination of the vertical distribution of fluid phases through analytical expressions. Subsequently, the flow equations can be integrated in the vertical direction to derive a simplified model. This approach, widely employed in various branches of physics such as the description of water waves and creep flow, proves effective. Vertical integration not only reduces the spatial dimensions and, consequently, the requisite number of grid cells, but also diminishes the coupling between pressure and fluid transport. This leads to an enhancement in the characteristic time constants of the problem. Consequently, simulations based on vertical equilibrium, often termed as vertical-equilibrium simulations, typically exhibit orders of magnitude faster computation and substantially lower memory consumption compared to conventional 3D simulators (NILSEN *et al.*, 2011; NILSEN; LIE; ANDERSEN, 2016; NILSEN *et al.*, 2017; LIE, 2019).

Consider brine as the wetting fluid and CO_2 as the non-wetting fluid. Assume incompressible rock and fluids, no capillary forces, and impermeable top and bottom boundaries of the aquifer. Under these conditions, mass conservation and Darcy's law can be expressed as follows:

$$\frac{\partial(\phi s_\alpha)}{\partial t} + \nabla \cdot (\mathbf{u}_\alpha) \quad = \quad q_\alpha, \quad \alpha = w, c, \tag{B.1a}$$

$$\mathbf{u}_\alpha \quad = \quad -\kappa \lambda_\alpha (\nabla p - \rho_\alpha \mathbf{g}), \tag{B.1b}$$

where ρ_α is the density, q is the volumetric flux resulting from sources or sinks, α indicates the

fluid, λ_α is the fluid mobility, *dependent on the relative permeability and fluid viscosity*, p is the pressure, and $\mathbf{g}$ is the gravitational acceleration.

Let $(\mathbf{e}_\xi, \mathbf{e}_\eta, \mathbf{e}_\zeta)$ be a curvilinear coordinate system oriented to closely align with the global system $(\mathbf{e}_x, \mathbf{e}_y, \mathbf{e}_z)$, with a slight tilt ensuring that locally, $\mathbf{e}_\zeta$ is perpendicular to the main flow direction (ignoring small and medium-scale oscillations). The tilt is solely dependent on ξ and η, assumed to vary smoothly, and is maintained at all points within modest limits (a few degrees). Let $\mathbf{g}$ and ∇ be given by

$$\mathbf{g} = \mathbf{g}_{||} + \mathbf{g}_\zeta \mathbf{e}_\zeta \tag{B.2}$$

and

$$\nabla = \nabla_{||} + \mathbf{e}_\zeta \partial_\zeta, \tag{B.3}$$

respectively, where $||$ means the $(\mathbf{e}_\xi, \mathbf{e}_\eta)$ components of a vector/operator. Within the updated coordinate system, the aquifer is characterized by the top surface $Z(\xi, \eta)$ and its thickness $H(\xi, \eta)$ in the ζ-direction (Figure 44). Capital letters denote quantities in the upscaled model.
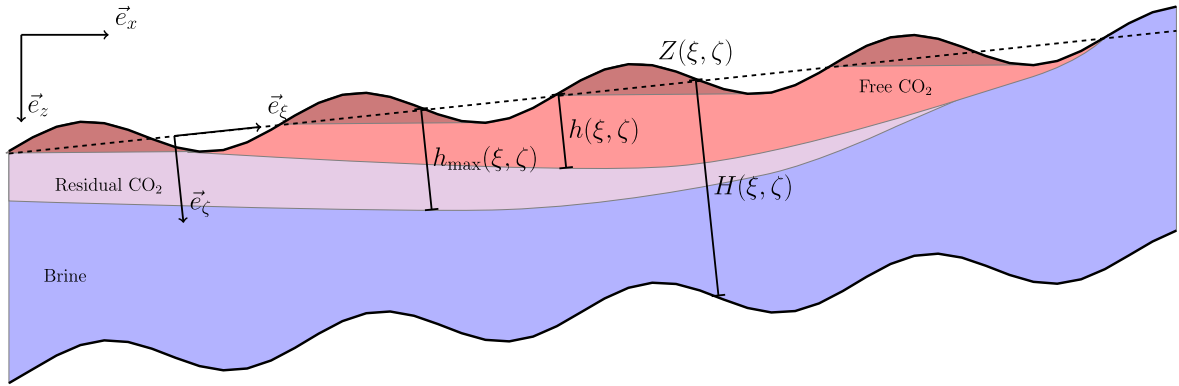

Figure 44 – Diagram illustrating the fluid distribution and coordinate systems employed for developing the fundamental vertical-equilibrium model. Source: (NILSEN; LIE; ANDERSEN, 2016).

In Figure 44, $h(\xi, \eta)$ represents the interface between CO_2 and brine, with h_{max} denoting the historical maximum value of h at a specific location. The *dashed line* denotes the assumed mean flow direction within the aquifer, depicted as *straight* in this illustration but permitted to be *slightly curved* in the general case. Performing the integration of equation B.1a from the upper to the lower extent of the aquifer, we obtain

$$\frac{\partial}{\partial t} \left[\int_Z^{Z+H} \phi s_\alpha d\zeta \right] + \nabla_{||} \cdot \left[\int_Z^{Z+H} \mathbf{u}_\alpha d\zeta \right] = \int_Z^{Z+H} q_\alpha d\zeta. \tag{B.4}$$

Due to the design of the coordinate system, the flow along the $\mathbf{e}_\zeta$ direction is anticipated to occur significantly faster than the migration in the $(\mathbf{e}_\xi, \mathbf{e}_\eta)$ direction. Consequently, we assume hydrostatic equilibrium in the $\mathbf{e}_\zeta$ direction. In the absence of capillary pressure considerations, CO_2 and brine will be separated by a distinct interface positioned at a distance $h(\xi, \eta)$ from the caprock along the $\mathbf{e}_\zeta$ direction when in equilibrium. Establishing the pressure datum

P_Z at the top surface, the pressure at a specific depth ζ is ascertained by:

$$p(\zeta) = \begin{cases} P_Z + \rho_c \mathbf{g}_\zeta (\zeta - Z) & , \text{ if } Z < \zeta \leq Z + h, \\ P_Z + \rho_c \mathbf{g}_\zeta h + \rho_w \mathbf{g}_\zeta (\zeta - Z - h) & , \text{ if } Z + h < \zeta \leq Z + H, \end{cases} \tag{B.5}$$

Figure 44 also shows how each vertical column is divided into three regions:

1. The CO_2 plume between Z and $Z + h$ with residual brine saturation s_{Rw}, CO_2 saturation $1 - s_{Rw}$, and CO_2 mobility $\lambda_{c,e} = \lambda_c (1 - s_{Rw})$;

2. The residual region between h and h_{max} with CO_2 saturation s_{Rc}, brine saturation $1 - s_{Rc}$, and brine mobility $\lambda_{w,e} = \lambda_w (1 - s_{Rc})$;

3. The region below h_{max} filled by brine.

We hence define vertically-averaged quantities:

$$\mathbf{K} = \frac{1}{H} \int_Z^{Z+H} \kappa_\| d\zeta, \tag{B.6a}$$

$$\Lambda_c(h) = \frac{1}{H} \left[\int_Z^{Z+h} \lambda_{c,e} \kappa_\| d\zeta \right] \mathbf{K}^{-1} \tag{B.6b}$$

$$\Lambda_w(h, h_{max}) = \frac{1}{H} \left[\int_Z^{Z+h_{max}} \lambda_{w,e} \kappa_\| d\zeta + \int_{Z+h_{max}}^{Z+H} \lambda_w(1) \kappa_\| d\zeta \right] \mathbf{K}^{-1} \tag{B.6c}$$

In Equation B.6c we have $s_{Rc} = 0$. Combining these expressions with Darcy's law (Equation B.1b) and setting $\Delta \rho = \rho_w - \rho_c$, we obtain vertically-integrated fluxes:

$$\mathbf{V}_c = -H\Lambda_c \mathbf{K} \left[\nabla_\| (P_Z - \rho_c \mathbf{g}_\zeta Z) - \rho_c \mathbf{g}_\| \right] \tag{B.7a}$$

$$\mathbf{V}_w = -H\Lambda_w \mathbf{K} \left[\nabla_\| (P_Z - \rho_c \mathbf{g}_\zeta Z) - \mathbf{g}_\zeta \Delta\rho \nabla_\| h - \rho_w \mathbf{g}_\| \right]. \tag{B.7b}$$

To develop the usual fractional-flow formulation, we introduce total velocity $\mathbf{V} = \mathbf{V}_c + \mathbf{V}_w$, assume that $\mathbf{K}$ and Λ_α commute ($\mathbf{K}$ isotropic or $\kappa_\|$ constant in ζ), and sum (Equation B.4) over phases. After some manipulations, we obtain a pressure equation:

$$\nabla_\| \cdot \mathbf{V} = Q,$$
$$\mathbf{V} = -H\Lambda \mathbf{K} \left[\nabla_\| P_Z - (\rho_c \mathbf{F}_c + \rho_w \mathbf{F}_w)(\mathbf{g}_\| + \mathbf{g}_\zeta \nabla_\| Z) - \mathbf{F}_w \mathbf{g}_\zeta \Delta\rho \nabla_\| h \right], \tag{B.8}$$

where $\Lambda(h, h_{max}) = \Lambda_w(h, h_{max}) + \Lambda_c(h)$ and $\mathbf{F}_\alpha(h, h_{max}) = \Lambda_\alpha \Lambda^{-1}$, and a transport equation:

$$\frac{\partial}{\partial t} \Phi + \nabla_\| \left[\mathbf{F}_c \mathbf{V} + \Delta\rho \mathbf{K} \Lambda_w \mathbf{F}_c [\mathbf{g}_\| + \mathbf{g}_\zeta \nabla_\| (Z+h)] \right] = Q_c, \tag{B.9}$$

where $\Phi(h, \xi, \eta) = \int_Z^{Z+h} \phi(1 - s_{Rw}) d\zeta$ and $Q_c = \int_Z^{Z+h} q_c d\zeta$. This is the so-called h-formulation of the VE model.

APPENDIX C - COMPUTATIONAL RESOURCES

All simulations were conducted using MATLAB R2023a on a 2.30 GHz Intel Core i7 machine with 16G RAM. The pie chart below (Figure 45) shows the percentage of memory used by the relative functions for each section of the simulations.
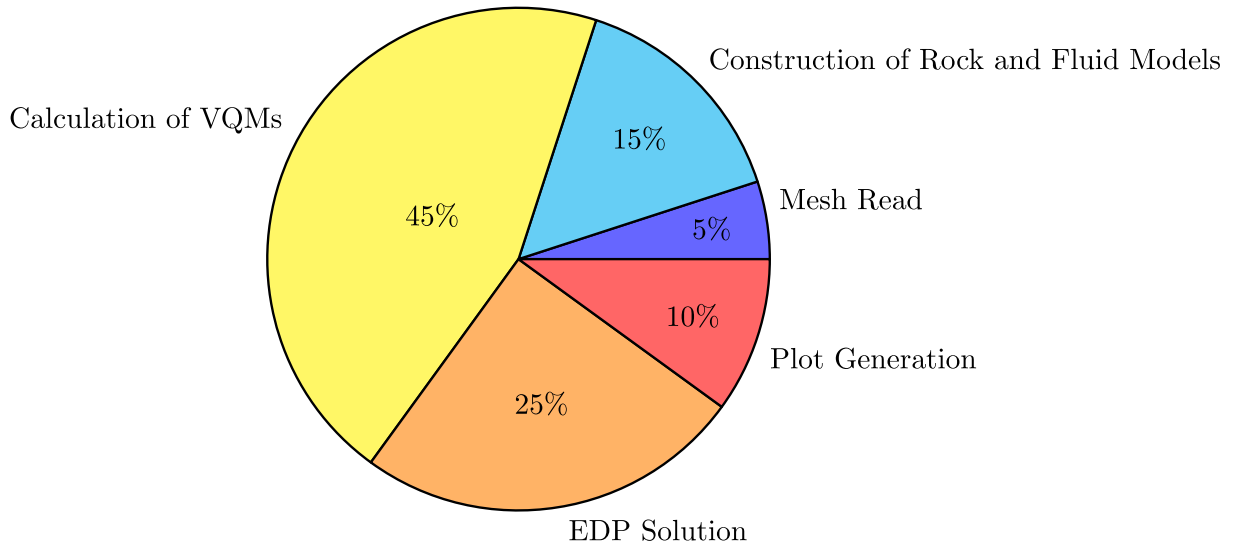

Figure 45 – Pie Chart of the percentage of memory used by the relative functions for each section of the simulations.

APPENDIX D - SCIENTIFIC CONTRIBUTIONS

Find below the scientific production associated to this thesis.

Journal Papers

- **SILVA, J. W. L.**, SANTOS, M. D., OLIVEIRA, G. P. Generalized functionals for qualification of geological carbon storage injection sites. **International Journal of Greenhouse Gas Control**, 2024. DOI:10.1016/j.ijggc.2024.104167.

- FERNANDES, C. P. B., COUTINHO, W. P., **SILVA, J. W. L**, SANTOS, M. D., OLIVEIRA, G. P. Optimal path planning for directional wells across flow units' many-targets. **Journal of Petroleum Exploration and Production Technology**, p. 1-13, 2023. DOI: 10.1007/s13202-023-01709-z.

Event proceedings

- **SILVA, J. W. L.**, OLIVEIRA, G. C. P. Generalized Qualifying Functionals for Geologic Carbon Storage Injection Sites. In: **Mecânica Computacional em Petróleo e Energia (MeComPE 2024)**, Recife, Brazil, 2024.

- TIGRE, Y. S.; **SILVA, J. W. L.**, OLIVEIRA, G. C. P. Classification of Injection Units by Unsupervised Binning Methods for Geological Carbon Storage. In: **Mecânica Computacional em Petróleo e Energia (MeComPE 2024)**, Recife, Brazil, 2024.

- **SILVA, J. W. L.**, SANTOS, M. D., OLIVEIRA, G. Distance-to-trap weighting functions for selection and ranking of CO_2 storage sites. **27th International Congress of Mechanical Engineering (COBEM)**, Brazilian Association of Mechanical Engineering and Sciences (ABCM), Florianópolis, Brazil, 2023.

- **SILVA, J. W. L.**, OLIVEIRA, G. P. Generalized functionals for qualification of geologic carbon storage sites. **2th MRST Symposium**, SINTEF Digital, Oslo, Norway, 2023.

- FERNANDES, C. P. B., COUTINHO, W. P., **SILVA, J. W. L.**, SANTOS, M. D., OLIVEIRA, G. P. Optimal planning of directional drilling operations: a mixed-integer programming formulation. **27th International Congress of Mechanical Engineering (COBEM)**, Florianópolis, Brazil, 2023.

- **SILVA, J. W. L.**, TIGRE, Y. S.; SANTOS, M. D., MIRZAEI-PAIAMAN, A., OLIVEIRA, G. C. P. Analysis of injectivity functionals based on static and dynamic parameters for

co2 storage projects. **XXV Encontro Nacional de Modelagem Computacional (XXV ENMC)**, 2022.